Department of Advanced Materials Engineering
Jagiellonian University

Self–organized polymer structures and their impact on efficiency of organic photovoltaic devices

Monika Biernat

Thesis for Ph.D. degree in Physics
under the supervision of
dr hab. Jakub Rysz

Kraków, 2018

Wydział Fizyki, Astronomii i Informatyki Stosowanej
Uniwersytet Jagielloński

Oświadczenie

Ja niżej podpisana Monika Biernat (nr indeksu:1081059) doktorantka Wydziału Fizyki, Astronomii i Informatyki Stosowanej Uniwersytetu Jagiellońskiego oświadczam, że przedłożona przeze mnie rozprawa doktorska pt. *"Self–organized polymer structures and their impact on efficiency of organic photovoltaic devices"* jest oryginalna i przedstawia wyniki badań wykonanych przeze mnie osobiście, pod kierunkiem dr hab. Jakuba Rysza. Pracę napisałam samodzielnie.

Oświadczam, że moja rozprawa doktorska została opracowana zgodnie z Ustawą o prawie autorskim i prawach pokrewnych z dnia 4 lutego 1994 r. (Dziennik Ustaw 1994 nr 24 poz. 83 wraz z późniejszymi zmianami).

Jestem świadoma, że niezgodność niniejszego oświadczenia z prawdą ujawniona w dowolnym czasie, niezależnie od skutków prawnych wynikających z ww. ustawy, może spowodować unieważnienie stopnia nabytego na podstawie tej rozprawy.

Kraków, dnia . . . .

podpis doktoranta

Streszczenie

Tematem przewodnim rozprawy są organiczne ogniwa słoneczne, lekkie, elastyczne oraz tanie w produkcji urządzenia bazujące na półprzewodnikach organicznych. W rozprawie poruszono dwa tematy: 1) właściwości fizyczne mieszaniny polimer–fuleren używanej do produkcji warstwy aktywnej ogniwa słonecznego, 2) wpływ polimerowych warstw pułapkujących światło na absorpcję światła oraz wydajność organicznych ogniw słonecznych.

Pierwsza część poświęcona została przewodzącemu kopolimerowi na bazie karbazolu (PCDTBT), stosowanego jako materiał donorowy w organicznych ogniwach słonecznych. W pierwszej kolejności, na podstawie puchnięcia warstwy polimerowej w obecności par rozpuszczalnika, wyznaczono parametr oddziaływania Florego–Hugginsa χ pomiędzy PCDTBT oraz czterema rozpuszczalnikami. Parametr ten pozwala określić kompatybilność pomiędzy danym polimerem a rozpuszczalnikiem. Z punktu widzenia organicznych ogniw słonecznych parametr ten odgrywa ważną rolę przy formowaniu objętościowego heterozłącza bazującego na mieszaninie materiału donorowego i akceptorowego.

Zgodnie z naszą wiedzą w niniejszej rozprawie po raz pierwszy przedstawiono wartości χ dla pary PCDTBT oraz następujących rozpuszczalników: chloroform, chlorobenzen, toluen oraz o-dichlorobenzen. Następnie na podstawie otrzymanych parametrów χ skonstruowano trójskładnikowy diagram fazowy dla mieszaniny – PCDTBT, $PC_{70}BM$, rozpuszczalnik – w oparciu o który starano się wytłumaczyć końcową morfologię heterozłącza PCDTBT:$PC_{70}BM$ otrzymanego w wyniku separacji fazowej. Przewidywania te zostały porównane z rzeczywistą morfologią warstwy zbadaną przy użyciu mikroskopii sił atomowych.

Głównym celem drugiej części rozprawy było zbadanie wpływu polimerowych warstw pułapkujących światło — periodycznych siatek oraz losowo rozłożonych porów — na absorpcję światła oraz wydajność organicznych ogniw słonecznych. Struktury te otrzymano przy użyciu miękkiej litografii oraz wykorzystując wzory kondensacyjne. O ile siatki periodyczne otrzymane przy wykorzystaniu komercyjnych płyt DVD oraz CD nie wykazały poprawy wydajności ogniw, o tyle struktury porowate doprowadziły do wzrostu absorpcji oraz prądu zwarcia.

W ramach pracy poszerzono wiedzę na temat tworzenia się wzorów kondensacyjnych oraz zbadano jak ich rozmiary (ich głębokości i średnice) wpływają na absorpcję światła. Największą poprawę otrzymano dla struktur o wąskiej dystrybucji kształtów skupionej wokół średnicy 0.15 μm oraz głębokości 0.35 μm. Wyniki te są zgodne z wynikami symulacji przygotowanej przez dr Jakuba Haberko. Następnie pokazano, że struktury porowate o średnicy poniżej 1.1 μm oraz głębokości poniżej 350 nm umieszczone na zewnętrznej stronie ogniwa słonecznego zwiększają prąd zwarcia w ogniwach o 6%.

Na zakończenie zaproponowano wykorzystanie metody poziomego rozciągania roztworu (horizontal–dipping) do tworzenia struktur porowatych. Technika ta daje możliwość przygotowania warstw, w których średnie rozmiary struktur są gradientowo rozłożone wzdłuż próbki, co pozwala na badanie wielu typów struktur jednocześnie przyspieszając badania. Struktury te zostały następnie powielone za pomocą miękkiej litografii i umieszczone na zewnętrznej stronie ogniw słonecznych. Również w tym wypadku zaobserwowano poprawę prądu zwarcia.

Contents

Chapter 1

Introduction

Synthetic polymers, commonly called plastics, have become an indispensable part of our modern society. Plastics found in every–day applications are commonly associated with insulators. This is, however not true in general: in 1977 Shirakawa, MacDiarmid and Heeger discovered that a doped polyacetylene conducts electricity. This discovery and their further work on conductive polymers brought them the Nobel Prize in Chemistry 23 years later. Due to the unique properties of conductive polymers such as variety of chemical structures, ease of processing, macroscopic flexibility and low–cost fabrication they have already found a wide range of applications especially in organic electronics. Examples of such applications include organic LEDs (OLEDs), organic photovoltaics (OPVs) and organic field effect transistors (OFETs). Whereas OLEDs have already entered the market, OPVs adoption is hindered by their low efficiency and rapid degradation compared to traditional silicon photovoltaics [1]. To overcome these problems research is being directed towards extending the theoretical description of OPVs, exploring new materials and incremental optimizations of OPV devices.

One way to produce optimal structures in an efficient way is to apply self-organizing materials. Such materials can be used to generate a large array of shapes and structures. In particular, due to phase separation they can create bicontinuous interpenetrating structures, commonly used to form bulk heterojunctions (BHJ) in OPVs. Such BHJ structures are usually formed spontanously during the deposition of a polymer:fullerene mixture. However, the phase separation process leading to BHJ is difficult to control and its outcomes cannot be easily predicted. Therefore we still have to refer to experimental methods to gain information on the physical properties of resulting structures.

In the first part of this thesis we investigate the phase separation in a ternary system of carbazole–based copolymer (PCDTBT) and fullerene derivative $PC_{70}BM$ dissolved in common solvents, which is nowadays one of the most prospective mix-

tures for BHJ [2]. We composed ternary phase diagrams for this mixture (the first such result to our knowledge) and compared them with the final morphology of BHJ. To construct the ternary phase diagrams we measured Flory–Huggins interaction parameters between PCDTBT and several solvents. These parameters are also relevant by themselves as they provide insights into the thermodynamic properties of polymer solutions such as their miscibility or solubility.

In the second part of this thesis we shift our attention to another aspect of OPVs: the light–trapping layer. This layer can be attached to the front side of an OPV where its main function is to increase the scattering angle of incoming light. With larger scattering angles the photons traverse longer paths within the OPV and have increased chance of absorption. Our work focused on comparing how different surface geometries influence the optical properties of the light–trapping layer and whether this leads to an increased performance of OPVs. In particular, we compared periodic geometries with random geometries, where the latter were based on breath figures (patterns formed by water condensing on a cold polymer solutions surface). As far as we know, the breath figures have never before been investigated in the context of light– trapping layers for OPVs.

Chapter 2

Theoretical background

2.1 Organic solar cells

The increasing interest in new renewable energy sources is dictated by the shrinking supplies of fossil fuels and the motivation to reduce greenhouse gas emissions. Among different solutions, sunlight seems to be the most promising energy source for the near future. Inorganic solar cells, mainly based on silicon wafers, have already successfully entered an energy market. The efficiency of commercial silicon wafers modules amount to about 17% [3], whereas in the laboratories the best results reach up to 25.6% [4]. Despite the fact that prices of silicon–based solar cells have been visibly reduced over the last decade there are still too high when compared to other electrical sources [5]. Therefore there is a significant research interest to find alternative materials and technologies which will meet the market requirements. This thesis focuses on thin solar cells based on organic semiconductors, mainly conjugated polymers, which are characterized by desirable qualities such as low cost, flexibility, transparency and potential to integrate into infrastructures [6].

In the last two decades the researchers made great effort to develop new organic materials with suitable opto–electronic properties which shift the efficiency of organic solar cells (OPV) from 1% to over 11.2 % in 2016 [4]. Such enhancement was possible not only thanks to new materials but also through understanding of the fundamental processes in OPV and systematic optimizations. Below we describe some breakthrough technological improvements and current and past research that OPVs have undergone, including their operation principle, the device structures and measurement methods.
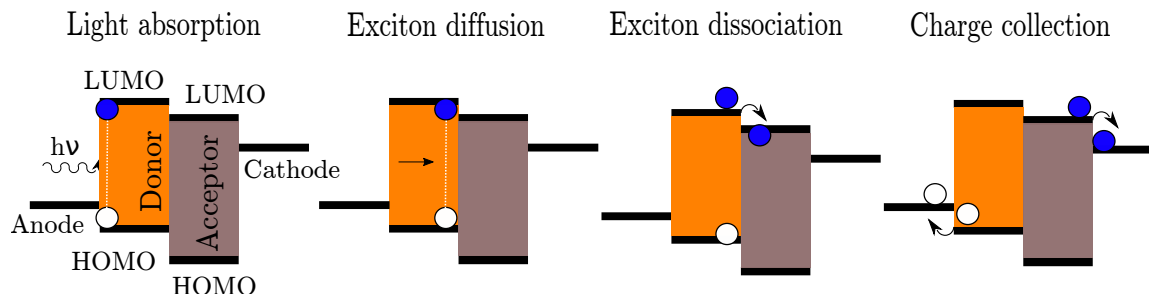
Figure 2.1: Schematic illustration of charge generation process within an organic solar cell.

2.1.1 Operation principle

Organic solar cells (OPV), like their inorganic counterparts, harvest the solar energy and convert it into electricity. However, the photovoltaic process for inorganic and organic cells differ from one another. In inorganic solar cells the photon absorption leads to a formation of free charges, electrons and holes, which after separation at a p–n junction diffuse to respective electrodes. In case of OPV, due to low dielectric constant of organic materials ($\varepsilon \sim 3 - 4$ [7]), the light absorption does not directly lead to free charge formation but to an exciton creation, which is an electron–hole pair bounded with Coulomb force. Excitons, as neutral quasi–particles, do not contribute directly to the photocurrent, instead they have to be firstly separated into free charges. This separation has to occur within their lifetime, otherwise the absorbed energy will be lost through nonradiative or radiative decay [8]. The exciton dissociation typically occurs at the interface between donor and acceptor materials, where the energetic difference between donor and acceptor lowest unoccupied molecular orbital LUMO levels exceed the exciton bond energy ($\sim$0.3–0.5 eV) [9]. As we will discuss later, due to a short exciton characteristic distance 10 nm, the proper donor–acceptor interface architecture is a key factor in OPV development. At the end, after exciton separation, free positive and negative charges can travel within the respective materials to the proper electrode. The whole photovoltaic process for OPV is schematically summarized in Figure 2.1. The overall efficiency of OPV depends on each of the steps including light absorption, exciton generation and diffusion, charge separation and collection.

Light absorption   The efficiency of the light harvesting inside the active layer of OPV depends on several factors: a layers thickness, an absorption coefficient and a bandgap of active layer materials. Organic materials have a relatively high absorption coefficient ($\sim 10^5$ cm^{-1} [10]) therefore an absorption layer of a few hundreds nanometers suffices to absorb all the light at the material absorption peak [11]. However, due to low charge mobility in organic semiconductors ($\sim 10^{-3}$–10^{-6} cmV^{-1}s^{-1} [11]), there is a mismatch between optimal thickness from the optical and electrical perspective. Even hundreds of nanometers cause a significant increase in resistance which nega-

tively influence the overall efficiency. Therefore the optimal active layer should be as thin as possible without loosing the absorption capability. One method to achieve this is to increase the optical path via various light trapping and scattering techniques [12]. The major part of the presented thesis is devoted to external light trapping structures and their influence on the OPV performance (see Section 5).

Another obstacle which limits the efficient absorption is an insufficient overlap between the absorption spectra of organic materials and the solar spectrum. The majority of the solar energy is concentrated at the visible and near IR regions, whereas the bandgap of common semiconducting polymers, such as poly(3–hexylthiophene), does not exceed 2 eV, corresponding to a wavelength less than 620 nm. Thereby at most 30% of the solar energy can be absorbed. There is a huge scientific interest to find new organic materials with lower bandgap which will absorb in a wider solar spectrum. Recently, researches developed new low-band polymers [13] for which the absorption spectra is extended up to 826 nm [11]. On the other hand, narrowing band gap can lead to a mismatch between the donor and acceptor energy levels of materials in OPV which negatively affects the open circuit voltage (the maximum voltage which a device can deliver to an external circuit) and lower the overall OPV efficiency [14]. Therefore, to have the best OPV performance, the balance between optical and electrical parameters must to be struck.

Exciton diffusion and dissociation   After the creation of an exciton it has to reach a donor–acceptor interface within its lifetime to undergo charge separation. Unfortunately, for organic materials the exciton diffusion length is within the range of tens of nanometers [15] which means that only excitons created within this distance from the donor–acceptor interface will participate in the photocurrent. This process can be improved either by extending the exciton diffusion length (e.g. through enhancement of crystalline order of materials, balancing radiative and non–radiative decay by host–guest dilution [16]) or by designing a favorable donor–acceptor interface. Let us concentrate on the second aspect as the major breakthrough in OPV was related to introduction of a new donor–acceptor architecture, so-called bulk heterojunction (BHJ), schematically presented in Figure 2.3B.

The idea behind BHJ is to prepare an interpenetrating donor–acceptor network characterized by a large interfacial area and by adequate donor and acceptor percolated pathways. Such network would help the created exciton reach the interface, be dissociated within its lifetime and then, as a free charge, be transported without recombination to the respective electrode. The first organic solar cells based on BHJ with efficiency exceeding 1% were presented by Yu et al. [17] in 1995. Up to this moment BHJ has been the most studied configuration for OPVs [14]. Such bulk–heterojunction is formed during the phase separation of the donor and acceptor blend cast from a common solvent. The final morphology of the bulk–heterojunction depends on many factors (choice of solvent, solution concentration, processing conditions, post–processing treatments, interaction between components, miscibility, etc.)

making it hard to control and to understand. Nevertheless, there is a significant effort to find the optimal materials and preparation conditions which will result in the optimal bulk–heterojunction morphology [18, 19]. One of the approaches to predict the final morphology is to study a phase behavior of binary or ternary systems [20–22]. One of the objectives of the presented thesis was to analyze the behavior of one such donor–acceptor mixture (carbazole–bazed copolymer blended with fullerene) via ternary phase diagram. The results are presented in Section 4.

Once excitons reach the donor–acceptor interface they can be dissociated into free charges or recombined to a ground state. The dissociation can happen if the energy difference between donor and acceptor LUMO level exceeds the exciton binding energy and proceeds in several steps, including a formation of a weakly bounded intermediate charge transfer state. This state, however, can still lead back to a recombination, the undesirable process in the context of photocurrent creation. The probability of a recombination depends, among others, on the interface morphology [18].

Charge transport and collection After exciton dissociation one of the final steps to capturing the exciton energy is to efficiently transport charges through the device to the respective electrodes. The transport is driven by both drift (caused by internal and external built–in field) and diffusion (related to charges concentration gradient). Due to amorphous (non–crystalline) nature of organic materials the charge transport has a hopping character rather then a coherent band-like motion, as in highly ordered molecular crystal or inorganic semiconductors. The charge mobility of a disordered polymer is rather low, in the range of $10^{-6} - 10^{-3} cm^2/Vs$ [23]. However, there are several ways to improve the mobility, making the transport more efficient: better molecular packing, optimizing the molecular size and weight and also reducing the morphological defects which negatively affect the charge lifetime [23].

The final step is to efficiently collect charges at the respective electrodes. To minimize the losses the acceptor and donor layers should form an Ohmic contact with respective electrodes. In practice, intermediate layers are used to better fit the energetic levels of the materials and also block undesirable charges.

2.1.2 Device structures

Figure 2.2 schematically presents the conventional architecture of OPV with selected layers. An active layer, a major part of the device where the energy from light is transferred to the charges, is located between two electrodes of which at least one has to be transparent (depending on the architecture of the OPV). Intermediate layers, placed between the active layer and the electrodes, can improve the charge extraction and therefore increase the efficiency of the photovoltaic process. The organic devices are susceptible to degradation under different environment factors like oxygen, humidity, temperature [24]. To suppress such degradation additional protection barriers are necessary.

Glass
Transparent electrode
Intermediate layer
Active layer
Electrode
Protection barrier

Figure 2.2: Schematic picture of organic solar cells with layers placed in certain order - two electrodes, which at least one has to be transparent; active layer, where light is absorbed and convert into charges, intermediate layer which improves charge extraction and protection layer which reduces the negative impact of the environment on the device performance.

Electrodes and substrate   One of the most common transparent electrodes, used not only for OPV but also in liquid crystal displays, touch panels or organic light–emitting diodes, is indium tin oxide (ITO) characterized by high optical transmission in the visible region and high electrical conductivity [25]. However, due to high costs (ITO is the most expensive part of OPV [26]), poor mechanical flexibility and limited supply (ITO is listed among 14 the most critical raw materials in the world [27]) there is a huge research effort to find low–cost replacements for ITO. The most promising alternatives include carbon based electrodes like graphene, carbon nanotubes or conducting polymers [28].

As for the substrate, glass is still one of the most popular material due to its low cost and stability. It fits well as a rigid substrate, however, it is not suitable for roll–to–roll manufacturing. Therefore alternative materials are under examination like flexible plastic substrates; poly(ethylene terephthalate) PET, polycarbonate PC [29] or recyclable cellulose substrate [30]. In general substrates should satisfied several requirements like high transparency, high surface smoothness to avoid shunts in the devices, have high dimension stability, good resistance to chemical, temperature or mechanical impact [25].

Interfacial layer   One of the last steps in photocurrent generation is to efficiently collect the charges at the electrodes. To facilitate this process the interfacial layers are commonly placed between the active layer and electrodes. They improve the selective hole or electron extraction by simultaneously blocking the opposite charge, minimizing the recombination losses and adjusting the energy levels. In the organic devices, where ITO is used as a transparent anode, there is often a mismatch between ITO work function and HOMO level of donor materials. To improve the Ohmic contact one of the most common choices for a cathode interlayer is poly(3,4-ethylenedioxythiophene) polystyrene sulfonate (PEDOT:PSS) characterized by high transparency and solution processability. However, as studies showed, it negatively influences the device stability [15], therefore there is a great effort to find the alternatives. Here inorganic materials
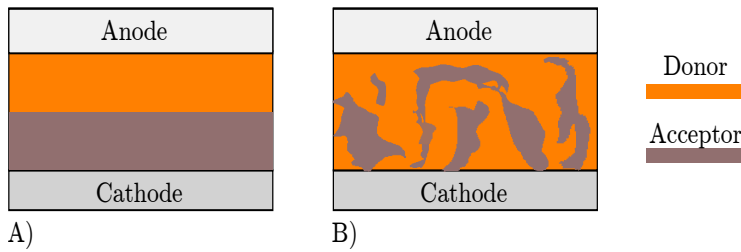
Figure 2.3: Schematic illustration of three different strategies for donor–acceptor architectures: A) a bilayer structure, B) a bulk heterojunction

(p-type metal oxides as NiO, V_2O_5, MoO_3), polymers (doped polyanilines, conjugated polyelectrolyte) or self–assambled monolayers are under examination [14]. For efficient electron collection and hole blocking the most widely used cathode interfacial layers are ZnO (due to its high conductivity, solution processibility and low cost), TiO_x, graphenes and self–assembled monolayers [15].

Active layer   The active layer, a place where absorbed photons are converted into the excitons and then separated into free charges, typically consists of two materials: donor and acceptor. There are several strategies how these two materials can be arranged within the active layer (Figure 2.3).

Historically, the first organic solar cells with efficiency close to 1% presented in 1986 by Tang et al. [31], were based on a bilayer structure (Figure 2.3A). Unfortunately, for many years the researchers failed to get a highly efficient bilayer OPV, the best ones did not exceed 3% [11]. The main reason behind it was that in the bilayer structure only a small volume of the active layer is fully involved in charge production. As we already discussed, due to short diffusion exciton length within conductive materials only excitons created closed to donor–acceptor interface can be dissociated and then collected at the electrodes.

Recently, however, Seo et al. [32] made a breakthrough presenting their sequentially deposited polymer–fullerene bilayer OPV with efficiency 7.12%. They showed that by adding the ordering agent to the polymer solution and heterojunction agent to the fullerene solution it is possible to obtained nanoscale non–planar heterojunctions which enlarge the interfacial area between the donor and acceptor. Based on these positive results one can expect that in near future the bilayer system will attract much more attention.

The second and also the most studied donor–acceptor architecture is the so–called bulk heterojunction (BHJ) (Figure 2.3B) which we have already introduced in Section 2.1.1. Here the donor and acceptor materials form bicontinuous interpenetrating networks with extensive interfacial surface which enables efficient exciton dissociation. Since 1995 the OPVs based on BHJ have been widely studied and the top results can be found in several reviews [14, 33, 34]. In a nutshell, the research on BHJ in OPV carried out for more than 20 years has been concentrated on exploiting a

new donor– acceptor materials [14], controlling and optimizing the morphology in bulk–heterojunction [19] and finding the optimal processing conditions. Additionally, a lot of attention was recently given to test and improve device reliability, stability and lifetime [35–37].

For years the most investigated donor–acceptor materials were mixtures of poly(3–hexylthiophene) P3HT with fullerene derivative $PC_{60}BM$. Despite the fact that the efficiency of the devices was not high (based on metastudy [34] most of the reported efficiency were between 3% and 4%), the studies under this system brought a lot of important strategies on how to enhance the device performance by thermal or solvent annealing, selection of solvent, using the processing additives and increasing the crystallinity which were later successfully applied for other BHJ systems.

Subsequently, the focus was shifted to low band gap polymers like polyfluorene or polycarbazoles as novel donor materials for BHJ. A polymer with a band gap below 2 eV can absorb light with wavelengths greater than 620 nm resulting in more efficient harvesting of solar energy compared to poly(3–hexylthiophene). Additional increase in open–circuit voltage V_{oc} and short–circuit current density J_{sc} was obtained by decreasing and optimizing the energy bandgap and the donor HOMO energy level. All of these changes result in high performance devices with efficiency regularly exceeding 7% [38].

2.1.3 Photovoltaic characteristics

Current–voltage characteristic and equivalent circuit   The performance of an organic solar cell can be determined by measuring the device current response on the applied voltage (Figure 2.4 A). Under dark conditions the current–voltage (J–V) characteristic follows a diode behavior, whereas under the illumination solar cell can be treated as a current generator which delivers the photocurrent. For the ideal solar cell under the illumination the J–V curve can be expressed by:

$$J = J_s \left[\exp\left(\frac{qV}{k_B T}\right) - 1\right] - J_{ph},\tag{2.1}$$

where J_s is a saturation current density, q the elementary charge, V the applied voltage, k_B the Boltzmann constant, T the temperature and J_{ph} the photocurrent density.

In reality, however, due to the presence of different parasite resistances (series R_s and shunt R_{sh}) the J–V curve deviates from the ideal shape described by Eq. 2.1. R_s is mainly associated with the resistance of the active layer and electrodes as well as the resistance between interfaces, whereas R_{sh} is related to leaking current induced by impurities or manufacturing defects. Figure 2.5 presents the equivalent circuit for a non–ideal organic solar cell with a photocurrent source, a diode and a shunt and series resistor. For such system the current response can be written as:

$$J = J_s \left[\exp\left(\frac{q}{nkT}(V - JR_s)\right) - 1\right] + \frac{V - JR_s}{R_{sh}} - J_{ph}\tag{2.2}$$
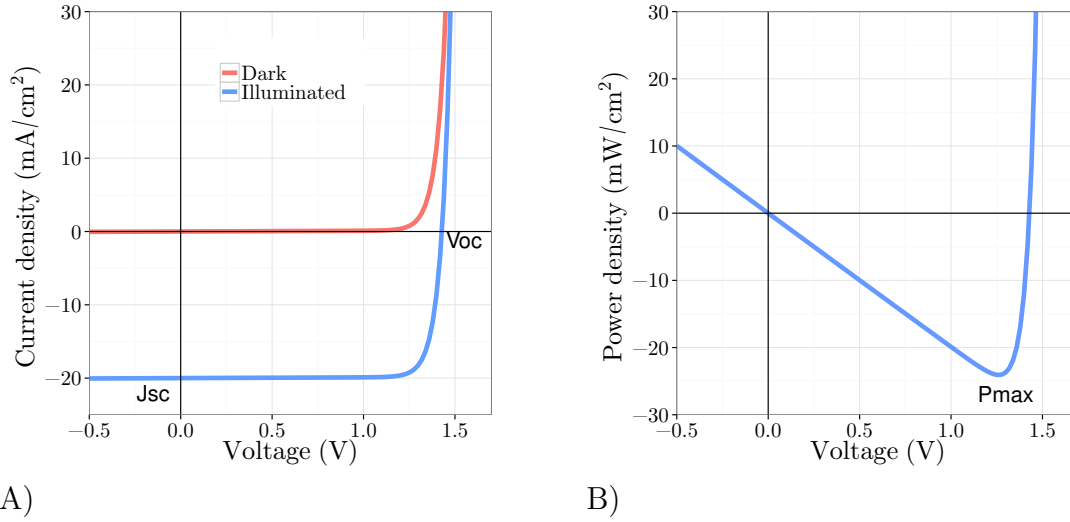
Figure 2.4: A) Current-Voltage characteristic for idealized solar cell without any parasitic resistances in dark and under illumination. The J-V curve intersection with y-axis determines the short-circuit current density J_{sc} whereas the intersection with x-axis the open-circuit voltage V_{oc}. B) Electrical power curve with a marked maximum power point also known as the optimum operation point.
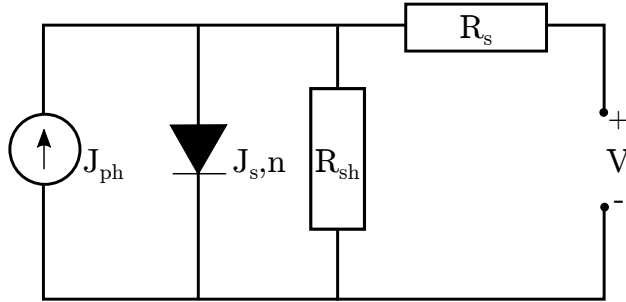
Figure 2.5: Equivalent circuit of a non–ideal solar cell consisting of photocurrent generator J_{ph}, diode part with marked current density of diode J_s and ideality diode factor n, series R_s and shunt resistance R_{sh}.

where n is the ideality factor of the diode. The factor n indicates how close the diode matches the ideal diode theory. If $n = 1$ then there is no carrier recombination in the depletion region and diffusion current dominates, for $n = 2$ the situation is reversed. Due to the presence of both diffusion and recombination currents n should be within the range 1 to 2. However, in case of organic solar cells as well as thin film solar cell n is often found to be greater than 2 due to the presence of different traps and heterojunctions [25].

Efficiency The J–V characteristic gives us a valuable source of information about the quality of the device and the different processes occurring in it. On top of that the J–V curve allows to calculate the overall efficiency of the device (a power conversion ratio) defined as a ratio of maximum power density P_{max} generated by the device to the density power of the incident light P_{in} according to the formula below.

$$PCE = \frac{P_{max}}{P_{in}} = \frac{J_m V_m}{P_{in}} = \frac{J_{sc} V_{oc} FF}{P_{in}},\qquad(2.3)$$

where P_{max} is a product of J_m and V_m in the optimum operation point (Figure 2.4B); J_{sc} is short–circuit current density which describes the current flow under zero voltage; V_{oc} open–circuit voltage the maximum voltage which can be delivered to an external circuit and FF is a fill factor which describes how close to a rectangle the J–V curve is. Let us look on some factors which influence the above parameters.

Fill Factor This parameter characterizes how rectangular the J–V curve is and is defined as a ratio between the maximum output power of a solar cell and a rectangle spanned by the V_{oc} and I_{sc} and (0,0):

$$FF = \frac{I_m V_m}{I_{SC} V_{OC}}\qquad(2.4)$$

In case of organic solar cells FF is usually within the range of 50 to 70% whereas for inorganic devices it can reach up to 90% [39]. FF is related to the balance between charge extraction and recombination therefore it is mainly affected by the carriers mobility, charge collection and series and shunt resistances [40]. In recent years different approaches were proposed to enhance FF in organic solar cells among others using a buffer layer which will reduce contact resistance or current leakage, improving mobility through morphology optimization and crystallinity enhancement [39].

Open Circuit voltage Open–circuit voltage, V_{oc}, is the maximum voltage which can be delivered to an external circuit. For organic solar cell, the V_{oc} is predominantly determined by the difference between highest occupied molecular orbital (HOMO) of donor and lowest unoccupied molecular orbital level (LUMO) of acceptor [41]. Scharber et al. [42], based on examination of 26 different donor–acceptor materials, proposed an empirical expression for V_{oc} in organic solar cells.

$$V_{oc} = \frac{1}{e}(D_{HOMO} - A_{LUMO}) - 0.3.\qquad(2.5)$$

Unfortunately, there is still lack of precise understanding of origin of V_{oc} [43]. Nevertheless, up to now, the researchers found plenty of factors influencing the open circuit voltage in organic solar cells like donor–acceptor interface area, charge transfer state, morphology, temperature, defects, crystallinity, charge mobility and recombination rate (see [41] for a comprehensive review).

Short Circuit Current   Even under zero voltage the illuminated solar cells produce the photocurrent known as short–circuit current I_{sc}. The value of I_{sc} depends on the devices area therefore to remove this dependence this parameter is commonly substituted by short–circuit current density J_{sc}. Under ideal conditions, without any loss mechanisms, the J_{sc} will be the same as the light–generated current and will be equal to the product of photoinduceed charge carrier density and the charge mobility within the organic materials.

The values of J_{sc} is mainly associated with the optical and transport properties of active layers materials. To ensure a high J_{sc} value the absorption spectrum of materials should overlap with the sunlight spectrum. For materials with a bandgap of 1.8 eV (like poly(3–hexylthiophene)), where each absorbed photon generates an electron, J_{sc} will reach 20 $mA \cdot cm^{-2}$ [11]. Therefore, as we already pointed out, a lot of attention is currently being devoted to finding polymer materials with a lower bandgap.

2.2   Light management for organic solar cells

Efficient light absorption in photovoltaic devices is one of the crucial factors which determines their overall performance. Compared with silicon, conductive polymers have relatively high absorption coefficient 10^5 cm^{-1}, so hundreds of nanometers of materials is enough to absorb most of the radiation [25]. However, the optimal organic active layer, where the absorption and charge generation occurs, is much thinner than it should be from an absorption perspective due to a limited exciton diffusion range of $\sim$10 nm. Therefore a lot of attention has been devoted to find new approaches which will improve absorption and keep the active layer thin to enable efficient charge collection. As in the case of silicon solar cells, the optical enhancement can be realized through anti–reflection or light trapping structures. The anti–reflection structures are attached on the front side of a solar cell whereas the light trapping structures can be integrated both outside and inside of the device [44]. Below we will describe both strategies with particular emphasis on using polymer materials. Thanks to their self–organization or phase separation a wide range of structures with different dimensions can be formed. A considerable part of the presented thesis was devoted to polymer light trapping structures and their influence on the organic solar cells performance (Section 5).

2.2.1   Anti–reflection structure

When modeling light travelling through a medium we have to take into account several physical phenomena depending on optical properties and surface texturing of the material: the light can be transmitted, absorbed, scattered, refracted or reflected.

The light reflection at uniform planar interfaces can be described via Fresnel equations. In the simplest case when the light is reflected only from one interface, e.g.

reflection between air and substrate, the incidence angle is equal zero and there is no difference between p and s polarization the reflectance is given by [45]:

$$R = \left| \frac{n_0 - n_s}{n_0 + n_s} \right|^2, \tag{2.6}$$

where n_0 and n_s are refractive index of air and substrate. For a common glass with $n_s \approx 1.5$ the reflectance is 4%, in case of silicon layer the reflectance reach up to 30% due to larger refractive index $n_s \approx 3.5$ compared to air.

There are several ways to decrease the reflectance: single or multilayer coating, gradient refractive index coating, introducing additional porous layers or applying surface–relief grating [46–48]. The structures can be fabricated either bottom up by solution processing, physical or chemical vapour deposition or top down using etching [46].

Anti–reflection strategies   The simplest antireflection coating can be manufactured from a single homogeneous film placed on top of the substrate. Under special conditions the reflected light from interface e.g. substrate and air can interfere destructively maximazing the light transmission. For an exact reflectance cancellation two criteria have to be met. Firstly, the thickness of anti–reflection layer has to be an odd multiple of a quarter of the wavelength of the incident beam. Secondly, two reflected wave must have the same intensity which is satisfied when the refractive index of an anti–reflection coating is a geometric mean $n = \sqrt{n_0 n_s}$ of the refractive index of air (n_0) and substrate (n_s) [46]. For glass substrate with refraction index ≈ 1.5 the antireflection material should have index about 1.22. Unfortunately, materials which meet this criterion are rare [46]. Additionally, the single–layer coating has a major limitation. Due to the dependence of refractive index on wavelength this strategy can be optimized only for a single wavelength and for a fixed (normal) angle of incidence.

An antireflection effect in broad spectrum range can be achieved through a multi–layer coating or a gradient refractive index coating, where refractive index gradually decreases from the top to the bottom of the antireflection layer. It was demonstrated that a gradient–index medium can be realized through polymer porous layers prepared using phase separation of polymer blends [49, 50], block–copolymer [51–53] or breath figures [54, 55]. The influence of breath figures on the light propagation will be discussed in more detail in Section 2.2.3 as one of the objective of the presented thesis is to examine the effect of breath figures on changes in organic solar cells performance (Section 5.2).

Walheim et al. [49] showed that nanoporous polymer films can improve transmission up to 99.7% over the whole visible spectrum. The nanoporous structures were prepared via phase separation of polymethyl–methacylate and polystyrene resulting in lateral phase morphology. To produce porous films one of the components, in this case polystyrene, had to be selectively dissolved. By changing the volume fraction of polymer composition they were able to vary the refractive index between 1.5 to 1.05.
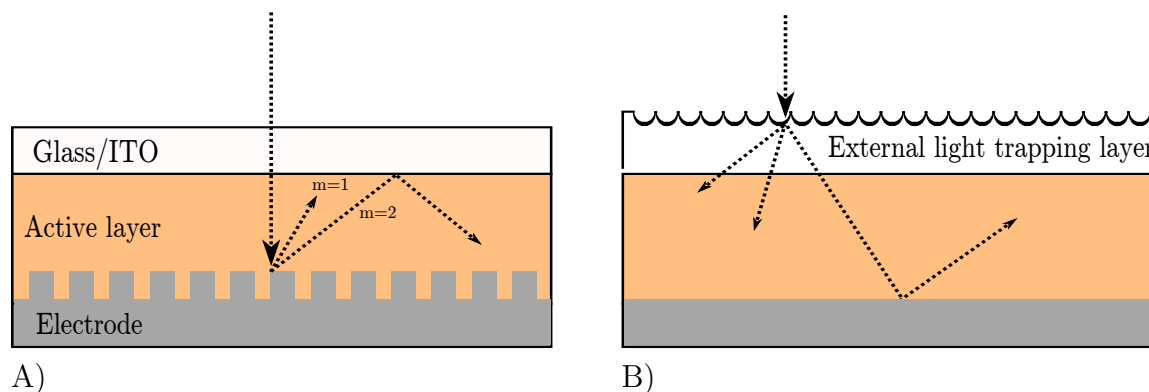
Figure 2.6: Two strategies how to increase the optical path inside the active layer of organic solar cells: A) by modifying active layer – electrode interface with periodic structures, B) by attaching an external light trapping layer.

Park and Kim [54] found that breath figures prepared from cellulose acetate butyrate with average pore diameter of 227 nm reduce reflectance of glass from 4% to less then 1% in the wavelength region between 900 and 2000 nm. Galeotti et al. [55] went a step further: they used breath figures as templates for PDMS replica molding. They showed that a glass surface covered with hemispherical nanodomes with diameter of 250 nm and depth of 100 nm in has 2% higher transmission compare to flat glass substrate. In Section 5.2.1 we will show how the breath figures imprinted on an glass substrate with this technique affect the light transmissions.

In the context of organic solar cells the question is how the reduction of light reflectance due to additional antireflection structures translates into changes in performance of devices. As Luk et al. [56] showed the self–assembling nano–silica spheres with 126 nm in diameter not only reduce the light reflectance by 3% but also improve the efficiency of organic solar cells (based on P3HT:PC$_{60}$BM) from 1.8% to 2.05%. Chen et al. [57] used moth eye monostructures with groove depth of 180 nm and period of 200 nm as a self-cleaning antireflection layer. They reported a decrease in average reflectance from 12% to 5% over the wide spectrum from 300 nm to 800 nm along with an increase of organic cell efficiency up to 3.89%. As the above studies showed, adding anti–reflection layers is a viable strategy to increase OPVs performance [57].

2.2.2 Light trapping structures

The goal of light trapping is to extend the light path inside solar cells and thereupon increase the probability of light absorption. This can be achieved by employing random or ordered surface structures, backside reflector, electrode engineering, plasmonic structures or photonic crystal [12, 44, 58–63]. Below we will concentrate mainly on a periodically modified active layer (Figure 2.6A) and external light trapping layers (Figure 2.6B) as the main part of the presented thesis was dedicated on these topics.
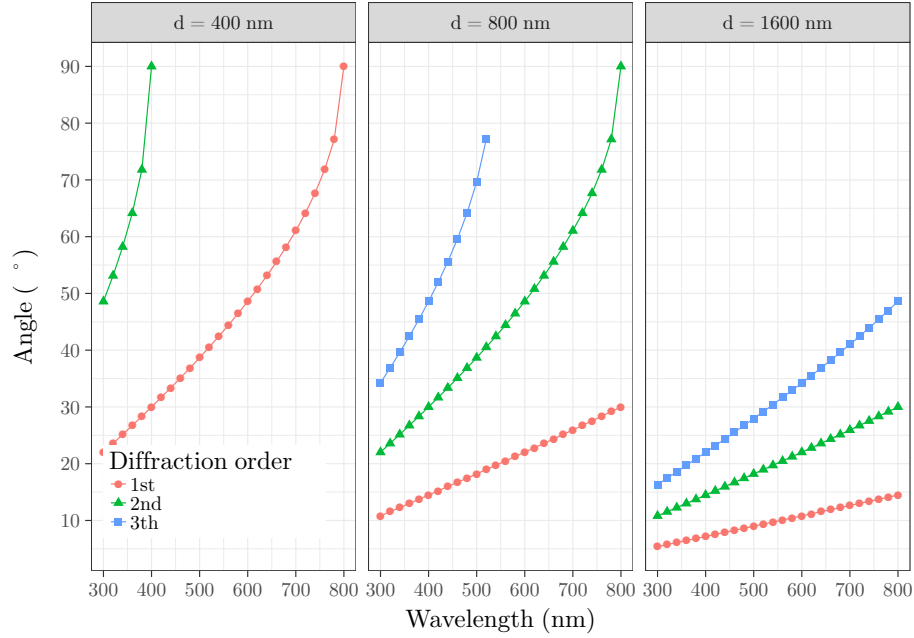
Figure 2.7: The influence of three grading periods (400 nm, 800 nm and 1600 nm) on the diffraction angles.

Additionally, we will refer to simulations performed by dr Jakub Haberko in which the author examined the influence of dimensions of external porous structures on the light propagation.

Grating structures

One of the method how to trap light inside the solar cell is to use different 1D or 2D grating structures integrated either directly on the active layer [64] or on one of the electrode [65, 66]. As is schematically depicted in Figure 2.6A, due to backward diffraction on the periodic structures the direction of light propagation is changed increasing the optical path inside the solar cells. The diffraction angles can be calculated based on Bragg grating equations:

$$m\lambda = nd(\sin\theta_i + \sin\theta_m) \tag{2.7}$$

where m is the diffraction order, λ the wavelength of incident light, n refractive index of active layer, d grating period, θ_i the incident angle and θ_m the diffraction angle of m diffraction order.

Let us check how the choice of grating periods affects diffraction angels. Here we concentrate on three values $d = 400\ nm, 800\ nm, 1600\ nm$ which correspond with periods of commercially available Blu–ray, CD and DVD discs. As we will show in Section 5.1.1 the discs' patterns can be replicated to the polymer layers via soft

lithography. As can be seen from Figure 2.7 under the normal light incidence $\theta_i = 0°$ for $d = 1600\ nm$ the 0, 1st, 2th and 3th diffraction order is observed in whole visible range. For smaller periods the diffraction angles shift towards higher values resulting in disappearance of higher order diffraction above certain wavelengths. After backward diffraction the light passes once again through the active layer. Additionally, if the diffraction angle θ_m is greater then critical angle for total internal reflection at the multilayered interface the light can be reflected back and again coupled in the active layer. For simplification let as assume that refractive index of the active layer P3HT:PC$_{60}$BM is constant in the visible range $n_{active} \approx 2$ [67]. As a matter of fact the refractive index of conductive polymers varied in non-linear way across the wavelength (see [67] or Figure 4.5). For the active layer – glass boundary the critical angle amounts $\theta_c = 48.6°$. The conductive polymers, such as P3HT, absorb in visible range up to 400 nm [8], therefore based on Figure 2.7 the most suitable grating period to trap the light in the polymer absorption range seems to be 800 nm which correspond to DVD pattern. In one of our experiment (Section 5.1.1), on the influence of grating period on the absorption changes in a conductive polymer, we confirmed that the highest improvement was observed for grating with period around 800 nm.

In the last decades employing different periodic structures to improve the organic solar cells (OPV) performance has attracted much attention from research teams [64–66, 68, 69]. One of the first example of embossing diffraction grating in the active layer of OPV was presented by Roman et al. [68]. They used soft embossing to transfer triangular shape patterns with period 416 nm to the polymer layer. They observed the enhancement in device efficiency in the wide range of spectrum. They also examined separately a transversal and parallel part of polarizated light with reference to the plane of incidence. They showed that whereas for unpattern solar cell the external quantum efficiency is comparable for both polarizations, in case of pattern structure there is a visible increase in the efficiency for transversal light polarization. The similar observation was reported by Niggemman [65, 70] who examined a sinusoidal grating with a 720 nm period. The absorbance in the active layer increase about 8.7 % due to light-guide effect for transversal electric polarization (perpendicular to the light incidence plane) for wavelength greater than 650 nm. On the other hand, in case of transversal magnetic polarization most of the guided light is absorbed by aluminium causing 27% reduction in absorbance inside the active layer. Na et al. [64] showed that not only gratings' periods but also their heights affect the performance of OPV. The best results were achieved for structures with 20 nm grating height. Higher gratings deteriorate OPV through lowering of shunt resistance. The problem with reduction of fill factor for pattern structures was presented by [71] and also in one of our experiment (Section 5.1.1).

As can be seen event though integrated grating structures increase the optical path it does not always result in better OPV performance due to i.e. non–uniformity in metal contact [64]. In the section below we will present a different light trapping strategy which will not negatively affect the internal electrical properties of the devices.

External light scattering structures

The second option how to increase the chance of light absorption is to scatter the light inside a device. This can be done among others by texturing the light incidence surface of the devices.

One of the first theoretical description of influence of textured surface onto the absorption in silicon solar cells was made by Yablonovitch and Cody [72]. They showed that due to an isotropically scattering surface the average light path length can increase by $4n^2$, where n is the material refractive index. Their work was based on a few assumptions. Firstly, the textured surface was treated as a Lambertian surface which by definition reflects the light equally into all directions. Secondly, the thickness of the cell was greater than $\lambda/2n$ where λ is the light wavelength, so the wave optical effects can be omitted. Yablonovitch theory was confirmed in the work by Otto et al. [73]. The authors observed the appropriate absorption enhancement in black silicon sample due to additional textured layer. However, in case of organic solar cells the optimal thickness of absorbing layer is much thinner than the wavelength of incident light, so wave effects can not be neglected. Yu et al. [74] examined the light trapping in thin films through coupled–mode theory. They showed that with proper design of nanophotonic structures one can achieve even higher absorption enhancement than this which result from standard theory of light trapping applied for bulk structures.

To obtain the scattering effect both an internal and an external part of the device can be modified. Here, however, we will concentrate mainly on the external light trapping structures (Figure 2.6B). Compare to internal counterparts the external structures does not negatively interfere with the internal electrical properties [75]. Secondly, the structures can be fabricated independently from solar cells using soft–lithography or solution based techniques [12] suitable also for large scale production. Additionally, the structures can be applied to already optimized device configuration.

Tvingstedt et al. [76] propose to use external microlenses with additional metallic mirror with holes prepared by soft–lithography and self–assembly process. Polymer lenses with period 400 μm collimate and direct the incident light inside the devices, whereas the metallic mirror prevents the escape of light from the devices. In this way the authors observed enhancement in the absorption rate and photocurrent by 25% in organic solar cells. Myers et al. [75] showed that transparent polymer microllenes with diameter 100 μm increased efficiency of several different types of organic solar cell including polymer:fullerene bulk heterojunction (26% of relative increase of efficiency $\Delta\eta$), bilayer small molecules ($\Delta\eta = 56\%$) or hybrid devices ($\Delta\eta = 32\%$). Chen et al. [57] examined experimentally the influence of microlenses on organic solar cells performance and also conducted a simulation of electrical field distribution. Compare to [75,76] the features size were hundred times smaller from 0.6 to 2 μm. Based on the OPV current–voltage characteristic the highest relative increase in efficiency up to 10% was obtained for devices with microlenses 1 μm in diameter. Additionally, they observed that the efficiency of the OPV improves with an increasing depth of the microlenses. The experimental results were with agreement with simulations which
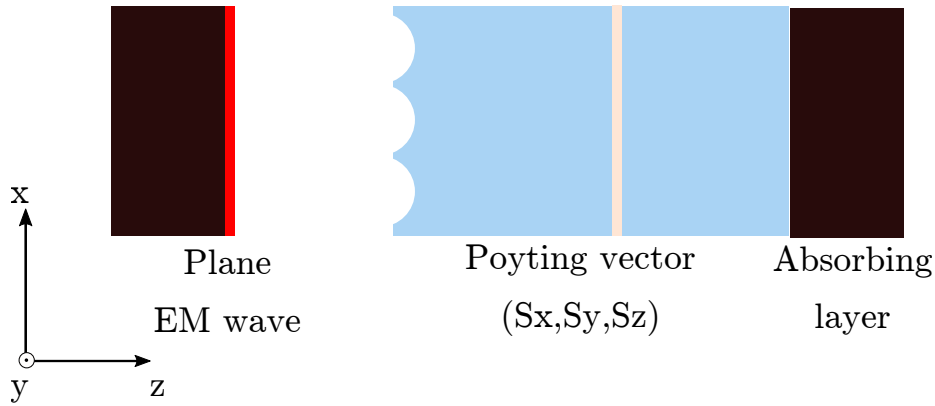
Figure 2.8: Schematic picture of simulated system. Plane monochromatic electromagnetic waves, propagating in z-direction, pass through porous polymer structures with a pore diameter (d) and a depression (sd). As the output the Poyting vector is determined.

also reveal the increase in the light path was results of light diffraction.

In all above experiments microlenses have convex character. In this thesis, however, we adopted a different approach namely we use external porous structures known as breath figures. The structures were prepared in a single step methods by deposition of a polymer solution either in a humid atmosphere or by additional small amount of water in the solution. In this way we obtained porous structures with various diameters up to 1.5 μm. As simulation and also our experimental results showed such structures not only reduce reflection but also change the direction of light propagation. The deflection angle strongly depends on porous diameters and also their depressions. The next section will summarized the most important results of simulation conducted by Dr. Jakub Haberko [77].

2.2.3 Light propagation through porous polymer layer

The goal of the simulation, performed by Dr. Jakub Haberko, was to evaluate the antireflection and light trapping capabilities of a porous polymer layer. To check the antireflection character the author determined the light transmittance through pores with different dimensions. In case of light trapping the deviation of the Poyting vector from the surface normal was calculated.

All of the results were based on solving Maxwell's equations for plane monochromatic wave propagating through pores. Figure 2.8 presents the schematic picture of the system. Simulation were performed by using Finite Difference Time-Domain. The analyzed structure were closed–packed polymer pores arrange in the triangular network. The pores diameter (d) and the depression (sd) varied between d: 0.3 - 1.8 μm, sd: 0.0 - 0.9 μm whereas the thickness of the polymer layer were fixed.
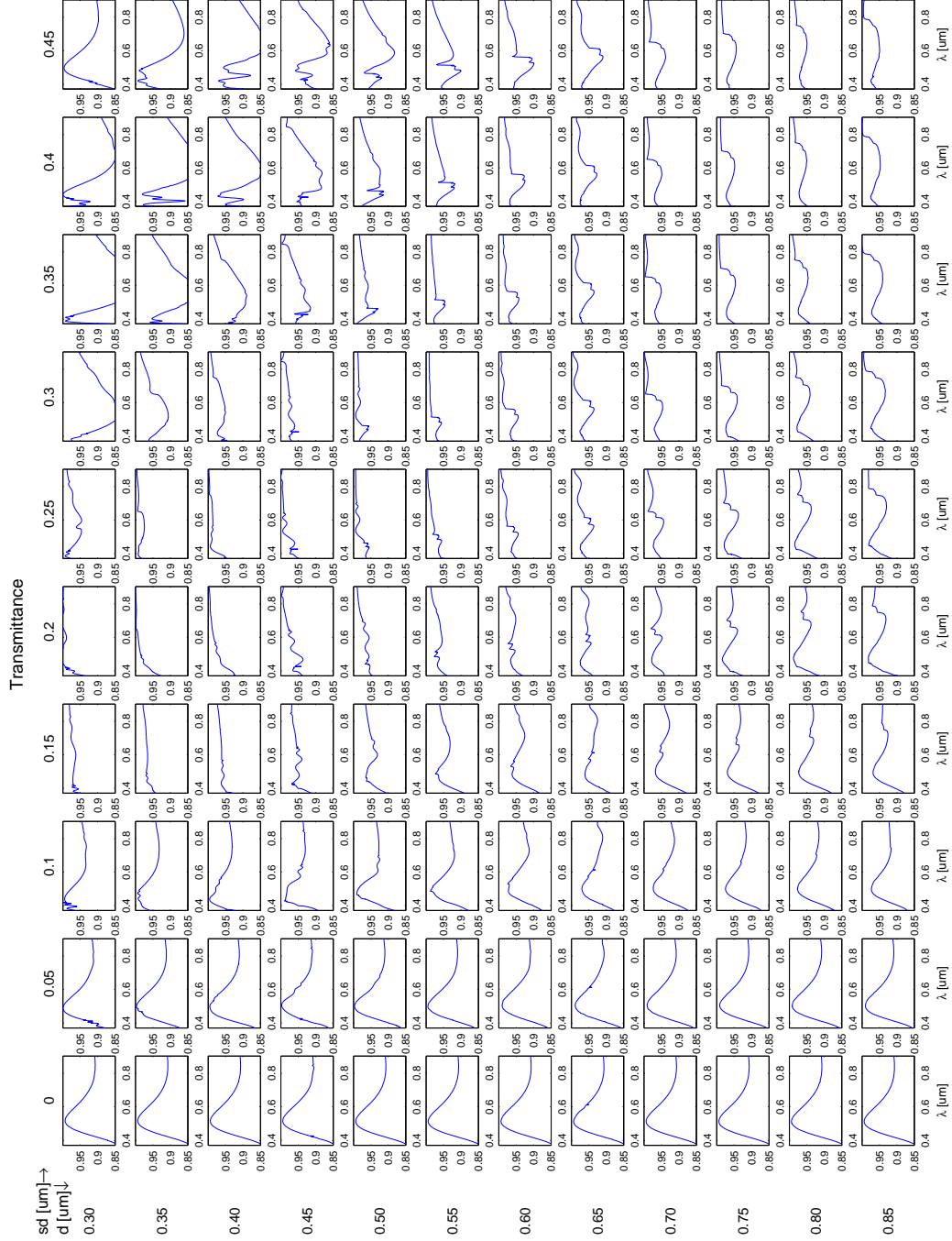
Figure 2.9: The simulation results for light transmission made by dr Jakub Haberko. The graph presents the transmission spectra for holes with different depression (sd) and the distance between the hole center (d).
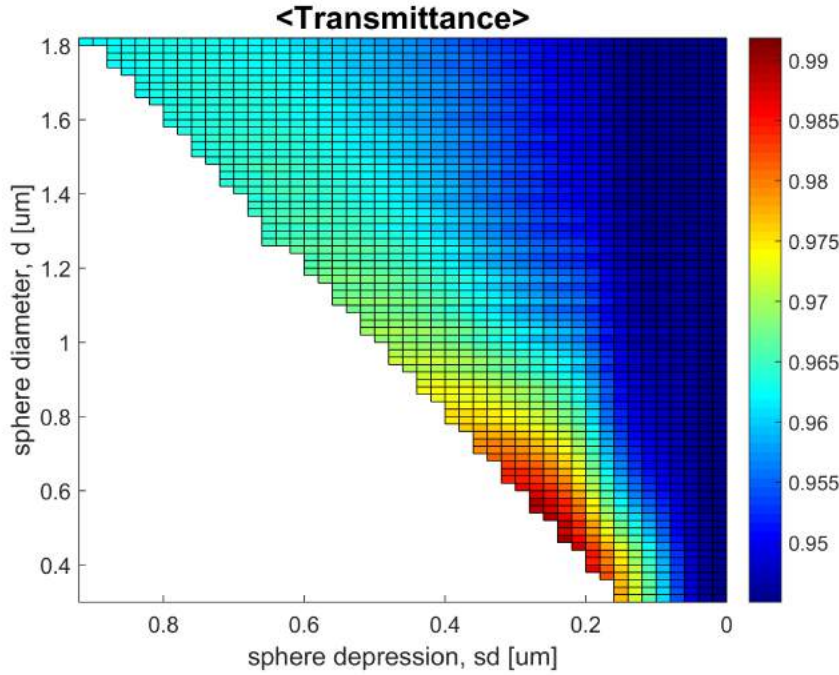
Figure 2.10: Simulation of transmittance prepared by dr Jakub Haberko. The 2D map presents the transmittance for holes with different depression (sd) and the distance between the hole center (d) The transmittance was calculated as a weighted mean (the weight was solar radiance spectrum).

Transmission   Figure 2.9 presents transmission spectra through porous structures for different pairs of diameter (d) and depression (sd). A flat polymer layer is represented in the first column as a structures with zero depression. As can be observed both parameters influence light propagation in a visible range, however the more pronounced changes are visible when the pores depression is changing. The highest transmission throughout whole spectra was observed for structures with sd: 0.2 - 0.25 μm and d: 0.3 - 0.4 μm.

To better explore the influence of pores dimensions the author calculated transmittance as a weighted mean, where weight was solar radiation spectrum AM1.5. The results are depicted on a 2D map of pores dimension presented in Figure 2.10. For a flat layer and structures with sd below 0.1 μm the transmittance amounts 94.6% and it is accordance with values 94.8% obtained from Fresnel equations. In the transmittance map we can distinguish some main regions; for structure with depression smaller than 0.1 μm independently on the diameter the transmittance doesn't exceed 95%. The slight improvement up to 96.5% was observed for pores with d: 1.2 - 1.9 μm and sd greater then 0.4 μm. The increased up to 98% were visible in the relative narrow region of sd: 0.18 - 0.28 μm and d: 0.3 - 0.6 μm. The best results 99.2% were obtained for sd: 0.22 - 0.24 μm and d: 0.44 - 0.46 μm. Such structures are most suitable as an

antireflection textures.

Light scattering   As simulation depicted the porous structure not only increase the light transmission but also can act as light scattering structures. The magnitude of scattering angle depends, similar as for diffraction grating, on the wavelength and the structures dimensions. As in the previous transmission simulation the main attention was paid to examine how the scatter angle depends on pores diameters (d) and their depression (sd) and for which pair (d, sd) the highest angle values are obtained.

The effective scattering angle we mentioned above is defined as an energy–weighted average of the angle of the outgoing wave. Mathematically this can be described by

$$\phi_{evg} := \frac{\langle \phi(x)E(x)\rangle_{x\in\Sigma}}{\langle E(x)\rangle_{x\in\Sigma}} \tag{2.8}$$

where x is a point on a 2d plane Σ parallel to the incoming wave and placed some distance after the porous structures, while $E(x)$ is the energy of the wave at point x, given simply by a length of a Poynting vector $\langle|S(x,t)|\rangle_{t\in[0,T]}$ averaged over one period. The angle $\phi(x)$ is the angle of the Poynting vector at point x. The denominator is the average of the weights and it normalizes the effective angle with respect to the total energy of the outgoing wave (so that for a constant $\phi(x)$ we have $\phi(x) = \phi_{avg}$). One can interpret formula 2.8 as the angle at which most of the energy leaves the system.

Figure 2.11 presents calculated effective scattering angle ϕ_{evg} for different pairs of pores diameters (d) and depression (sd). As can be seen, similar in a transmission map (Figure 2.10), the value strongly depends on both pores parameter. The most pronounced deflection, $\phi_{avg} = 22°$, was observed for d≈ 0.42 μm and sd changing from 0.12 to 0.2 μm. Additionally, for a wide range of structures the scatter angle exceed 11°. Interestingly, there are also some additional islands with increase in ϕ_{avg} which resembled the diffraction patterns.
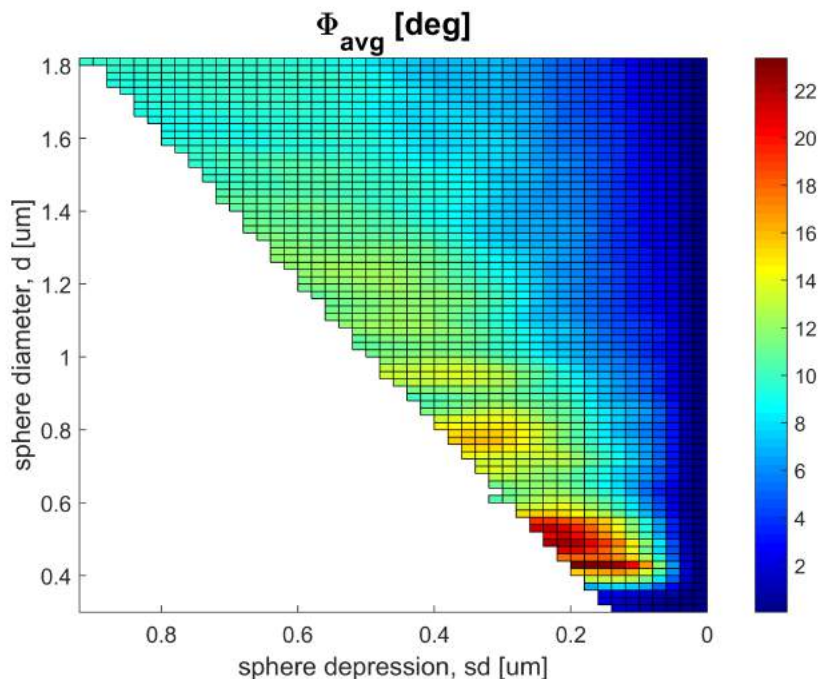
Figure 2.11: Calculated effective scattering angle for different hole depression (sd) and diameter (d). The simulation and calculation was performed by dr Jakub Haberko.

2.3   Phase separation

Mixing behaviour of two or more components (e.g. polymers or polymer and solvent) can be described in thermodynamics terms by analyzing the change in Gibbs free energy defined as [78]:

$$\Delta G_m = \Delta H_m - T \Delta S_m, \tag{2.9}$$

where ΔH_m is the enthalpy, ΔS_m the entropy of mixing and T is the temperature. The components are not miscible if $\Delta G_m > 0$ and miscible if $\Delta G_m < 0$. As ΔG_m can not be explicitly determined [22] approximate models have to be used to predict the mixing behavior. In 1940s Flory and Huggins proposed a mathematical model to calculate the change ΔG_m for mixing a polymer with a solvent.

2.3.1   The Flory-Huggins theory

Flory–Huggins theory combines a mean field theory and a lattice model. The lattice, graphically depicted in Figure 2.12, consists of n sites which are occupied either by polymer segment or solvent molecule. Let us assume that each polymer chain consists of N segments and in total there are n_p polymer chains. The remaining sites are occupied by n_s solvent molecules so that $n_s + N n_p = n$. Then the polymer volume
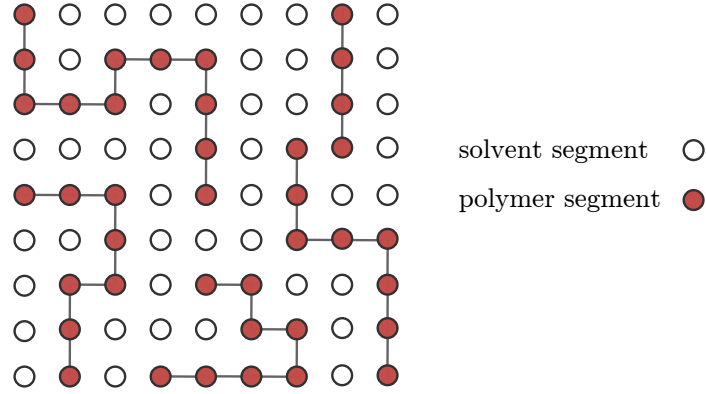
Figure 2.12: Lattice model for a polymer–solvent blend system. The red sites are occupied by polymer chains whereas the white by solvents molecules.

fraction can be expressed as:

$$\phi = \frac{n_p N}{n} \tag{2.10}$$

and solvent fraction

$$1 - \phi = \frac{n_s}{n}. \tag{2.11}$$

Using statistical mechanics one can calculate the combinatorial entropy of mixing (see [79]):

$$\frac{\Delta S_m}{k_B} = -\left[\frac{\phi}{N}\ln\phi + (1-\phi)\ln(1-\phi)\right]. \tag{2.12}$$

For polymers with large segment length N and low concentration ($\phi \ll 1$) the expression ΔS_m is small and the main role in miscibility is played by enthalpy. As Flory showed the enthalpy of mixing per lattice site is given by (for derivation see [80]):

$$\frac{H_m}{k_B T} = \chi\phi(1-\phi), \tag{2.13}$$

where χ is the Flory-Huggins interaction parameter determined by contact energies ε_{ij} between the i and j segments:

$$\chi = \frac{z}{k_B T}(\varepsilon_{PS} - \frac{1}{2}(\varepsilon_{PP} + \varepsilon_{SS})), \tag{2.14}$$

where z is the number of the nearest neighbors in the lattice, ε_{PP} is the contact energy between polymer–polymer segments, ε_{SS} solvent–solvent and ε_{PS} polymer–solvent. Depending on the relative strengths of interactions χ can have positive or negative values. Positive χ means that the polymer–polymer and solvent–solvent contacts are more favorable then the polymer–solvent, in contrary to negative χ where polymer–solvent contacts are preferred.

Combining Eq. 2.12 and Eq. 2.13 one obtains a Flory–Huggins equation for the polymer solution:

$$\frac{\Delta G_m}{k_B T} = \frac{\phi}{N} \ln \phi + (1 - \phi) \ln (1 - \phi) + \chi \phi (1 - \phi).$$ (2.15)

The first two terms in Eq. 2.15 represent the combinatorial entropy, the third term represents the enthalpy. While the entropy always promotes the mixing the enthalpy can either promote ($\chi < 0$) or oppose ($\chi > 0$) the polymer mixing. It is evident that χ plays an important role in mixing behavior. In Section 4.1 we will experimentally determine an interaction parameter χ between a new generation donor carbazole–based copolymer (PCDTBT) and solvents.

2.3.2   Flory-Huggins interaction parameter

Flory-Huggins theory is based on several assumptions [79]:

1. The volume and shape of polymer segments is equal to solvent molecules.

2. All polymer molecules have the same size.

3. There is no volume change of mixing and the interaction parameter χ is independent of composition.

In reality, however, these criteria are not satisfied. All deviations are compensated by making χ a function of the composition ϕ, temperature T or chain length N [78]:

$$\chi = \frac{\alpha(\phi, N)}{T} + \beta(\phi, N)$$ (2.16)

There are several experimental methods how to determine χ parameter such as osmotic pressure measurements, light scattering methods suitable for a low concentrated region or vapour pressure methods which can be applied for a wider range $0.3 < \phi < 0.8$ [81]. It this thesis we use an vapor-pressure method; the swelling of polymer layers due to the presence of solvent vapors (see Section 4.1).

Swelling of polymer films   A polymer layer swells in the presence of solvent vapors as the solvent molecules diffuse into the polymer layer. The process can be described analogous to the regular solution theory [80].

In a swelling experiment two equilibrium states are considered: 1) the equilibrium between solvent and its vapors, 2) the equilibrium between solvent molecules in the swollen polymer (polymer solution) and the vapors above them. In the first case the equilibrium is obtained when the vapor is saturated, the chemical potential is equal:

$$\mu_s(T, p_{sat}) = \mu_o + k_B T \ln (p_{sat}/p_o)$$ (2.17)

where μ_o is a chemical potential at reference pressure p_o In the second case for a given polymer volume fraction ϕ the chemical potential is equal:

$$\mu_m(T, p, \phi) = \mu_o + k_B T \ln (p/p_o). \tag{2.18}$$

On the other hand, chemical potential difference $\Delta\mu_s$ of solvent molecules between a solution and pure solvent can be calculated based on energy of mixing:

$$\frac{\Delta\mu_s}{k_B T} = \left(\frac{\partial}{\partial n_s} \frac{\Delta G_{mix}}{k_B T} \right)_{T,p,n_p} = \ln (1 - \phi) + (1 - \frac{1}{N})\phi + \chi\phi^2, \tag{2.19}$$

where n_p and n_s are numbers of polymers and solvent molecules.

Subtracting Eq. 2.17 and Eq. 2.18 and combining with Eq. 2.19 we obtain the expression which relates the relative partial pressure $p/psat$ with polymer volume fraction ϕ.

$$\ln(p/p_{sat}) = \frac{\mu_m - \mu_s}{k_B T} = \ln (1 - \phi) + (1 - \frac{1}{N})\phi + \chi\phi^2 \tag{2.20}$$

Additionally, if volume fraction ϕ is expressed as the reverse of relative film expansion $\phi = d_0/d$ and also N $\gg$ 1 then Eq. 2.20 can be approximated as:

$$\ln(p/p_{sat}) = \ln \left(1 - \frac{d_o}{d} \right) + \frac{d_o}{d} + \chi \left(\frac{d_o}{d} \right)^2 \tag{2.21}$$

By measuring the relative expansion of the polymer layer under the different vapour pressure one can calculate the interaction parameter χ between polymer and solvent.

2.3.3 Flory-Huggins interaction parameter and solubility parameter

For a non-polar mixture, where interaction between species is governed mainly by dispersion forces, the Flory–Huggins interaction parameter can be estimated based on the solubility parameter δ [78]:

$$\delta_i = \sqrt{\frac{\Delta E_i}{V_{seq}}}, \tag{2.22}$$

where V_{seq} is the volume of lattice segment and ΔE_i is the energy of vaporization. The ratio $\frac{\Delta E_V}{V_{seq}}$, known as cohesive energy density, can be understood as the interaction energy per volume between the molecules of the same types (polymers or solvents) ε_{ii} therefore:

$$\frac{\Delta E_i}{V_{seq}} = -\frac{z\varepsilon_{ii}}{2V_{seq}} = \delta_i^2 \tag{2.23}$$

The minus sign stems for the fact that it is assumed that polymers and solvents interact mainly by dispersion forces ($\varepsilon_{ii} < 0$), whereas the energy of vaporization is
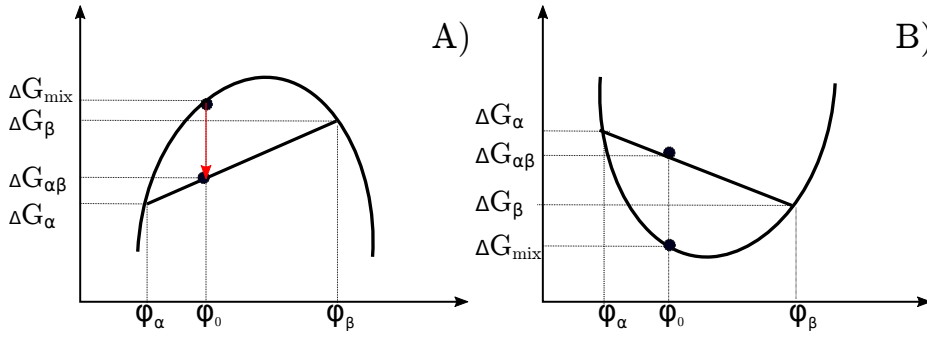
Figure 2.13: Composition dependence of Gibbs free energy corresponding to two states. A) Unstable, the system will minimize its energy by separating into two phases α and β, as $\Delta G_{\alpha\beta}(\phi_0) < \Delta G_{mix}(\phi_0)$. B) Stable, a one homogeneous mixture is more energetically favourable as $\Delta G_{mix}(\phi_0) < \Delta G_{\alpha\beta}(\phi_0)$.

positive [78]. If we substitute Eq. 2.23 to the definition of Flory-Huggins interaction parameter (Eq. 2.14) and assume that the interaction energy between polymer and solvent is given by $\varepsilon_{PS} = \sqrt{\varepsilon_P \varepsilon_S}$ we obtain:

$$\chi = \frac{V_{seq}}{RT}(\delta_P - \delta_S)^2 \tag{2.24}$$

Based on Eq. 2.24 Flory–Huggins interaction parameter χ should be positive, which is usually true for mixture with non–polar interactions between molecules (van der Waals forces) and not for systems with strong polar interactions [78].

Additionally, real mixtures do not always meet the assumptions of Flory–Huggins theory, resulting in discrepancies between the theoretical value calculated from Eq. 2.24 and an experimental one. Therefore, the interaction parameter χ is often modeled as a sum of enthalpic χ_H and entropic χ_S parts. The latter is usually treated as an empirical constant (for non-polar system $\chi_S = 0.34$) [81]:

$$\chi = \frac{V_{seq}}{RT}(\delta_P - \delta_S)^2 + 0.34. \tag{2.25}$$

2.3.4   Phase diagram

When physical parameters of a homogeneous mixture change it can decompose into two or more phases via a phase transition. A phase diagram is typically used to show which state is more energetically favorable in which physical conditions. In the case of polymer mixtures the relevant parameters are temperature, composition and interaction parameter so a phase diagram is usually plotted on a temperature vs composition or interaction vs composition plane [82].

Let us start with a homogeneous mixture with an overall composition ϕ_0 and the corresponding Gibbs free energy $\Delta G(\phi_0)$. The question is whether it is possible to
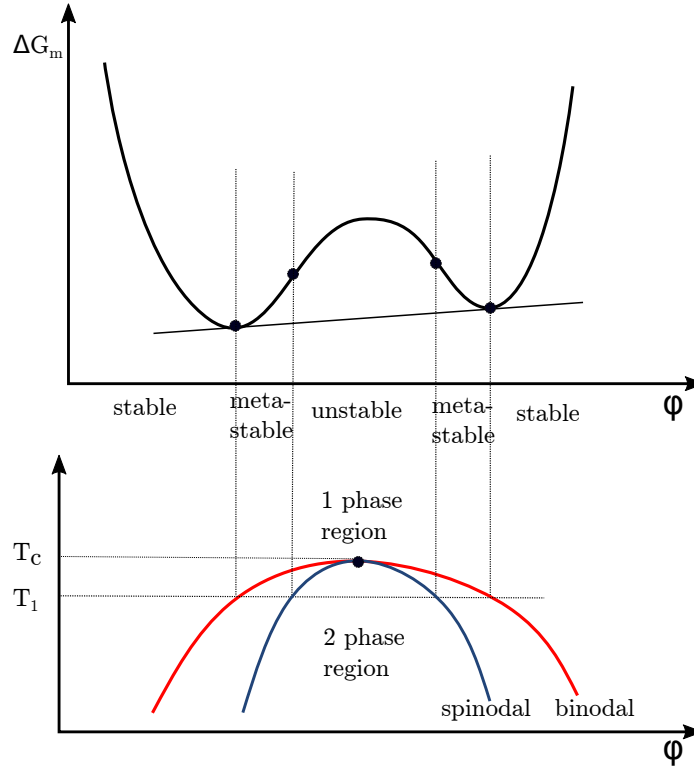
Figure 2.14: The free energy of mixing as a function of composition for a temperature T_1 below the critical temperature T_c and the phase diagram for binary mixture.

find two phases α and β with compositions ϕ_α and ϕ_β, the combination of which will be characterized by a lower Gibbs free energy $\Delta G_{\alpha\beta} < \Delta G(\phi_0)$. Assuming that phases α and β occupy the volume fractions g_α and g_β ($g_\alpha + g_\alpha = 1$), the Gibbs free energy is a weighed average of the free energies in each of α and β states, that is $\Delta G_{\alpha\beta} = g_\alpha \Delta G(\phi_\alpha) + g_\beta \Delta G(\phi_\beta)$. The compositions ϕ_α and ϕ_β can be chosen arbitrarily, however, the following condition has to be satisfied $\phi_0 = g_\alpha \phi_\alpha + g_\beta \phi_\beta$ because the total amount of both components is conserved. It follows that the free energy of the phase separated states is given by [78]:

$$\Delta G_{\alpha\beta}(\phi_0) = \frac{(\phi_\beta - \phi_0)\Delta G(\phi_\alpha) + (\phi_0 - \phi_\alpha)\Delta G(\phi_\beta)}{\phi_\beta - \phi_\alpha} \tag{2.26}$$

The value of $\Delta G_{\alpha\beta}(\phi_0)$ can be interpreted geometrically as the intersection point of a line connecting the value of ΔG at points ϕ_α and ϕ_β with a vertical line at $\phi = \phi_0$, this construction is schematically presented in Figure 2.13. It is visible now that for a concave curve (Figure 2.13A) it is more energetically favorable for it to separate into two phases since $\Delta G_{\alpha\beta} < \Delta G(\phi_0)$ for any ϕ_α and ϕ_β. On the other hand, for a convex curve (Figure 2.13B), $\Delta G_{\alpha\beta} > \Delta G(\phi_0)$, the homogeneous mixture is favorable for all initial compositions ϕ_0. To summarize the local curvature of $\Delta G(\phi)$ determines the local stability of the system.

In a case of partially miscible mixture, however, curve $\Delta G(\phi)$ has a more complex shape with both locally concave and convex sections, as is illustrated in Figure 2.14. The homogeneous mixture is stable only for compositions outside of the so–called miscibility gap given by the interval $[\phi_1, \phi_2]$. The values ϕ_1, ϕ_2 are determined by the common tangent rule:

$$\frac{\partial(\Delta G_m)}{\partial \phi}\Big|_{\phi=\phi_1} = \frac{\partial(\Delta G_m)}{\partial \phi}\Big|_{\phi=\phi_2} = \frac{\Delta G_m(\phi_2) - \Delta G_m(\phi_1)}{\phi_2 - \phi_1} \qquad (2.27)$$

Two further sub–regions can be distinguished inside the miscibility gap called un-stable and metastable regions, corresponding to locally concave and convex regions respectively (the inner and outer parts of the miscibility gap in Figure 2.14). For both cases the system will eventually separate into two phases with compositions ϕ_1 and ϕ_2, however, the mixture starting in a metastable region must rely on some spurious energy fluctuation to push one of the components over the inner hill. This results in geometrically different structures, the metastable mixture will decompose into two phases through nucleation and growth, while the unstable mixture will go through a spinodal decomposition. The nucleation and growth mode creates highly localized structures starting from scarce nuclei seeded by a random energy fluke required for the phase transition. In contrast, the spinodal decomposition does not need the addi-tional energy and thus it takes place uniformly through the mixture, creating complex structures, typically long wobbly interconnected paths.

At the end, by carrying out the above analysis for different temperature one can construct the phase diagram in temperature — composition plane (Figure 2.14). A binodal curve separates stable from metastable region and a spinodal curve metastable from unstable. These two curves are connected in so–called the critical point.

Ternary phase diagram   So far we have concentrated on a binary system such as polymer solution. However, the main part of the organic solar cell, the active layer, is commonly prepared from a ternary system: a mixture of a polymer and fullerene dissolved in a common solvent. In this situation the phase separation is initiated by reducing a solvent volume (solvent quench) in the mixture. The phase behavior can be analyzed analogously to the binary system starting from a generalized Flory–Huggins theory with Gibbs free energy given by:

$$\frac{G_m}{nk_BT} = \frac{\phi_1}{N_1}\ln\phi_1 + \frac{\phi_2}{N_2}\ln\phi_2 + \frac{\phi_3}{N_3}\ln\phi_3 + \chi_{12}\phi_1\phi_2 + \chi_{13}\phi_1\phi_3 + \chi_{23}\phi_2\phi_3 \qquad (2.28)$$

where ϕ_i is the volume fraction of i-th component (solvent, polymer or fullerene), N_i expresses the degree of polymerization and χ_{ij} are represent interaction parame-ters between components. To obtain binodal and spinodal curves, however, numerical computations are required. Because of the constraint $\phi_1 + \phi_2 + \phi_3 = 1$ the whole sys-tem has effectively two dimenssions and can be represented in a Gibbs concentration triangle [83] (Figure 2.15A) The corners correspond to pure components, the sides of
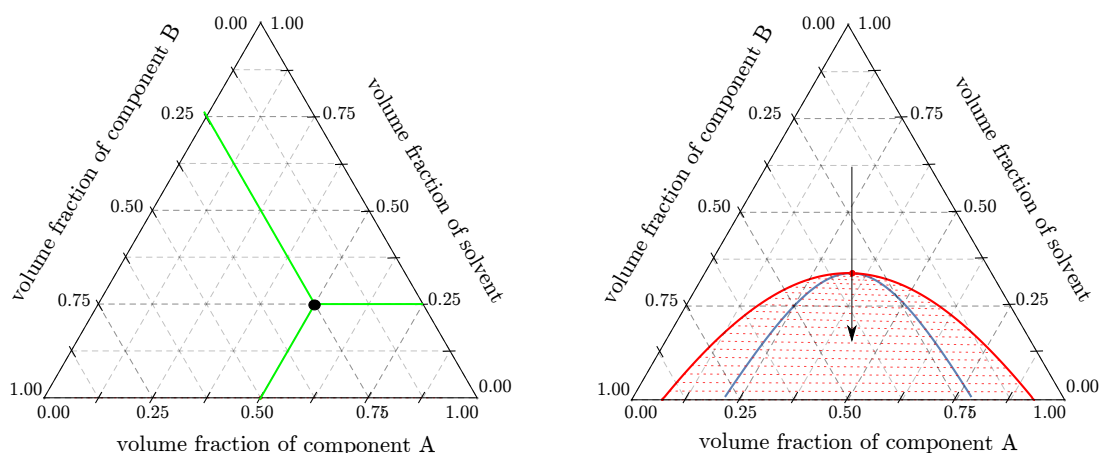
A)   B)

Figure 2.15: A) Triangular coordinates system with marked point corresponding to the blend with following proportion: 0.5 of component A, 0.25 of component B and 0.25 of solvent. B) Phase diagram for a ternary mixture - two components A and B in a common solvent. The red line corresponds to a binodal curve, the blue line presents a spinodal curve. As the solvent evaporate the system transits from one to two phase region along the marked path.

the triangle represent purely binary systems and each point inside the triangle represents a unique combination of three components. Figure 2.15B presents the schematic picture of transition from a stable one phase region to an unstable two phase region via solvent evaporation (solvent quench). One of the objectives of this thesis was to examine whether it is possible to predict the final morphology of a polymer:fullerene layer based on the ternary phase diagram. The phase diagrams were computed by Dr Paweł Biernat with a numerical algorithm [84]. The experimental results along with the phase diagrams will be discussed in detail in Section 4.2.1.

Chapter 3

Experimental

3.1 Thin polymer film preparation

Thin polymer films can be fabricated on both lab and large scales using different solution–based methods like coating (spin, blade, spray coating) or printing (ink jet, screen printing). In the presented thesis polymer films were mostly prepared by spin coating. Despite the popularity of this technique, also in organic solar cells production, it has limited scalability which makes a transfer to large–scale fabrication processes difficult. In comparison, linear coating techniques, like dip coating or blade coating, have better scalability potential. Below we present a relatively new technique, horizontal–dipping, which combines dip and blade coating. This technique facilitates creation of polymer films with thickness gradients, in turn optimizing the experimental procedures and finding optimal layer parameters: one experiment delivers a whole range of samples.

3.1.1 Spin coating

Spin coating is a one–step solution–based technique to prepare polymer thin films, it is widely used not only in the academia but also in the industry. A fabrication process can be divided into the following steps: Firstly a small amount of polymer solution is placed on a substrate rotating at high speed. At the beginning most of the solution is removed from the substrate, the rest is spread out, both processes are driven by centrifugal forces and viscous forces. A thin polymer film is formed after a complete evaporation of the solvent.

Despite a simplicity of the spin coating, models which describe the film formation are complex [85] and depend on many parameters such as angular velocity, polymer concentration, viscosity or diffusion parameter. In this project we mainly manipulate the rotation speed (ω) and the polymer concentration (c) to vary the thickness of the
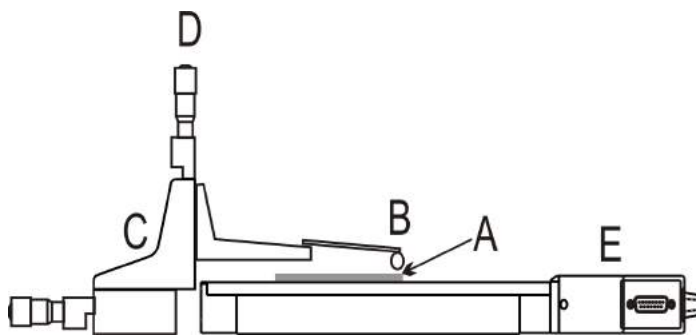
Figure 3.1: Diagram of home build system for H-dipping: A) substrate, B) cylindrical glass bar fixed to a microscopic slide, C) 3-axis linear stage, D) micrometer positioner, E) linear stage [86].

resulting layers (h). According to the Lewrence model these parameters are linked via a relation $h \propto c \cdot \omega^{-\frac{1}{2}}$ [85].

Polymer films studied in swelling experiment and light trapping layers were prepared under normal atmospheric conditions by a KW-4A (Chemat Technology) spin coater. Thin films used as active layers in organic solar cells were prepared in a glove box in an argon atmosphere to protect the layer from oxygen and humidity. The final film thickness was measured either by an ellipsometer or by analyzing the AFM profile of scratched films.

3.1.2   Horizontal dipping

Horizontal dipping (h–dipping) is a relatively new method introduced by Park at el. [87,88] to prepare layers with thickness gradients for organic solar cells and light emitting diode. It brings together a dip–coating and a blade–coating.

During dip–coating a substrate is first vertically dipped in a polymer solution. A film layer is formed during the withdrawing the substrate under a meniscus and a whole process is completed when the solvent evaporates. The faster the substrate is withdrawn the thicker is the film. During blade–coating a small amount of dissolved polymer is placed on a substrate. A blade, which moves parallel and close to the surface, spreads solution over the substrate. Similar to dip–coating the thin film forms after the evaporation of the solvent. During h–dipping [86,88,89], similar to the dip–coating, a wet layer of dissolved polymer is made by withdrawing a substrate under a meniscus of the coating solution. However, here the substrates moves horizontally as in blade–coating. Figure 3.1 presents a schematic diagram of a home build h–dipping apparatus [90]. A cylindrical glass bar, fixed to a microscopic slide, is mounted on a 3-axis linear stage (Newport 460A-xyz). Height and tilt can be adjusted by a micrometer positioner. A small amount of solution is placed between the substrate and the glass bar. Then, the substrate is horizontally set in motion by a computer–controlled linear stage (Newport UTS100). It can move either with constant velocity, which results

Figure 3.2: Schematic picture of h-dipping. A small amount of solutions is placed between a glass bar and a substrate. The substrate is next set in motion either with constant velocity or acceleration. After complete solvent evaporation the thin film is obtained. The film thickness depends on velocity v, bar diameter Φ, the distance between substrate and the bar d as well as on viscosity μ and surface tension σ [86].

in constant layer thickness, or with acceleration, resulting in layer with thickness gradients.

The film thickness can be estimated within a model proposed by Landau and Levich [91] which describes a formation of a wet layer behind the meniscus. For small capillary numbers $C_a = \frac{\mu v}{\sigma} \ll 1$ — where μ represents the viscosity and σ surface tension, and v is the drawing speed — a dry film thickness is equal:

$$h = 1.34 \left(\frac{\mu v}{\sigma} \right)^{\frac{2}{3}} R_d \kappa. \tag{3.1}$$

Here R_d is the downstream meniscus radius which depends on the diameter of a bar Φ and is constant for the constant height d (Figure 3.2), κ is the ratio between dry and wet film thickness.

The main advantages of h–dipping compared to the spin–coating is a possibility to prepare films with thickness gradients. Additionally, it can be easily implemented for large area and use in roll–to–roll processing. In contrary to the dip–coating only a small amount of the solvent is necessary to cover a large area of substrates. This thesis describes the first, to our knowledge, use of h–dipping, to prepare breath figure structures with diameter and depth gradients which are applied as the light trapping layers for organic solar cells. The analysis of the experimental results is presented in Section 5.2.3.

3.2 Self-organization and structural pattern

Over the last decades a lot of attentions has been paid to micro and nanometer structures formed in polymer films as suitable elements for optoelectronic devices or for biotechnology. The nanostructures can be formed in two different approaches: from the bottom up, where atoms or molecules are used to create the complex structures, or the from the top down, where the desire structures are formed after the removal or division of material [92]. Below we will describe two "top down" methods — soft lithography and breath figure — which we used for preparation of light trapping structures.
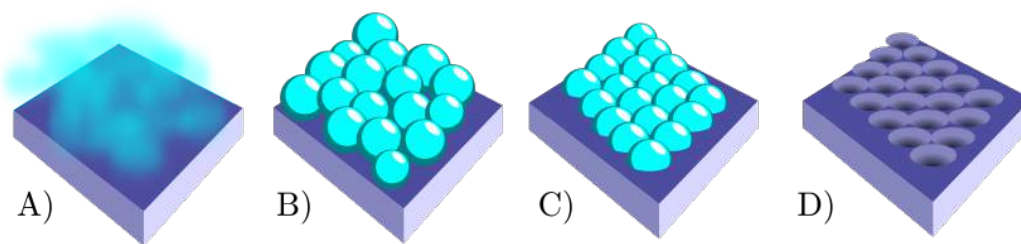
Figure 3.3: The illustration of the breath figure mechanism. Due to evaporation of the solvent (A) the solution surface is cooled and caused the nucleation of the water droplets (B), which then sink into the polymer solution (C). After the evaporation the porous pattern is formed (D).

3.2.1   Breath figure

Breath figures ware originally defined as the formation of water droplet arrays on a surface [93]. As Widawski et al. [94] showed in 1994, this phenomenon can be used to fabricate porous polymer films. Since then such polymeric structures have found many applications ranging from biomedicine, optics and ending with membranes [95]. In the presented thesis we used breath figure structures as a light trapping layer for organic solar cells, basing on a solution of poly–(methyl methacrylate). We focused on how the breath figure size affects the performance of devices, for that purpose we tested with several experiments to obtain a wide range of structures.

Breath figure formation in a polymer solution can be described as follows (Figure 3.3): due to solvent evaporation a temperature of the solvent decreases, promoting the water condensation on the surface of the solution. The solvent evaporation continuous resulting in a growth of water droplets, their spontaneous ordering and sinking into the polymer film. Subsequently, complete evaporation of both solvent and water results in a 2D or even 3D array of air bubbles, also known as honeycomb structure.

In practice, we can apply most of thin–film coating methods, discussed in Section 3.3, to prepare breath figures. For the purpose of this thesis we chose spin coating and horizontal dipping. It is worth noting that although spin coating is commonly used for breath figure preparation [96–98], to our knowledge, there are no studies devoted to formation of breath figures by h–dipping.

Breath figures are typically formed in high humidity environments, however, there are also low humidity techniques. One of them, proposed by Park et al. [97], bases on adding small amounts of water into the solution. In presented thesis breath figures were prepared in both high and low humidity.

In the high humidity case, we used a spin coater (KW-4A, Chemat Technology) extended with a system to adjust and control retaliative humidity in a coating chamber [99]. The first stage of the experimental setup consists of splitting a nitrogen flowing out of a container into two fluxes. One of the fluxes passes through a bubbler filled with water, producing vapors with relative humidity reaching 100 %. The other
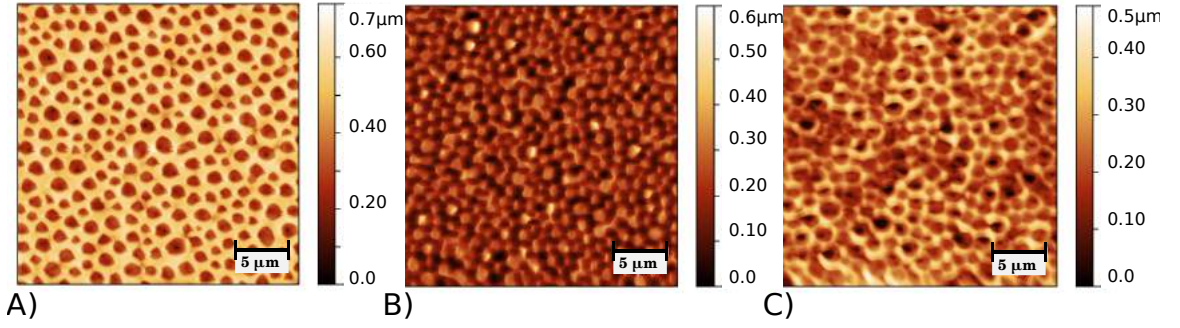
Figure 3.4: AFM images of three steps how to reproduce a porous structures prepared originally by breath figures. A) master: porous poly–(methyl methacrylate) layer prepared by breath figure methods, B) elastomeric PDMS stamp: a negative master pattern, C) replication pattern in polymer film obtained by Microtransfer molding using PDMS stamp

flux passes unaltered and mixes with the flux coming from the bubbler. We can actively control the relative humidity of the mixed flux by changing the mixing ratio, giving us a range of relative humidities between 40 to 90%.

For the low humidity experiment, we added water into a poly–(methyl methacrylate) solution, and used either spin coating or h–dipping without having to work in isolated chamber. The results with additional experimental details are presented in Section 5.2.

3.2.2 Soft lithography technique

Soft lithography is a collection of techniques (micro–contact printing, replica molding, microtransfer molding, solvent–assisted micromolding, etc.) to generate reproducible patterns in a large size range from 30 nm to 500 μm [100]. Compare to traditional microfabrication techniques like photolithography, electron–beam lithography, soft lithography is suitable in these disciplines where unconventional soft materials are used like biotechnology, medicine or organic electronic. Additionally, soft lithography do not demand any special condition resulting in lower production cost.

Generally, soft lithography can be dived into several steps: pattern design, master fabrication, stamp preparation and fabrication of structures by printing, embossing or molding with the stamp. Below we briefly describe which kind of masters and soft lithography technique we used during our experiments.

Masters and elastomeric stamp   For the soft lithography two components are crucial: a master and a stamp. Masters, from which the patterns are transferred into the elastomeric stamps, are usually prepared by conventional methods like electron beam lithography or photolithography These processes are time–consuming and require

advanced techniques. Recently, however, the non-lithography methods have been introduced. In was shown that, for example, self–assambled system are suitable as a pre–pattern for master. In the presented thesis masters were also prepared by two alternative non–lithography approaches. Firstly, for the periodic structures we used the commercial available optical storage media (CD, DVD or Blu–ray disc). This method was proposed for the classroom demonstrations and laboratory experiments [101]. Secondly, inspired by Yabu et al. [102] results, the porous patterns were prepared by using breath figure structures formed during the polymer deposition under high humidity.

The next step is to prepare an elastomeric stamp which is usually made of poly–(dimethylsiloxene). PDMS, commercially known as Sylgard 184, is a durable elastomer resistant to degradation. However, one of its main disadvantage is fact that it swells in many organic solvents [103]. Generally, solvents with a similar solubility parameter to PDMS ($\delta = 7.3$ (cal/cm)$^{1/2}$) swell better than these with a substantially different one. Lee et al. [103] ranked experimentally organic solvents according the swelling ability of PDMS.

In this thesis PDMS stamps were prepared by mixing prepolymer and curing agent at ration 10:1. The mixture was placed to the ultrasonic bath for 20 min to remove the air bubbles. Then the mixture PDMS was coated onto a master with desired pattern and cured at 100° for 40 min. At the end the stamp was peeled off from the master and was ready to use. Figure 3.4 shows an example of all three elements of soft-lithography: master, PDMS stamp and final patter.

Solvent-Assisted Micromolding (SAMIM)   This is one of the molding techniques in which the elastomeric PDMS stamp is wetted with a solvent and brought into the contact with a previously prepared polymer layer. Wherever the solvent–covered stamp comes in contact with the polymer the latter is dissolved by the solvent resulting in an impression complementary to the pattern on the stamp surface. A key element is to select a proper solvent which dissolves a polymer but does not cause the PDMS stamp swell. For our experiments we chose to use chloroform. Despite the fact that chloroform has relatively high solubility effect on PDMS [103] we haven't observed any noticeable degradation of PDMS stamp during experiments. SAMIM technique was applied to prepare period structures for external light trapping (Section 5.1.2) as well as to pattern active layer in organic solar cells (Section 5.1.1)

Microtransfer molding (μTM)   In this technique a drop of polymer solution is placed on the patterned PDMS stamp. Then by blowing through with a small stream of nitrogen a surplus solution is removed from the PDMS surface. Next, the stamp is brought into the contact with the substrate surface and press until the solvent evaporates. At the end the PDMS stamp is peeled away carefully leaving a relief the polymer pattern. By μTM not only two-dimensional pattern can be produce, but also

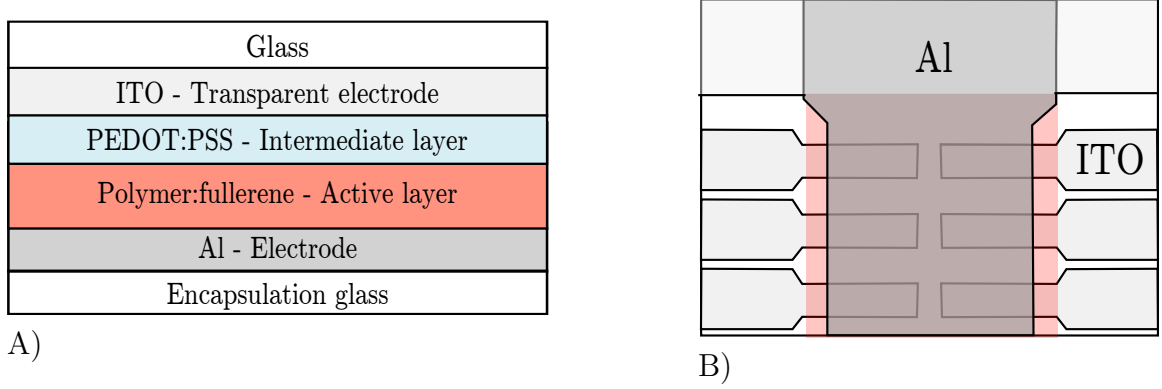| Glass |
|---|
| ITO - Transparent electrode |
| PEDOT:PSS - Intermediate layer |
| Polymer:fullerene - Active layer |
| Al - Electrode |
| Encapsulation glass |

A)

B)

Figure 3.5: A) Schematic picture of an organic solar cell: glass substrate with pre-pattern indium tin oxide acting as transparent electrode; buffor PEDOT:PSS layer improves holes injection from active layer to ITO; active layer - mixture of donor and acceptor - place where, in short, light is converted into electricity; B) The solar cells arrangement on the pre–pattern ITO glass. Each substrate consists of 6 individual pixels.

more complicated 3-dim structures as was presented by Zhao et al. [104], which can be applied in engineering or optics.

In the presented thesis we applied μTM to prepare periodic structures for light trapping application (Section 5.2.3). The main drawback of μTM, which we observed during the experiment, was the difficulty in obtaining the pattern from the whole stamp. This is not a problem in an experiment, in which the position of the pattern on the substrate is irrelevant, but in case of patterning the active layer in organic solar cell it can cause problems in device operation. Therefore for imprinting the active layer we chose SAMIM. In Section 5.1.1 using the same PDMS stamp we compared the SAMIM and μTM technique is sense of the reproducibility and patterns size.

3.3   Organic solar cells preparation

Organic solar cells (OPV) consist of several layers added in a certain order by printing, coating or by evaporation. Figure 3.5A schematically presents an OPV stack geometry which were used in the presented thesis. The role of these layers has been already discussed in Section 2.1.2. Here, however, we will describe how we prepared OPV devices. In general, our fabrication procedure was largely based on a manual prepared by Ossila [105] and can be summarized in the following steps: substrate cleaning, a buffor and active layer casting, a cathode evaporation and encapsulation.

Glass substrate and ITO electrode   All devices were fabricated onto pre–pattern indium tin oxide (ITO) glass substrates with 6 pixels per substrate, as is presented in Figure 3.5B. Substrates were purchased from Ossila Ltd. The size of glass substrate

O$_2$ plasma treatment	J_{sc} (mA/cm^2)	V_{oc} (V)	FF(%)	PCE (%)
20 s	2.38 $\pm$0.14	0.61 $\pm$0.01	67.0 $\pm$0.8	1.96 $\pm$0.11
100 s	2.31 $\pm$0.22	0.61 $\pm$0.01	67.0 $\pm$1.2	1.92 $\pm$0.20

Table 3.1: Performance parameters of organic solar cells based on P3HT:PC$_{60}$BM differing in ITO time of oxygen-plasma treatment.

amounts 20 mm x 15 mm, whereas a one ITO pixel has 4 mm x 1.5 mm. Based on the data–sheet thickness of ITO amounts 100 nm and resistance 20 Ω per square.

Firstly, all substrates were cleaned by ultrasonication in acetone and isopropyl for 30 min and blown dry with nitrogen. Then they were treated with oxygen–plasma (Zepto plasma cleaner, Diener Electronic, Germany) to remove organic contaminants, modulate ITO workfunction [10], increase the surface energy [106] and improve wettability. As Wagenpfahl et al. [107] showed too long oxygen plasma treatment results in S–shaped characteristic and decrease of OPV performance. As a preliminary experiment we checked two treatment times 20 s and 100 s. According [107] 100 s of oxygen plasma treatment should cause S–shaped characteristic. However, our results did not confirm this observation as we did not observe any significant differences in final OPV performance (Table 3.1). In both cases we obtained devices with a proper diode characteristic and high fill factor.

PEDOT:PSS The second layer, acting as a buffor layer, is poly(ethylene dioxythiophene):polystyrene sulfonic acid (PEDOT:PSS) which is a highly conductive, transparent in the visible spectral range and water–soluble polymer. PEDOT:PSS layer smooths the roughness of ITO and decreases the chance of shorts. Additionally, it improves holes injection from an active layer to ITO.

A thin PEDOT:PSS layer was prepared by spin coating. The rotation conditions were chosen based on results of our test measurement where we examined the influence of different rotation speeds on the OPV performance. The results are presented in Figure 3.6. As can be seen solar cells with PEDOT:PSS layer have better performance parameters compare to one without PEDOT:PSS layer. However, among different speeds there is no significant difference. For a subsequent PEDOT:PSS preparation we chose 4000 rpm resulting in PEDOT:PSS layer thickness approximately 60 nm. Our selection was dictated by the fact that at rotation speeds higher than 4000 rpm substrates frequently dropped out of the spin–coater's chuck.

After spin coating, to assure the proper contact between ITO and Al, part of PEDOT:PSS was removed from the cathode using the cotton bud soaked in distilled water. At the end all substrates with PEDOT:PSS were annealed at 150°C for 5 min on a hotplate and transferred into the glove box.

Active layer All OPV devices, prepared and analyzed for the purpose of this thesis, were based on so–called bulk heterojunctions. As a donor we used two poly-
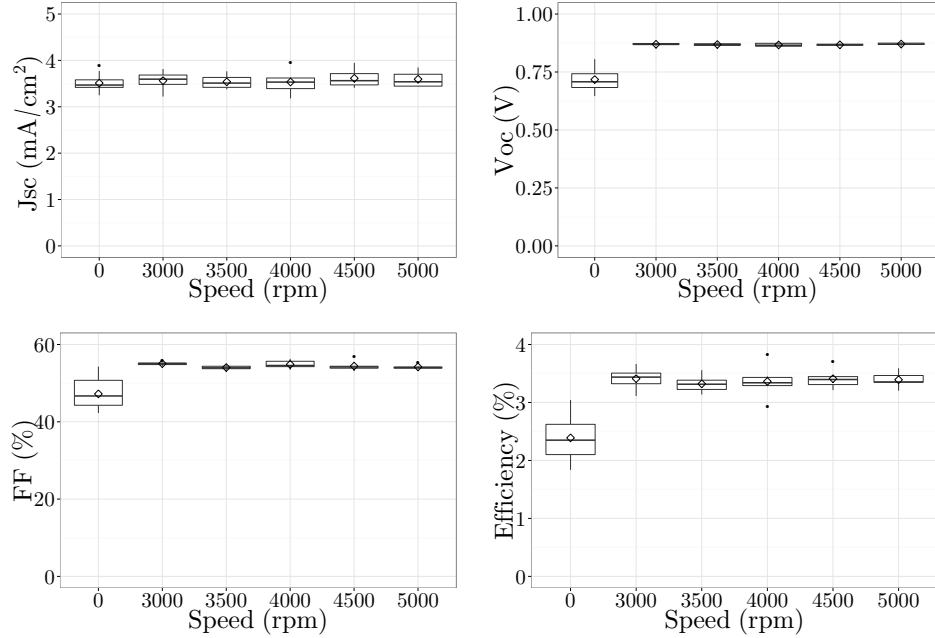
Figure 3.6: Performance parameters of organic solar cells PCDTBT:PC$_{70}$BM with PEDOT:PSS layer prepared at different spin-casting speed from 3000 to 5000 rpm. Solar cells without PEDOT:PSS is marked as the 0 rpm. The distribution of values are graphically depicted in boxplot. Here the central rectangle displays the interquartile range IQR (the data between the first Q1 and third quartile Q3), the band inside the box represents the median of data whereas the diamond symbol the mean value. The lower and upper whisker includes data within Q1 - 1.5xIQR and Q3 + 1.5xIQR, respectively. The results which are not included between upper and lower whisker are treated as outliers and marked as dots.

mers Poly(3-hexyl-thiophene) (P3HT) and Poly[N-9'-heptadecanyl-2,7-carbazole-alt-5,5-(4',7'-di-2-thienyl-2',1',3'-benzothiadiazole)] (PCDTBT), whereas as a acceptor two fullerene derivatives phenyl-C61-butyric-acid-methyl ester (PC$_{60}$BM) and phenyl-C71-butyric-acid-methyl ester (PC$_{70}$BM).

P3HT is one of the most investigated polymer in a field of organic solar cells [14] due to its high hole mobility, semicrystallinity and solubility in common organic solvents. P3HT ($M_W \approx 48900 mg/mol$), used in this work, was purchased from Rieke Metals. The polymer was dissolved prior to use in chlorobenzene with total concentration 20 mg/ml.

PCDTBT is the next generation donor polymer which characterizes with longer wavelength absorption and lower HOMO - LUMO levels, thus the OPV based on this material has high open circuit voltage up to 0.91 V and efficiency 7.2% [108]. PCDTBT is also more stable under ambient conditions compare to P3HT therefore it can be used for large area deposition as printing or blade coating. PCDTBT with

$M_w \approx 48900$ g/mol was purchased from Osilla and dissolved prior to use in chloroben-zene at 15 mg/ml concentration.

$PC_{60}BM$ and $PC_{70}BM$ are commonly used as acceptor materials mainly due to their good solubility, miscibility with polymer donor material and high electron mo-bility ($3.3 \cdot 10^{-2}$ cm^2/Vs) [25]. The materials (with purity $> 99\%$) were purchased from Solanne BV and were dissolved prior to use in chlorobenzene.

As a next step donor and acceptor materials were mixed together and kept on a hot plate at 60°C for at least 24 hours. As studies show the optimum PCDTBT:$PC_{70}BM$ blend ratio is 1:4 [109] whereas for P3HT:$PC_{60}BM$ it amounts to 1:0.6 [105]. To minimize the degradation of materials due to the presence of oxygen, water or light the preparation of solutions was carried out inside a glovebox.

Next, the active layer was formed by pipetting donor:acceptor solution onto a spinning substrate. Depending on which materials were used the following spin–coated parameters were chosen: for P3HT:$PC_{60}BM$ the layer was prepared under rotation speed 3000 rpm for 30 s, in case of PCDTBT:$PC_{70}BM$ the rotation speed amounts to 500 rpm for 60 s and then 2000 rpm for 10 s. To ensure the good connection between ITO and Al part of active layer was removed from the cathode strip using chlorobenzene.

Aluminium deposition and encapsulation   As a next step the substrates were placed into the evaporation shadow mask and put into the evaporation system. The aluminium electrode (80 nm thick) was thermally deposited on the top of the active layer with an evaporation rate of around 1.4 A/s. After aluminium deposition devices based on P3HT:$PC_{60}BM$ were thermally annealed at 150°C for 15 min whereas the solar cells with active layer PCDTBT:$PC_{70}BM$ did not require any additional thermal treatment.

Finally, to protect devices against degradation due to moisture and oxygen all of them were encapsulated using UV curable epoxy (Ossila Limited) and a glass slide.

3.4   Morphology characterization and analysis

3.4.1   Atomic Force Microscopy

Atomic Force Microscopy (AFM), introduced by Binning et al. [110] in 1985, is one of the scanning probe microscopy techniques which allows not only explore the surface topography but also measure some physical properties or be used for a surface lithog-raphy [111]. Compare to the electron microscopy AFM does not require any special environment (as high vacuum or low temperature) and can operate under ambient air or even in a liquid cell so it is suitable for analysis of biological objects.

The main AFM operation principle is based on the interaction between a sample surface and a sharp tip mounted on a cantilever. The interaction, commonly described by Lennard–Jonnes potential, cause either the deflection of the cantilever or can

change vibration properties of the cantilever. By detecting these changes it is possible to reproduce a sample surface topography.

The deflection of cantilever is generally measured optically using a light beam which is reflected from the end of cantilever and detected by a sensitive four–segment detector. Apart from the cantilever with a mounted tip and the detector another key element is a piezoelectric scanner, which allows to scan the surface by moving the tip or the sample and electronic feedback system.

There are several operating regimes depending on the distance between the tip and the sample surface – contact, non–contact or intermittent mode. The contact mode characterized by high resolution and fast data collection. However, it is not suitable for soft materials as it can modify or even destroy the surface. For the soft materials a better choice is the tapping or non-contact mode. The downside is that these modes are significantly slower.

In the presented thesis we examined rather rigid surfaces, so we used mainly contact mode. Topography measurements of polymer layers were performed by the Agilent 5500 (Agilent Technologies) or Nanosurf Flex. The AFM pictures were subsequently analyzed either by Fast Fourier Transformation or by Grain Analysis.

3.4.2   Fourier transformation

Two–dimensional Fast Fourier transform (FFT) is useful tool to examine quantitatively both anisotropic and isotropic morphological features. It decomposes the signal into the harmonic components from which one can extract the information about e.g. the period of the structure or their domain scale.

For isotropic picture (Figure 3.7A) FFT results in a diffusive ring. Based on the radial average of the squared FFT amplitude one can extract the maximum value and the corresponding radius $|k_{max}|$ which reverse defines the inherent domain scale R of the features ($R = \frac{1}{|k_{max}|}$). The result of FFT for anisotropic stuctures FFT (Figure 3.7B) is a set of diffraction peaks where $k = nk_\lambda$ ($n = 1, 2, 3, ...$). The period of the structures is determined as $\lambda = \frac{1}{k_\lambda}$.

3.4.3   Grain analysis

AFM images provide valuable information on surface morphology. In case of breath figures we were interested not only in their depths but also in their area, volume and boundary. For such analysis we chose Grain Analysis function from Gwyddion, a free open–source software for image analysis of probe microscopies [112].

The first step in grain analysis is to properly mark the features either by simple thresholding algorithm, such as height or slope thresholding, or, in case of more complicated data structures, by using a watershed algorithm. For our experiments we mostly used height thresholding as the examined pores had a strongly bimodal height distribution with two well separated peaks corresponding to the bottoms and edges of the pores so a threshold could be easily set as a value between these two
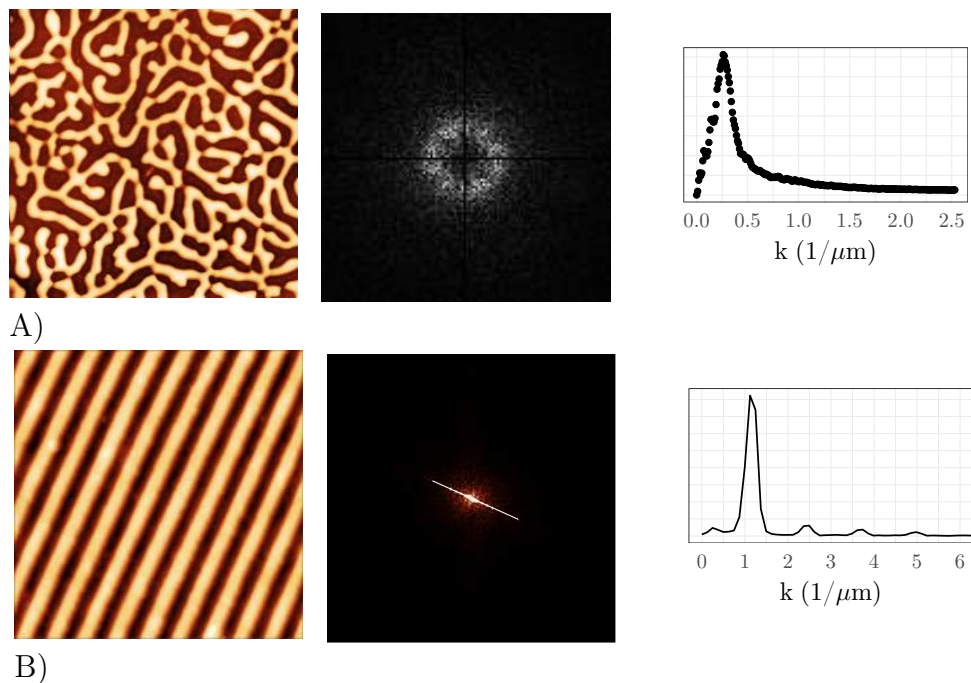
Figure 3.7: Schematic representation of 2D-FFT of isotropic (A) and anisotropic morphology (B) with resulting power spectra.

peaks. An example of such a bimodal height distribution with the selected threshold is presented in Figure 5.19 in Section 5.2.1.

After marking the features Gwyddion can extract information about the volume, area, size of depth of each feature. Based on these data one can calculate either a simple statistics like mean, median or variation. However, these summary statistics do not convey as much information as the distributions themselves. In this thesis we propose to use 2D maps representing the distributions of pore depths and diameters as in Figure 5.21. These distributions were extracted from Gwyddion and then analyzed in an open–source programming language R and plotted with the ggplot2 package.

3.5   Opto–electronics characterization

3.5.1   Spectroscopic ellipsometry

Spectroscopic ellipsometry is a nondestructive optical technique which allows to determine a layer thickness or materials dielectric parameters, such as refractive index $n(\lambda)$ and extinction coefficient $k(\lambda)$, in a wide range of wavelength. It is based on recording the changes in light polarization caused by reflection of light from a sample surface. The results of ellipsometry measurements are two angles Δ, Ψ related to the
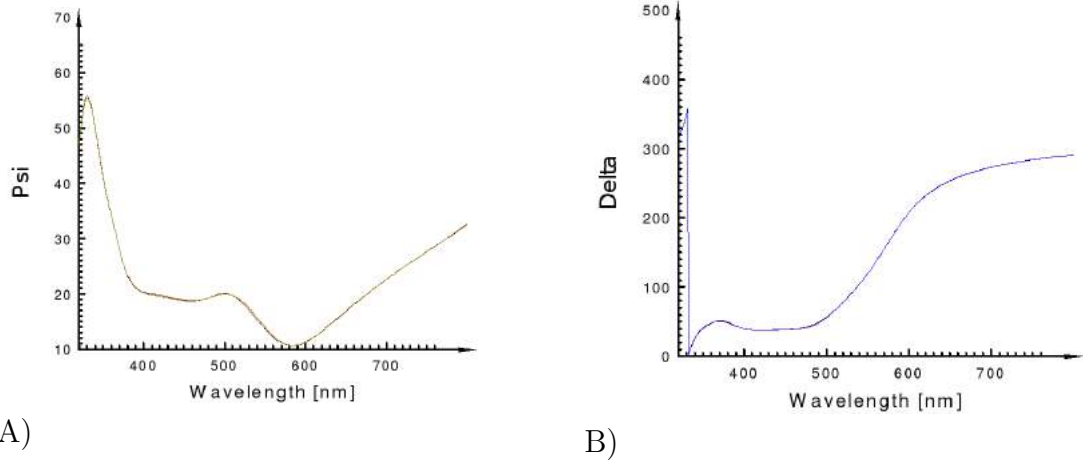
Figure 3.8: Example of ellipsometry output — recorded Ψ and Δ angles for absorbing polymer layer.

reflection coefficient ratio (ρ) for p- and s -polarization:

$$\rho = \frac{r_p}{r_s} = \tan(\Psi)e^{i\Delta}, \tag{3.2}$$

where Ψ represents the amplitude ratio and Δ phase difference between p- and s-polarized light waves. Figure 3.8 presents the example of recorded Δ and Ψ values.

In addition to many advantages such as high precision, fast measurement or possibility of real–time monitoring, unfortunately, ellipsometry is an indirect characterization method in which the measured values Δ and Ψ do not directly provide information about optical properties of materials. To unravel the optical parameters or a layer thickness from collected data an additional model analysis has to be performed. Depending on what kind of materials is analyzed (conductive, non–conductive, transparent or absorbing) the appropriate models has to be chosen such as: Cauchy (for transparent region), Drude (free–carrier absorption), Lorenz or Tauc–Lorenz (electric polarization in visible/UV region) model.

Measurement, Model and Fit While a spectroscopic ellipsometry itself is fast and straightforward, the major problem lies in selecting the optical model which will describe the experimental data. Difficulties arise among others for absorbing layers for which, compare to a transparent one, the optical parameters (n and k) are correlated with layer thickness. Below we briefly present the procedure which we used for modeling an absorbing polymer layer. The approach involves two steps. Firstly, we concentrated on the non–absorbing region, where only a refractive index n(λ) and thickness has to be found. For this region we apply the Cauchy model which gives good results for transparent films and allows to unravel thickness of a layer. As a next step, we have analyzed the whole measured wavelength spectrum (from 300 to 800 nm). During the modeling the layer thickness has been already fixed, the value

was taken from the previous non–absorbing region analysis. For optical modeling we chose the Tauc–Lorentz model [113], which was primarily design for amorphous materials. Tauc-Lorentz model is based on an oscillator expression for ε_2 (Eq. 3.3) and the Kramer-Kronig integral (Eq. 3.4).

$$\varepsilon_2(E) = \begin{cases} \frac{1}{E} \frac{AE_0C(E-E_g)^2}{(E^2-E_0^2)^2+C^2E^2} & E > E_g \\ 0 & E \leqslant E_g \end{cases} \tag{3.3}$$

$$\varepsilon_1(E) = \varepsilon_1(\infty) + \frac{2}{\pi}P\int_{E_g}^{\infty}\frac{x\varepsilon_2(x)}{x^2-E^2}dx \tag{3.4}$$

where E_g is the bandgap of the material (onset of the absorption), A the amplitude of the oscillator, E_o resonance frequency, C broadening of the oscillator. To get both refractive (n) and absorption (k) index from the Tauc–Lorenz model all of the above parameters have to be found. Figure 3.9 shows the final n and k spectra for absorbing polymer Poly(3-octylthiophene) obtained from Tauc–Lorenz. For a such layer the best result with the lowest mean square error (MSE = 0.4) which informs about deviation between the modeled spectrum and the measured data, was obtained using model with two oscillations. For the first one the parameters amount to $E_g(0) = 0.9$ eV, $A(0) = 0.29$, $E_0(0) = 3$ eV, $C(0) = 0.53$; for the second one $E_g(1) = 2.09$ eV, $A(1) = 11.62$, $E_0(1) = 2.6$eV, $C(1) = 0.5$. The typical polymer absorption spectrum is broad with additional shoulder. This phenomenon can be explained by the Franck–Condon principle.

At the end it is worth nothing that the more preliminary information about the layer we have (the position of absorption maximum, approximate layer thickness) the better fit can be obtained. All measurements, modeling and fitting were performed with software package SE-Advanced Module which was integrated part of the Sentech SE800 ellipsometer.

3.5.2   White light interferometry

The White Light Reflectance Spectroscopy (WLRS) allows to determine the thickness of the layers with nanometer accuracy. The main operation principle is based on the measurements of the light spectra reflected from the boundaries of layers with different refractive indexes.

In the presented PhD project we used WLRS to measure the thickness of thin polymer layer prepared on a Si substrate with well-controlled micrometer thick SiO_2 layer. For a such system the total energy which reaches the detector can be expressed by interference equation as [114]:

$$E = A + B\cos\left(\frac{4\pi n_1}{\lambda}d_1\right) + C\cos\left(\frac{4\pi n_2}{\lambda}d_2\right) + D\cos\left(\frac{4\pi(n_2d_2 + n_1 + d_1)}{\lambda}\right), \tag{3.5}$$
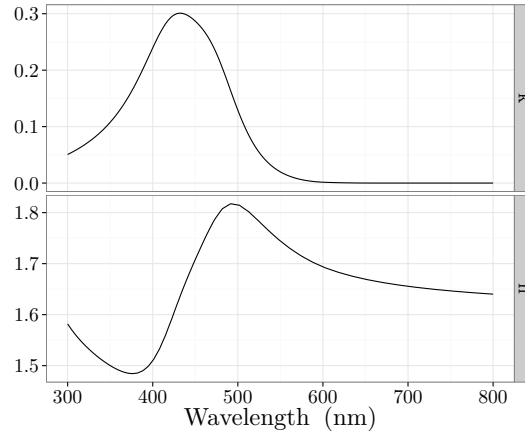
Figure 3.9: Wavelength depend of refractive index (n) and extinction coefficient (k) for P3OT determined with spectral ellipsometry using the Tauc-Lorentz model.

where $A(r_{01}, r_{12}, r_{23})$, $B(r_{01}, r_{12})$, $C(r_{01}, r_{12}, r_{23})$, $D(r_{01}, r_{12}, r_{23})$ are parameters depend on relative refractive indexes between adjacent layers (0 is air, 1 polymer film, 2 SiO$_2$ layer and 3 Si substrate) for example $r_{01} = \frac{n_0 - n_1}{n_0 + n_1}$.

By applying Eq.3.5 the film thickness as well as refractive index can be evaluated. However, in order to minimize the number of fitting parameters we previously obtained the refractive index $n_i(\lambda)$ of all layers with a spectroscopic ellipsometry. In this way by using WLRS only the thickness of layer were approximated.

3.5.3 UV-VIS Spectroscopy

Optical properties like absorption, reflection or transmission of thin polymer films are measured using a system built in our laboratory [115]. The main part of the system is a computer-controlled monochromator (Cornerstone 260 1/4m, Newport) equipped with automatic filter sorter and a beam splitter. The beam splitter, placed after monochromator, divides the light beam between a reference detector and the sample placed at the front of second detector. Signals from detectors (Amplified UV-Si Photodector, Newport) are measured using lock-in amplifier (Stanford Research System), the reference signal necessary for lock-in detection comes from optical chopper placed between light source and the monochromator.

For the absorption measurement we placed the sample in the path of the incident light. Based on the previously detected incident light intensivity $I_o(\lambda)$ and light intensivity after passing through $I(\lambda)$ we calculated the absorbance $A(\lambda)$ as:

$$A = \log \frac{I_o(\lambda)}{I(\lambda)} \tag{3.6}$$

Additionally to quantitatvely describe the absorption spectra we calculated the total
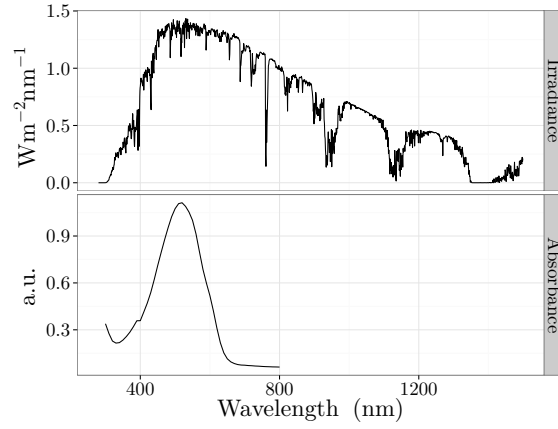
Figure 3.10: Example of measured absorption spectrum for Poly(3-octylthiophene) with presented on the top the solar spectrum.

absorptivitiy as:

$$A_T = \frac{\int A(\lambda)S(\lambda)d\lambda}{\int S(\lambda)d\lambda},\qquad(3.7)$$

where $S(\lambda)$ is Solar irradiance spectrum.

Chapter 4

Phase separation in polymer fullerene blends

Polymer blends have already found applications in numerous fields such as organic electronics, optics and biotechnology [116] mainly due to their ability to form variety of structures e.g lamellar, lateral, regular or hierarchic [117] with large size ranges; from nano to micrometers. Additionally, compare to metal or classic semiconductor, polymer blends can be dissolved and deposited as thin films in a one–step procedure by coating, printing or roll–to–roll techniques. During the solvent evaporation the polymer blends undergo phase separation resulting in a formation of different domains. Their final size and shape depend on many thermodynamic (temperature, pressure), processing (spin-coating speed) or material parameters (solution concentration, solubility parameter, miscibility of components, interaction parameter) [22,116]. As a performance of devices, based on polymer blends, is sensitive on the final phase domain structure the key issue in device optimization is to understand and control phase separation process.

In case of organic photovoltaics (OPV) an optimal phase domain size of the active layer is about 10 nm and should resemble a comb–like structure. This restriction is linked to a mechanism in which free charges are formed. Compared to their inorganic counterpart in OPV light absorption leads firstly to an exciton creation (electron-hole pair bounded with Coulombic attraction 0.3–0.5 eV [9]). In order to split the excitons into the free electrons and holes it is necessary to overcome the binding energy which is done when the exciton reaches donor-acceptor interface. However, the exciton diffusion path amounts only 10 nm [118]. Therefore to maximize the charge extraction from the OPV a donor–acceptor interpenetrating network should be prepared. In such system the exciton can reach donor–acceptor interface within its lifetime. Additionally, the interpenetrating network should form a continuous pathway to ensure that the free charges can reach the respective electrodes.

Although the last decades brought many optimization to OPV morphology through experimental methods [18, 19, 119], recently studies have been dedicated to modeling and predicting the polymer:fullerene blend behavior [20, 120–122]. In this part of the thesis, inspired by the results presented by Nillson et.al [123], we analyzed the carbazole–based copolymer (PCDTBT):fullerene ($PC_{70}BM$) behavior via ternary phase diagrams. We were interested whether based on the diagrams one can predict the final morphology of donor-acceptor film. The results are discussed in Section 4.2. Before we were able to construct the diagrams, however, we had to determine one of the key parameters in phase separation, namely the Flory–Huggins interaction parameter χ. In Section 4.1 we present how one can obtain χ based on polymer swelling.

In this experiment we concentrated on a particular blend system, PCDTBT and $PC_{70}BM$ dissolved in several solvents, which is nowadays one of the most efficient and stable donor–acceptor mixture used in the field of bulk heterojunction solar cells [2]. Despite such popularity of PCDTBT, to our knowledge, it is the first time when this system was analyzed via ternary phase diagram.

4.1   Swelling of polymer films

The starting point to construct a ternary phase diagram is to determine Flory–Huggins interaction parameters χ between polymer and solvents. The value of χ can be obtained experimentally via scattering, osmosis, vapor–pressure measurement or inverse gas chromatography [81]. For this project we chose another method based on a polymer swelling measurement. A polymer layer swells in the presence of solvent vapors because solvent molecules diffuse into the polymer film. An extent of swelling, according to the regular solution [80], depends directly on the value of interaction parameter between polymers and solvents. The swelling experiments have been already conducted in our laboratory to determine χ between poly(3–alkylthiophene)s and different volatile compounds [124]. However, it was performed manually. In order to optimize the whole procedure our first task was to build and program a new computer–controlled system, which we subsequently tested on a well–examined system polystyrene (PS)–toluene (TOL). Because there are already studies reporting $\chi_{PS--TOL}$ [125], [126], [127] we were able to compare χ_{PS-TOL} and to verify our methods (Section 4.1.1). Next, in Section 4.1.2 we describe the swelling behavior for a novel conductive polymer carbazole–based copolymer (PCDTBT) under different solvents vapor and we determine Flory–Huggins interaction parameter χ. To our knowledge, so far, there have been no reported χ values for PCDTBT and solvents. However, there are two references for solubility parameter δ_{PCDTBT} mainly 21.51 MPa$^{1/2}$ [128] and 23.8 MPa$^{1/2}$ [129]. As χ and δ are linked, we were able to, based on our swelling experiment, determine $\delta_{PCDTBT} = 22.8 \pm 1.2$ MPa$^{1/2}$, which is within the literature values (Section 4.1.3). It is worth to noting that the swelling apparatus was not only used for χ determination but also was utilized to measure an interdiffusion of PCBM into the polymer films [130].
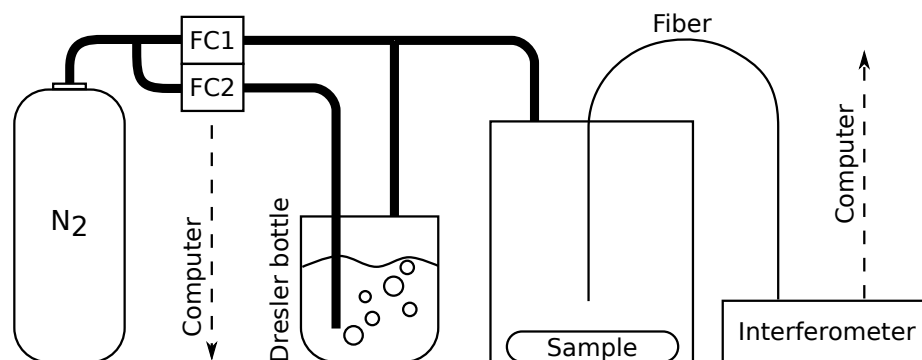
Figure 4.1: Schema of home build system for swelling experiment. Solvent with predetermined concentration is introduced to the measurement chamber via a dry nitrogen flux, which go through a Drechlser's bottle containing the respective solvent. The swelling of polymer film due to exposure to solvent vapors is measured with white light interferometry

Experimental

Sample preparation   For control measurement we examined a thin polystyrene (PS) layer prepared onto thermally oxidized silicon wafers. The SiO_2 was used to increase the accuracy during the measurement of polymer thickness by White Light Reflectance Interferometer (FRBasis Thetametrisis) [114]. PS ($M_W = 58$ kDa) was firstly dissolved in chloroform with total concentration (20 mg/ml) and then spin-coated (1000 rpm) onto the Si wafer with micrometer thick SiO_2 later. In the main part we examined Poly[N-9'-heptadecanyl-2,7-carbazole-alt-5,5-(4',7'-di-2-thienyl-2',1',3'-benzothiadiazole)] known as PCDTBT with $M_W = 61600$ g/mol. This polymer was dissolved in chloroform with total polymer concentration 15 mg/ml and then spin-coated with rotation speed 2000 rpm onto the thermally oxidized silicon wafers with 1010 nm (according the ellipsometry measurement) thick silicon dioxide layer.

Optical characterization   The spectroscopic ellipsometry measurement (The Sentech SE800, Sentech Instruments GmBH) was performed in a range between 320 nm - 800 nm under the constant incidence angle of 70°. Optical parameters (n,k) for PS layer were obtained using Cauchy dispersion formula. In case of PCDTBT we performed modeling in two steps. Firstly, we applied the Cauchy model for the non-absorbing region PCDTBT (from 650 nm - 800 nm) to extract the polymer layer thickness. Next, we used the Tauc-Lorentz model over a wider wavelength range to get optical constants; refractive index (n) and extinction coefficient (k) which were subsequently used by White Light Reflectance Interferometer.

Swelling examination   Figure 4.1 presents the schema of apparatus used during a swelling experiment. The system consists of nitrogen inlet, mass flow controllers con-

nected to the electromagnetic valves which control the nitrogen flows, the Drechsler's bottles filled with appropriate solvent, gas mixture and the chamber where the examined polymer film was placed. The gas flows was set to 2000 mL/min resulting in gas saturation within the chamber. The concentration of solvent vapors was regulated by mixing two components in varying proportions. The first component was simply a pure stream of nitrogen, while the second component was nitrogen carrying a steady amount of solvent vapors coming from a Drechlser's bottle. We manipulated the proportions of these components to regulate the concentration of solvent vapors in the swelling chamber. The changes in thickness of the polymer layers exposed to the solvent vapors were measured and recorded in real-time using a white light interferometer (FRBasis Thetametrisis).

4.1.1   Control measurement

After assembling and programming the swelling set–up with computer controlled flow meters (Figure 4.1) we performed a testing measurement on a well known polymer system polystyrene (PS) swollen in toluene vapor. Based on the experimental data we calculated the Flory-Huggins parameter which was next compared with the literature values [125–127].

The typical swelling experiment was conducted in a few steps. Firstly, using the ellipsometry we determined the optical parameters of polymer layer necessary for valuing the changes in layer thickness during the swelling experiment. In a case of polystyrene layer as well as SiO_2, which are transparent and non-conductive materials, a simple Cauchy model was applied to obtained the refraction index $n(\lambda)$. For a PS layer the refraction index has the following form: $n(\lambda) = 1.614 + 12.4 \cdot \lambda^{-2} + 88.1 \cdot \lambda^{-4}$ where λ is expressed in nm. Next the sample was transferred into a small chamber and placed horizontally under bifurcated optical fiber guides connected to the white light interferometry setup (Figure 4.1) which measured in real time the thickness of polymer layer. The swelling experiment begun with exposing the polymer layer to dry N_2, during this time the initial polymer thickness was evaluated ($d_0 = 93.7\pm0.1$ nm). Then we changed the relative partial pressure p/p_{sat} in the chamber by varying the ratio of dry N_2 to N_2 passing through the bubbler with the solvent. The detailed description of bubbler-based vapor generators is discussed in [131].

Figure 4.2 shows a typical polymer layer behavior under the vapor exposure. If the polymer layer is brought into contact with vapor, solvent molecules diffuse inside causing an increase of distance between polymer chains [132], resulting in an increase of the polymer layer thickness. The higher the relative partial pressure the bigger the swelling. The constant thickness is achieved when the polymer and vapor phases are in an equilibrium. In the presented experiment, however, the polymer layer did not reach the equilibrium, instead we observed an ongoing change in thickness. For low relative pressure ($p/p_{sat} < 0.454$), after a rapid reaction to the solvent vapors, the polymer layer slowly approaches to the equilibrium state. For higher relative pressure we observed that, the polymer layer first rapidly swell, but then the layers thickness
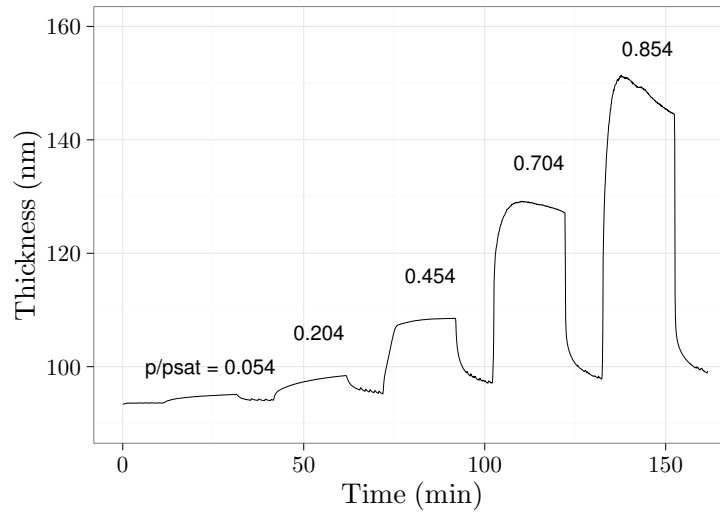
Figure 4.2: Control measurement: Thickness expansion of polystyrene (PS) layer exposed to the sequence of toluene vapors with different relative partial pressure.
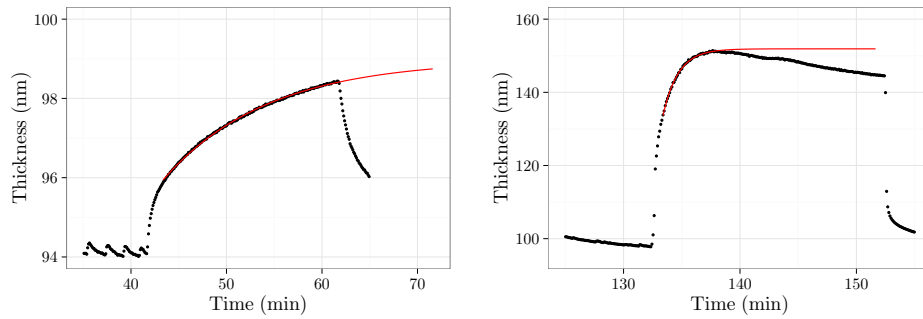

Figure 4.3: Example of ongoing changes in thickness of polystyrene film due to the presence of vapor. To determine the final thickness of the swollen polymer the exponential convergence (Eq. 4.1) was used.

starts to decrease. Such visible drop can be caused by several factors. The first factor could be associated with problems with saturation. As Mayer et al. [131] showed, in their work related to degree of saturation in a bubbler system, in order to reach a full saturation the liquid height should not be less then 40 mm. During our experiment a solvent level in the bubbler has visibly dropped because of solvent evaporation and the fact that the solvent leaves the bubbler carrier the nitrogen gas. The second factor is the decrease in liquid temperature during the bubbling [133]. The liquid evaporates into the gas bubbles and by removal of vaporization heat the temperature of the liquid rapidly drops. As Love et al. [134] demonstrated, under the flow rate 500 sccm through the water, the temperature of the system sharply drops by about 4.5 C° in the first 15 minutes and only after that slowly returns to the the equilibrium state. As they pointed out the lag time depends on many parameters like liquid type, mass or flow rate. The drop in the temperature causes a decrease in the partial pressure of the vapors which could be reason for lesser polymer swelling especially for high gas flow rates.

To calculate the Flory-Huggins interaction parameters from the swelling experiment we have to determine the final thickness of the swollen polymer layer. In our case, because of the ongoing changes in thickness, we needed to fit a model. As Berens et al. [132] proposed, the swelling mechanism can be described as a combination of two processes: diffusion and polymer relaxation.

As Berens et al. [132] observed the asymptotic approach to the equilibrium state can be modelled as a simple exponential convergence. Therefore if we consider only the long-time diffusion the thickness changes can be modeled with the following equation [135]:

$$d(t) = d_{eq}(1 - Ae^{-\alpha^2 t}) \qquad (4.1)$$

where d_{eq} is thickness in equilibrium, A and α are characteristic constants. Figure 4.3A shows that the experimental data obtained for low relative pressure (p/p$_{sat}$ < 0.454) reflect the exponential convergence (Eq. 4.1). For the results collected under high relative pressure we considered only the initial part of the data, corresponding to an increasing thickness (Figure 4.3B). As was mentioned before, the drop of the thickness could be related to either saturation problems or lowering the relative pressure in the chamber and it is not comply with the diffusion model.

After extracting the final polymer thickness d_{eq}, for each vapor pressure sequence, we calculated the Flory-Huggins interaction parameter χ using the expression binding the Flory-Huggins parameter χ, relative vapor pressure p/p_{sat} and reverse of relative film expansion d_0/d_{eq} (see Section 2.3.2):

$$\ln\left(\frac{p}{p_{sat}}\right) = \ln\left(1 - \frac{d_0}{d_{eq}}\right) + \frac{d_0}{d_{eq}} + \chi\left(\frac{d_0}{d_{eq}}\right)^2. \qquad (4.2)$$

Figure 4.4 compares calculated interaction parameters χ between polystyrene and toluene with reported literature values obtained by a similar experimental technique, however, in different ambient temperatures. The literature data cover a wide range of
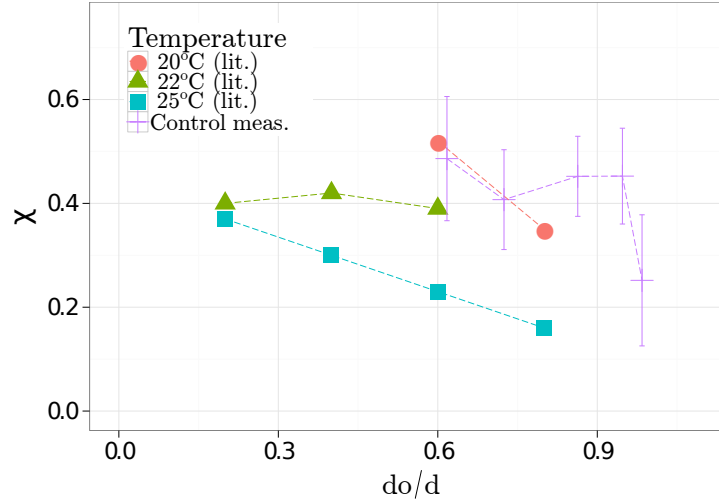
Figure 4.4: Interaction parameter χ between PS and toluene for different polymer volume fractions $\frac{d_0}{d}$ and temperatures. We compare χ from our measurement method with literature data collected for different temperatures: 20°C [125], 22°C [126] and 25°C [127].

polymer concentrations $\phi_p = d_0/d$ from 0.2 to 0.8, whereas we concentrated mainly on the high concentration range $\phi_p > 0.65$. If we compare the values we see that our results for $\phi_p < 0.8$ are in a good agreement with studies performed by Baughan [125] in temperature 20°C (our experiment was conducted under the ambient temperature 22 ± 1°C). Unfortunately, we do not have any temperature control mechanism inside the measurements chamber so the temperature of the examined polymer film could be changed during the experiment. For ϕ_p between 0.8 and 0.95 χ oscillates around 0.45, without a clearly visible trend, while for $\phi_p = 0.98$ there is visible decrease down to 0.25.

Summing up we showed that the presented set-up with computer controlled flow meters is suitable for an indirect measuring of the Flory-Huggins interaction parameters. The calculated Flory-Huggins parameters were comparable with literature values, despite the fact that we did not achieve the thickness saturation. The lack of saturation was mitigated by fitting an exponential model to obtain the final thickness.

4.1.2 Swelling of PCDTBT films

We dedicated the main part of the swelling experiment to explore the response of novel carbazole-based copolymer layer (PCDTBT) on different solvent vapors: chloroform, chlorobenzene, dichlorobenzene and toluene. PCDTBT has aroused great interest as a donor material for bulk heterojunction solar cells. The solar cells based on PCDTBT:PC$_{70}$BM mixture are characterized by a high open-circuit voltage, high-
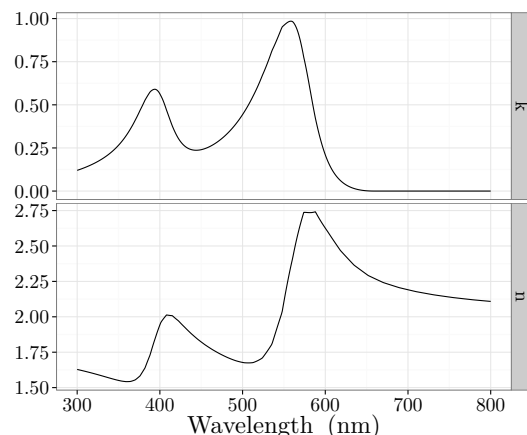
Figure 4.5: Wavelength depend of refractive index (n) and extinction coefficient (k) for PCDTBT determined with spectral ellipsometry using the Tauc-Lorentz model.

efficiency up to 7.5% and the possible life time up to 7 years [136]. Moreover, as Park et al. [109] showed, the internal quantum efficiency can be close to 100% which means that almost all absorbed photons generate carriers, which are subsequently collected by the electrodes. Despite the fact that PCDTBT is widely used, little attention has been paid to quantify an interaction parameter between PCDTBT and solvents. Information on this parameter can help to predict the phase separation behavior in donor–acceptor mixture and streamline an OPV optimization process. The goal of this part of thesis was to determine the Flory-Huggins interaction parameters, based on the swelling behavior of the polymer and, subsequently, construct a polymer-fullerene-solvent phase diagram.

The swelling experiment was performed analogously to the previously described control measurement. Compared to the polystyrene, however, PCDTBT is characterized with more complex dispersion relation because of its light absorption in the visible range. Therefore instead of working with a Cauchy model when modeling the ellipsometry results we used Tauc-Lorentz model, which is more suitable for absorbing amorphous materials like polymers, absorbing dielectrics or semiconductors. The procedure of determining optical parameters (n,k) for absorbing polymer layer is described in more detail in an experimental section (see 3.5.1). Figure 4.5 presents the resulting refractive (n) index and the extinction coefficient (k) for a thin PCDTBT layer. Compared to early stage donor polymers like poly–(phenylenevinylene) or poly–(thiophnene) derivatives PCDTBT exhibits two broad absorption peaks at around 390 nm and 560 nm which enhance the chance of light absorption due to the wider overlap with the solar spectrum.

During the swelling experiment polymer film was exposed to the sequence of N_2 fluxes carrying the solvent with different relative partial pressures p/p_{sat} inside a measurement chamber. After the polymer film was brought into contact with va-

por, solvent molecules diffuse into the polymer film causing an increase in distances between polymer chains [132], increasing in polymer layer thickness in the process. Each sequence was next separated by pure N_2 fluxes when the polymer film relaxed to its original thickness. During the experiment the relative partial pressure in the chamber varied from 0.05 to 0.85. Figure 4.6 presents the whole sequence of relative PCDTBT layer expansions d/d_0 under four solvent vapors with different relative partial pressures in the chamber. The initial thickness d_0 was calculated as an average of the thicknesses measured in the first 10 minutes of the experiment when the partial pressure was close to zero.

As with the previous experiment, we observed a rapid increase in thickness as a reaction to solvent vapors. If we compare the collected data we immediately notice that the swelling dynamic varies between the solvents. In case of chlorobenzene and dichlorobenzene for each exposure conditions we observed ongoing increase in thickness (with different rates of reaching a saturation state for the two solvents). In case of chloroform and toluene, for higher relative pressure, after swelling rapidly the layer starts to deflate. For chloroform the onset of such behavior was observed already for $p/p_{sat} = 0.354$. One of the possible explanations is that chloroform is a highly volatile solvent, characterized by high vapor pressure (21 kPa at 20°C) and low enthalpy of vaporization (31.4 kJ/mol). This is significantly higher then toluene ($p_{vap} = 2.93$ kPa at 20°C, $\Delta H = 38$ kJ/mol), chlorobenzene (1.2 kPa at 20°C, 41 kJ/mol) or o-dichlrobenzene (0.1 kPa, 48 kJ/mol) [137]. As we suggested in the previous part, the decrease in thickness could be caused by a drop in the partial vapors pressure, in turn caused by a temperature drop during the vaporization process. Based on solvents parameters, the biggest drop should occur for chloroform which is in agreement with our observation.

4.1.3   Interaction parameters between PCDTBT and solvents

To calculate the Flory-Huggins parameter χ, which describes the interaction between polymer and solvent, we followed the same procedure as during the control measurement. Firstly, to obtain the final thickness of the swollen layer, we fit an exponential model (described by 4.1) to our collected data as is presented in Figure 4.7. Then for each vapor pressure sequences we calculated χ using formula 4.2. The results are presented in Figure 4.8.

As in the control measurement, conducted for polystyrene–toluene system, χ changes with polymer volume fraction d_0/d: χ is decreasing with d_0/d for chloroform and it is increasing for other solvents (chlorobenzene, toluene and o-dichlorobenzene). It is worth highlighting that in the original Flory-Huggins theory the interaction parameter is independent of the polymer volume fraction which is usually true for nonpolar system. However, as experiments showed it is not satisfied for systems where either solvent of the polymer has a dipol [79]. Additionally, the increase in χ with polymer concentration is obtained for poor solvents and the decrease in χ occurs for
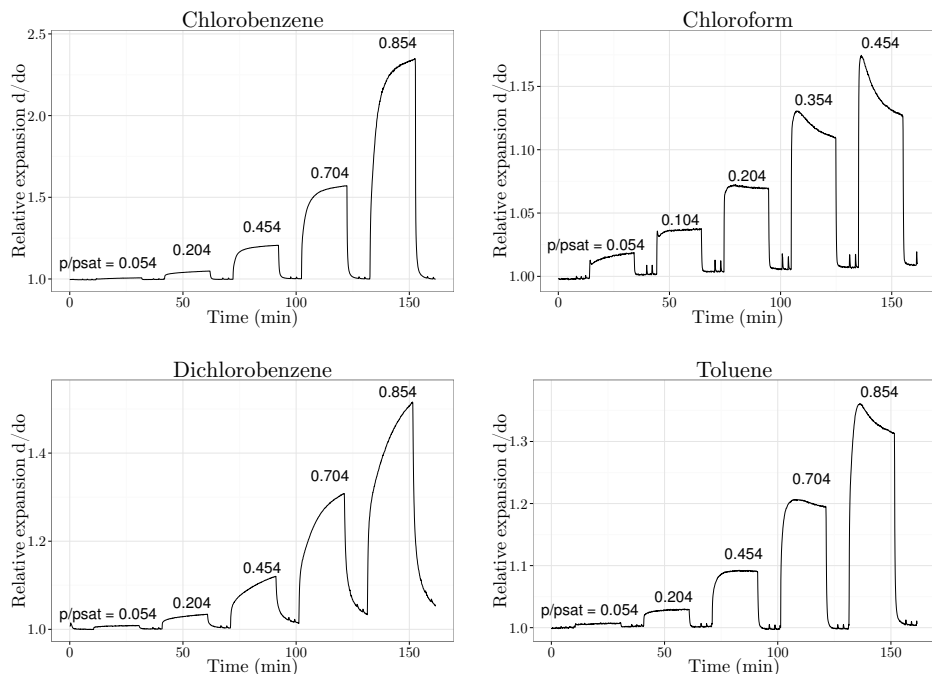
Figure 4.6: Relative expansion of PCDTBT films exposed to the sequence of various solvent vapors: chlorobenzene, chloroform, dichlorobenzene, toluene with different relative partial pressure.
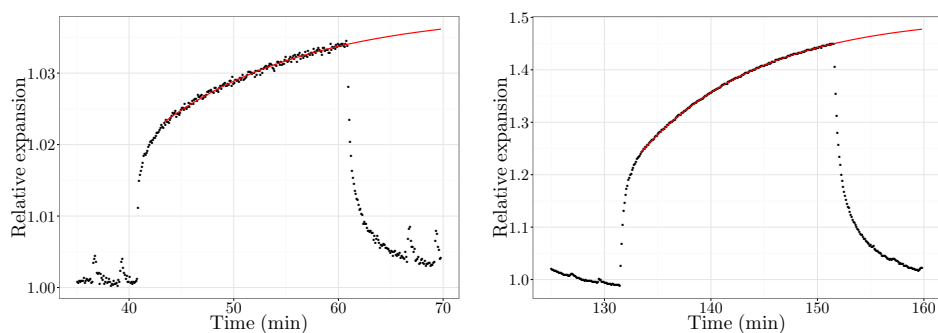

Figure 4.7: Example of fit an exponential model (Eq. 4.1) to data representing the expansion of PCDTBT films exposed to the dichlorobenzene solvent vapors with $p/p_{sat} = 0.204$ and 0.854

highly exothermic systems like PS/toluene [81]. However, the formula 2.20, we used to calculate χ applies also in the case of a variable χ, as pointed by Flory [79] himself.

If we now concentrate on χ values we see that they are in a range from -0.1 to 1.1. The positive value indicates that polymer–polymer and solvent–solvent contacts are more favored then the polymer solvent whereas a negative values inform about the preference of polymer–solvent neighborhoods [80]. As is visible in Figure 4.8 in almost all cases a neighborhood of the same species is preferred. Additionally, according to Flory-Huggins criterion, the complete miscibility can occur if $\chi_c < \frac{1}{2}(1 + \frac{1}{\sqrt{N}})^2$ where N is the degree of polymerization. Critical interaction parameter χ_c also tells us whether the solvent can be treated as a good one or a poor one. For PCDTBT, for which N is around 440 (see Section 4.2.1), χ_c amounts to approximately 0.54. Based on the presented swelling experiment we report chlorobenzene and chloroform as good solvents, toluene as a poor solvent for PCDTBT and o-dichlorobenzene in between.

For organic solar cells a selection of a proper solvent is one of the key factors which influence OPV final performance. However, as studies showed, choosing the best solvent for PCDTBT does not necessarily imply the best OPV performance, which according to studies was obtained for o-dichlorobenzene [138]. The reason behind this is that the final morphology of bulk-heterojunction is a result of complex behavior in the three component polymer—fullerene—solvent system which depends on many other parameters. Some of them will be discussed in Section 4.2. Even if χ cannot directly explain the formation of bulk-heterojunction it is nevertheless one of the necessary parameters to predict the phase behavior in polymer—fullerene—solvent mixture as we will demonstrate later.

4.1.4 Solubility parameter

The next parameter, which has an impact on the final morphology of the donor-acceptor mixture, is a solubility parameter δ which was originally developed to predict the mixing of simple non-polar solvents but later was extended to polar solvent and polymers [81]. This parameter can be understood as an internal pressure and, according to Hildebrand [139], it can be calculated as the square root of the cohensive energy density: $\delta = \sqrt{\frac{\Delta E}{V}}$ where ΔE is the vaporization energy of molecules, V their molar volume and δ is called the Hildebrand parameter. However, such definition is not accurate for materials in which dipole-dipole interaction or hydrogen bonding play a role. Therefore Hanses [140] proposed to split δ into three components; dispersive δ_d, polar δ_p and hydrogen δ_h; the geometric average of these components defines the parameter δ as $\delta^2 = \delta_d^2 + \delta_p^2 + \delta_h^2$.

There are several possibilities how to determine δ. The most direct way is to measure the energy of vaporization. However, this is possible only for volatile materials like solvents. In case of polymers indirect methods have to be used like solvent testing, measuring the osmotic pressure, swelling, surface tension or inverse phase gas chromatography (for more details see [81]). Additionally, there are also some different computational tools [141], based for instance on a group contribution technique,
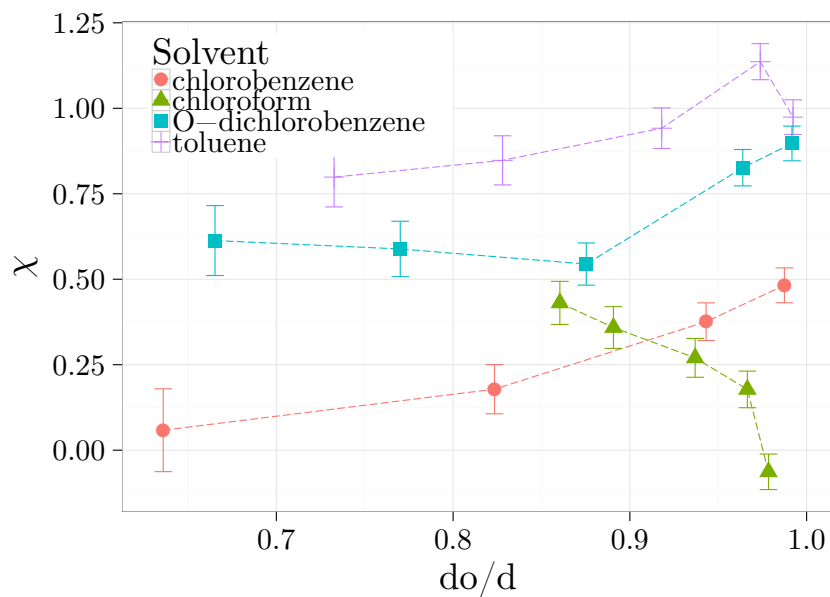
Figure 4.8: Flory-Huggins interaction parameter χ between polymer PCDTBT and solvents for different polymer volume fraction ϕ_P expressed by reverse of relative film expansion $\phi_P = \frac{d_0}{d}$.

which assume that the total energy of vaporization of polymer is a the sum of the energy of vaporization of different functional group.

Although solubility parameters for most of organic solvents are available in the literature [81], there is still little information about the solubility parameters of conjugated polymers. Doung et al. [142] obtained the Hansen Solubility Parameters (HSP) for small molecules, like $PC_{60}BM$ or $PC_{70}BM$, and semiconducting polymers P3HT and MEHPPV by measuring their solubility in 27 solvents and then using the HSPiP software developed by Abbot and Hansen. In the same way Machui et al. [143] predicted the HSP for P3HT, PCPDTBT and PCBM in a wide temperature range. Nilsson el. [123] estimated δ for APF3O–3, F8BT from experimentally measured surface energies, whereas Jaczewska et al. [124] used the swelling of polymer layer to determine δ for poly(3–alkylthiophenes).

In case of PCDTBT, to our knowledge, there are only two reported values of solubility parameter δ mainly 21.51 $MPa^{1/2}$ [128] and 23.8 $MPa^{1/2}$ [129], both determined by the group contribution technique. Here we estimated the solubility parameter δ for PCDTBT based on the experimental swelling data and using the relation between Hildebrand and Flory-Huggins interaction parameter. The solvents solubility parameter and molar volume were taken from [81] and resulted in δ(chloroform) = 19.0 $MPa^{1/2}$, δ(chlorobenzene) = 19.4 $MPa^{1/2}$, δ(dichlorobenzene) = 20.5 $MPa^{1/2}$, δ(toluene) = 18.2 $MPa^{1/2}$. As it can be seen in Figure 4.9 most of our calculated values fall within the reported range with the mean value δ(PCDTBT)= 22.8$\pm$ 1.2 $MPa^{1/2}$.
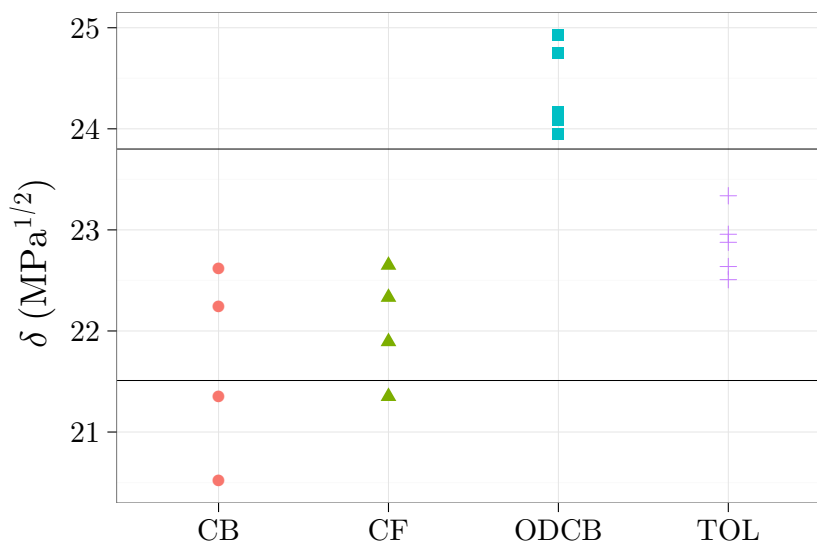
Figure 4.9: Calculated solubility parameters for PCDTBT based on the measured Flory-Huggins interaction parameter between polymer and different solvents: chlorobenzene (CB), chloroform (CF), o–dichlorobenzene (ODCB) and toluene (TOL). As a reference two reported δ values for PCDTBT 21.51 MPa$^{1/2}$ [128] and 23.8 MPa$^{1/2}$ [129] are marked.

Remarkably, the best efficiency of organic solar cells based on heterojunction PCDTBT:PC$_{70}$BM was recorded when this mixture was dissolved in oDCB [109].

Additionally, in the OPV context, it is worth noting that obtained δ(PCDTBT) is close to δ(PC$_{70}$BM) which is reported within the range of 20.7 MPa$^{1/2}$ [129] to 22.6MPa$^{1/2}$ [144]. Based on the equation 2.14, which links χ_{ij} with δ_i and δ_j, one can say that the smaller the difference between the δ_i with δ_j, the better they mix. However, as studies showed, χ predicts the miscibility only for amorphous substances [22] and it looses its importance when crystallization occurs.

4.2 Phase separation in ternary system

So far we have concentrated on the interaction parameter χ between conjugated polymer PCDTBT and four different solvents. However, as an active layer in an organic solar cell is commonly prepared from ternary systems – donor and acceptor materials initially dissolved in a common solvent – the knowledge of the χ alone is not sufficient to fully describe their mixing behavior. One possibility how to get insight is to construct a ternary phase diagram. This approach, in the context of conjugated polymers and small molecules, has been already presented by several groups [20, 120, 123]. The authors showed that a ternary phase diagram in combination with either the

film depth profiling or morphology analysis can reconstruct structure formation during a solvent evaporation. Here, inspired by the positive results from [20, 120, 123], we conducted a similar analysis as in [123] for mixtures of conjugated polymer PCDTBT, fullerene derivative $PC_{70}BM$ and various solvents. We were interested in whether a ternary phase diagrams can help us to understand the final $PCDTBT:PC_{70}BM$ morphology. Despite the growing popularity of PCDTBT in the context of organic photovoltaics [2], to our knowledge, it is the first time when this specific mixture was analyzed via ternary phase diagram.

4.2.1   The ternary phase diagram

A phase behavior of a three-component mixture can be graphically depicted using two-dimensional triangle plot, inside which each point corresponds to different component proportions. In our case the proportions will be expressed as volume fractions of solvent ϕ_1, polymer ϕ_2, and fullerene ϕ_3. In the equivalent triangle a sum of such proportions is always constant (here $\phi_1 + \phi_2 + \phi_3 = 1$). The ternary phase diagram is calculated from Flory-Huggins theory [79]. To construct the diagram we start with defining a Gibbs free energy G_m for a ternary blend:

$$\frac{G_m}{nk_BT} = \frac{\phi_1}{N_1}\ln\phi_1 + \frac{\phi_2}{N_2}\ln\phi_2 + \frac{\phi_3}{N_3}\ln\phi_3 + \chi_{12}\phi_1\phi_2 + \chi_{13}\phi_1\phi_3 + \chi_{23}\phi_2\phi_3 \qquad (4.3)$$

where ϕ_i is the volume fraction of components (in presented system $i = 1$ solvent, $2 =$ polymer (PCDTBT), $3 =$ fullerene ($PC_{70}BM$)), N_i expresses the degree of polymerization and χ_{ij} is the interaction parameter between components. Table 4.1 summarizes χ_{ij} and N_i values for the investigated mixtures. Additionally, in the Calculation details (at the end of Section 4.2.1) one can find a description of how we obtained these values. Using 4.3 one can calculate the most important features like spinodal and binodal curves or critical points. Spinodal and binodal lines separate composition space into three regions: a stable single phase region (outside the binodal); an unstable region inside the spinodal line, where the demixing occurs; and a metastable region located between both curves. In the metastable region the system is stable with respect to small composition fluctuation. The critical point is a point in which a spinodal and a binodal coincide and tie lines (red dotted lines in Figure 4.10) connect the points in binodal curve with equal chemical potential; their slope, which is driven by the difference in χ_{12} and χ_{13}, informs about the preference of solvent to be in the fullerene or polymer reach phase [20].

Figure 4.10 presents phase diagrams for $PCDTBT:PC_{70}BM$:solvent mixtures generated by dr Paweł Biernat based on the parameters from Table 4.1. The bottom left corner describes a highly diluted region, dominated by a solvent, similarly the bottom right corner and the top corner describe regions dominated with PCDTBT and $PC_{70}BM$ respectively. Let us look how we can describe a $PCDTBT:PC_{70}BM$ film formation through a ternary phase diagram. The starting point is a low-concentration
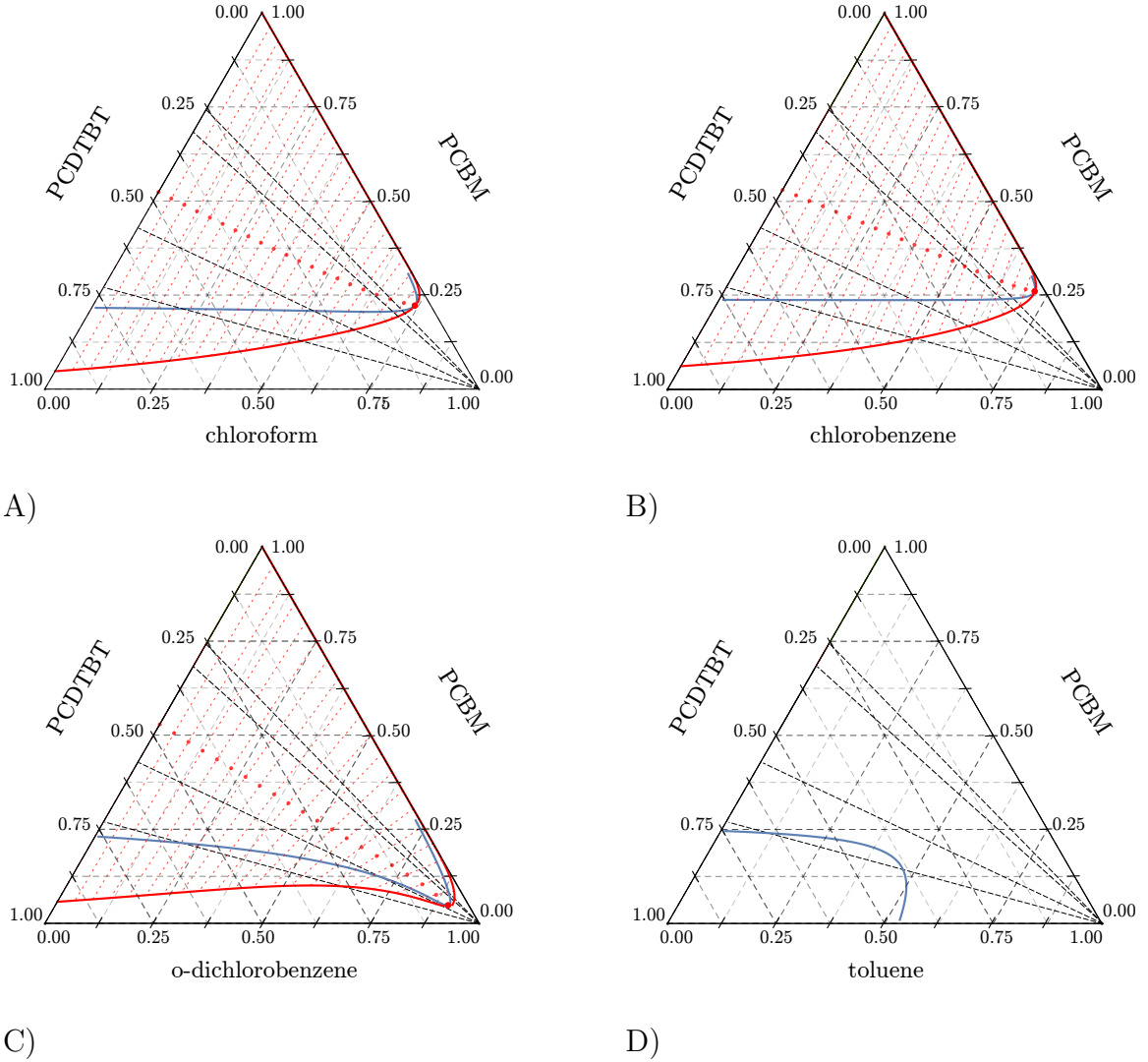
A)

B)

C)

D)

Figure 4.10: Ternary phase diagram of three component the system solvent:PCDTBT:PC$_{70}$BM calculated based on the parameter presented in Table 4.1. On the axis the volume fractions of three components (ϕ_1, ϕ_2 and ϕ_3) are marked. The red lines represent the binodal blue lines spinodal composition. Additionally, starting for the right corner, a direction of the solvent quench for a 2:1, 1:1, 1:3 and 1:4 PCDTBT:PC$_{70}$BM ratio is marked. The simulation was performed by dr Paweł Biernat.

solvent	χ_{12}	χ_{13}	χ_{23}
chloroform	0.431	0.610	0.387
chlorobenzene	0.178	0.631	0.350
dichlorobenzene	0.544	0.430	0.363
toluene	0.942	0.929	0.340

Table 4.1: Flory-Huggins interaction parameter χ_{ij} for ternary blend solvent (1): PCDTBT (2): PC$_{70}$BM (3). In each case an effective degree of polymerization amounts $N_1 = 1$, $N_2 = 440$, $N_3 = 6$.

region (points close to the right corner). As it can be seen in Figure 4.10 for chloroform (CF), chlorobenzene (CB), o-dichlorobenzene (oDCB) the blend starts in a stable single-phase region. When the solvent evaporates the whole system moves towards the higher concentration region along a straight line until it reaches the binodal curve. From this moment the mixture is no longer homogeneous and demixing occurs via spinodal decomposition or nucleation-and-growth, depending on the location of the intersection point.

Let us firstly concentrate on the results for chloroform and chlorobenzene presented in Figure 4.10A and B. Their phase diagrams are very similar, differing only slightly in a critical point position, which in both cases lies far from the centre of the diagram. Both binodal and spinodal curves are asymmetric which is a result of the molecular size difference between PC$_{70}$BM and PCDTBT. The binodal composition is visible only for the region enriched in PCDTBT with low fraction of PC$_{70}$BM. One phase region is here larger then for oDCB. If we look on χ_{ij} we can see that for both CB and CF the interaction parameter between solvent and polymer χ_{12} is relatively low (0.431 for CF and 0.178 for CB) denoting that both solvents can be treated as good one for PCDTBT. The dashed lines starting from the right corner indicate the direction of solvent quench for a (from bottom to top) 2:1, 1:1, 1:3, 1:4 blend ratio of PCDTBT:PC$_{70}$BM. Here for both CB and CF the system crosses the spinodal for lower solute concentration with increasing PC$_{70}$BM fraction. In other words for the ratio 1:4 the least amount of solvent has to evaporate before the composition reaches two-phase boundary and so it enters the two-phase region fastest. As Nilsson et al. [123] observed the less time the solvent needs to evaporate to reach the phase boundary the more likely the lateral structure will be formed.

In case of o-dichlorobenzene (Figure 4.10C) we observed an atypical shape of both curves, a critical point is shifted towards the more dilute region and the single phase region is comparatively smaller. Here less solvent has to evaporate to cross the binodal curve. This can have impact of the resulting morphology structures [123]. In case of toluene (Figure 4.10D) we did not observe a one–phase region which can be a consequence of a large discrepancy in χ_{ij} values because toluene is a poor solvent for PCDTBT and PC$_{70}$BM. As we mentioned, to our knowledge, there are no reported phase diagram for this specific blend PCDTBT:PC$_{70}$BM:solvent. However,

we found that our results for chloroform are similar to these presented by Michels and Moons [120], where they examined ternary system of polyfluorene copolymer APFO-3:PCBM:chloroform. The similarity is expected because APFO-3 has a similar chemical structure to PCDTBT.

Is it possible to predict the final morphology based on the ternary phase diagram? As Michels and Moons [120] pointed out, the position of the critical point can tell us what kind of final morphology, lamellar or drop-like lateral, we can expect. They described two systems; chloroform:APFO-3:PCBM and chloroform:PFB:PCBM. In case of APFO-3:PCBM the critical point was located in a relatively high solids concentration region and demixing occurs when the sum of volume fractions for APFO-3 and PCBM exceeds 0.37. In this example the lamellar structures were kinetically frozen, preventing the transition to the drop–like lateral structures. For such system the lamellar structures were expected with low surface roughness, which was confirmed by AFM measurement. Additionally, as authors of [120] suggest, in this case the phase separation is driven by diffusion process. For chloroform:PFB:PCBM the critical point is located in a region with high solvent fraction. In such region the mobility of the components allows to break up the lamellar structures before vitrification can take place, resulting in a drop–like lateral structures.

Going back to the phase diagrams for PCDTBT:$PC_{70}BM$ (Figure 4.10) we see that the lowest position of the critical point was obtained for chloroform and chlorobenzene. In those cases we expect the lateral structures with low surface roughness. In case of toluene we did not observe any critical point: the system is already in the unstable region. Here the possible break-up from lamellar to lateral profiles can take place. For o-dichlorobenzene the critical point is placed in a high solvent concentration region, similar as for chloroform:F8:PCBM examined by Nilsson et.al [123]. Here also drop-like structures can be anticipate. In the next section, based on the morphology analysis, we will see whether the foregoing predictions correspond with the results obtain experimentally.

Calculation details

To model the ternary phase diagram following parameters are necessary: three interaction parameters between solvent (1), PCDTBT(2) and $PC_{70}BM$ (3) χ_{12}, χ_{13}, χ_{23} and their effective degree of polymerization N_1, N_2, N_3. To calculate N_i we made similar assumption as in [123]. The single aromatic ring of the solvent is treated as the unit size resulting $N_1 = 1$. To determine N_2 we firstly divided the PCDTBT molecular weight (61 600 g/mol) by weight of monomer (701 g/mol) which gives us information about number of repeating units in the chain. Then considering a single aromatic ring as a unit we approximated the degree of polymerization as $N_2 = 440$. In case of $PC_{70}BM$ the molar volume approximate 600 cm^3/mol is 6 time bigger than the volume of solvent molecules therefore $N_3 = 6$. The values of interactions parameter between the polymer PCDTBT and solvents χ_{12} were obtained from the swelling experiment (see Section 4.1.3). As was shown in Figure 4.8, the interaction parame-

ters weren't constant but changed with concentration. For the following analysis we firstly concentrated on the χ values obtained for low relative partial pressure p/p_{sat} = 0.454. Two remaining χ_{ij} parameters between solvent and fullerene $PC_{70}BM$ χ_{13} and between polymer PCDTB and fullerene χ_{23} were calculated from eq. 2.25, similar as in [123]. All values necessary to construct a phase diagram are presented in Table 4.1.

4.2.2   Morphology of PCDTBT:PC$_{70}$BM

The choice of solvent not only affects the phase behavior in blend systems, as was presented in Figure 4.10, but also has an impact on the final morphology of the polymer:fullerene film, which plays an important role in organic photovoltaics performance (for comprehensive review see [14,19]). In the context of PCDTBT and $PC_{70}BM$ there are already several studies [109,145] in which authors examined the influence of three solvents; chloroform (CF), chlorobenzene (CB) and dichlorobenzene (DCB) on the film morphology and OPV performance. The purpose of this part was not only to extend the research to another solvent – toluene (TOL) – but also check whether our prediction about final morphology, based on the ternary phase diagrams presented in the previous section, are correct or not.

Experimental

Sample preparation and morphology analysis   Blend of PCDTBT:PC_{70}BM in varied weight ratios (2:1, 1:1, 1:3, 1:4) were dissolved in four different solvents: chloroform (CF), chlorobenzene (CB), o-dichlorobenzene (ODCB) and toluene (TOL). The solute concentration was set to 5 mg/ml for CF, CB, ODCB. In case of TOL, due to a poor solubility of PCDTBT in TOL, we decreased the solute concentration to 2.5 mg/ml. We prepared thin layers on the previously cleaned silicon substrate by spin-coating (300 rpm for 2 s, 1500 rpm 90 s). The topography of the layers was examined by contact AFM mode and analyzed by Gwyddion software.

From lamellar to lateral structures: introduction

Before we move on to our morphology results for PCDTBT:PC_{70}BM film let us briefly describe what happens during evaporation induced phase separation in a thin layer. This topic was widely discussed by several groups [120–122,146,147], here we concentrated on their most important observation for polymer:fullerene blends. The starting point in thin film formation is a polymer:fullerene blend dissolved in a common solvent. This solution is usually one–phase system with low solute concentration. During the film formation by printing or spin–coating the solvent is evaporating, which increases the solute concentration and moves the system into a two–phase region (as depicted in a ternary phase diagram in Figure 4.10). In case of solvent quenching the whole separation process is so fast that decomposition is dominated via spinodal
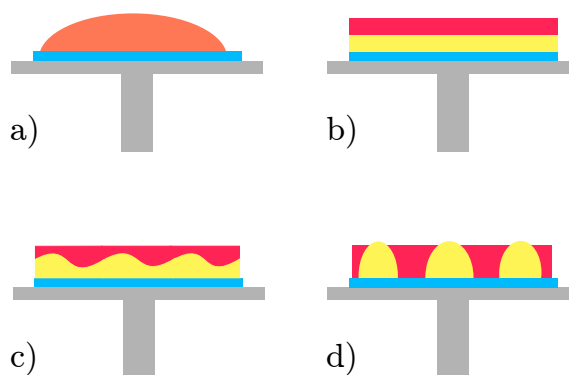
Figure 4.11: Schema of film formation during the spin coating. a) Initial stage of spin-coating b) vertical separation d) sinusoidal-like distortion of the interface resulting in d) lateral phase separation.

process instead of nucleation [122] resulting in structures of different topography from lateral to lamellar. As studies suggest [147], the whole process can be divided into several steps (Figure 4.11). Initially a vertical separation is induced resulting in the lamellar structures. This effect is related to the fact that blended components preferentially wet either the substrate or an air interface. Next, the lamellar structure can either freeze or break up into droplets due to instability caused by solvent concentration gradients within the film. Finally these droplets can merge into larger domains or even lateral structures [120]. Whether or not this transition from lamellar to drop–like or lateral structures takes place depends on the mobility of blend components in the solution, which is related to polymer concentration and evaporation rate. As experimental [123] and theoretical [121, 122] studies showed, by controlling the evaporation rate and blend composition one can cause the final morphology to be either lateral or lamellar. Below we discuss the morphology for PCDTBT:PC$_{70}$BM mixture prepared from different solvent.

Results

Figure 4.12 presents AFM topography of PCDTBT:PC$_{70}$BM films prepared from four different solvents with four different polymer:fullerene mixing ratios each. As we can see, both variables affect the final morphology. By varying a solvent we observe wide rage of feature: distinct islands for toluene, lateral structures for chloroform, nanoscale separation for chlorobenzene, homogeneous layer for o-dichlorobenzene, chlorobenzene and toluene.

Let us firstly concentrate on structures formed from toluene solution. For the mixing ratio PCDTBT:PC$_{70}$BM 2:1 the flat surface with no visible features is observed (roughness $\approx$0.44 nm). With increasing PC$_{70}$BM content, the islands with circle shape became more pronounced. For ratio 1:3 the islands are 66$\pm$ 2 nm high and 543$\pm$ 10 nm wide for 1:3 there are even higher and wider: 848$\pm$ 34 nm and 127$\pm$ 3 nm.
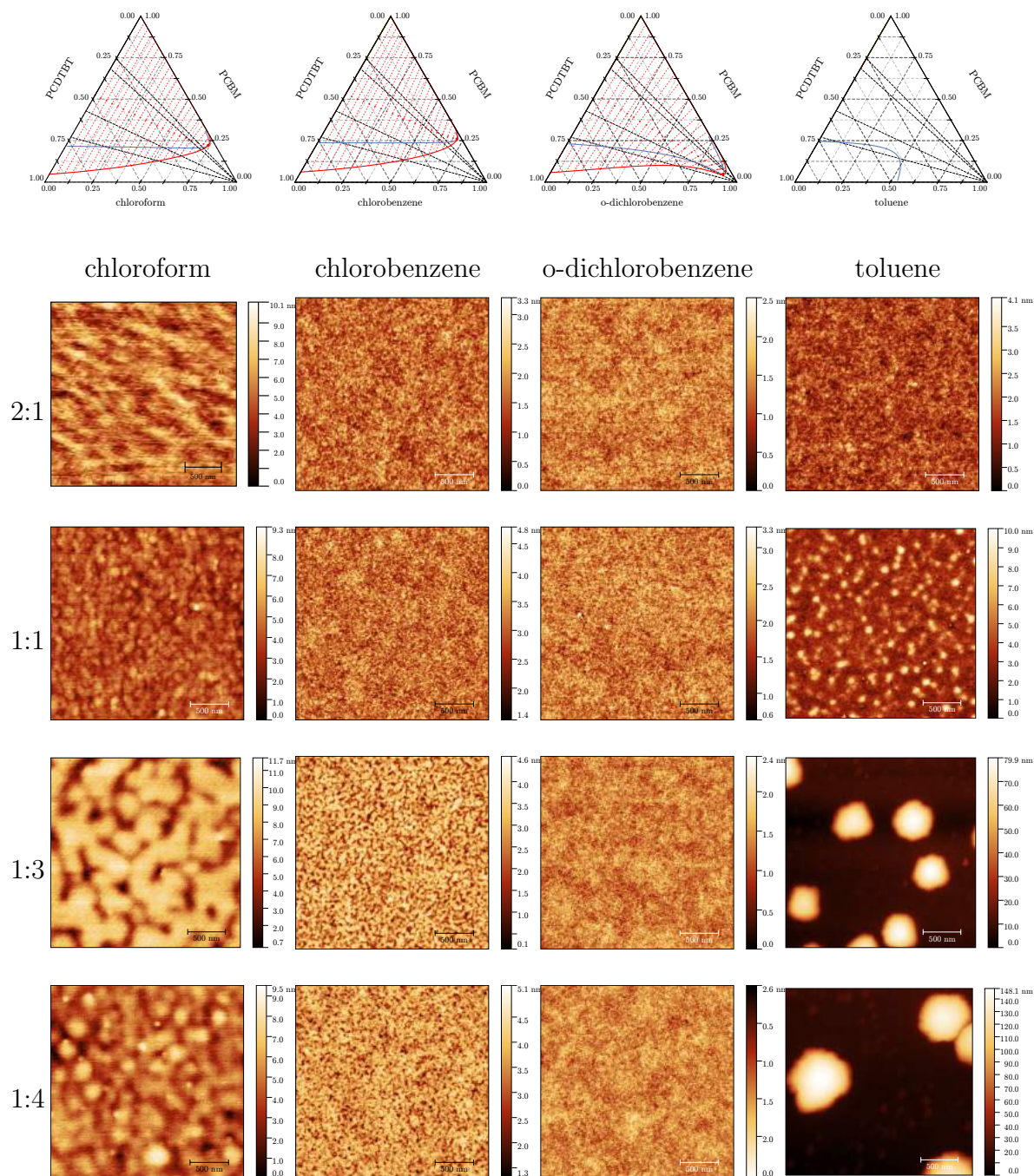
Figure 4.12: AFM images of polymer layers prepared from spin coated PCDTBT: PC$_{70}$BM blends with varying ratios and different solvent types.

The similar islands were observed by Hoppe et al. [148] for MDMO-PVV:PC$_{60}$BM film spin coated also from a toluene solution. Their size was one order of magnitude bigger than the size of the structures prepared with chlorobenzene solution. Here a question comes to mind. Which material, polymer or fullerene, are the clusters made of? Unfortunately, we cannot answer this question basing solely on AFM images. Here the additional experimental tools would be necessary like photoluminescence measurement [148] or a scanning transmission X-ray microscopy [149]. Indeed, with these methods authors showed that large cluster are assigned to the bare PCBM phase. Additionally, according to Nillson et al. [123], who examined the phase behavior in polyfluorene copolymers:PCBM mixture, the islands are a result of high solvent evaporation rate (chloroform, toluene or xylene) and strong polymer:fullerene repulsive interaction. Here our results partly support the first of Nillson's observations. For two high volatile solvents - toluene and chloroform we obtained cluster structures only for some mixing ratio. Additionally, in our experiment the interaction between PCDTBT and PC$_{70}$BM was relatively low (see χ in Table 4.1) and did not vary within mixtures, nevertheless both cluster and flat layer, were formed. Here we favor the explanation presented by Michels and Moons [120]. They demonstrated that for systems with a critical point located in the high solvent fraction region the transition between lamellar and lateral structures can take place. In case of toluene:PCDTBT:PC$_{70}$BM we did not observe the critical point which means that from the beginning the system is located within an unstable region. For low polymer concentrations the mobility of the blend components is sufficiently high to allow to drop-like breakup.

We obtained the interesting results for chloroform and chlorobenzene. The ternary phase diagrams, for these two solvents, are almost identical, so based only on diagram analysis the final morphology of polymer:fullerene layer should be similar. However, as AFM pictures depict, there are visible discrepancies in nanophase separation. Consequently, these results show that the ternary phase diagram is not sufficient to predict the final morphology. As resent studies showed [120, 122] the crucial thing is the dynamics of the process, which unfortunately cannot be seen in phase diagram. This dynamics is related to the solvent evaporation rate: the faster the evaporation, the more pronounced lateral structures are [123] which was also visible in this experiment.

At the end, the smooth final surfaces, with roughness not exceeding 0.6 nm, were obtained for o-dichlorobenzene. The summary of the roughness measurement for all solvents is presented in Figure 4.13. Our results are compatible with the values presented by Shin et al. [145], who compare the roughness for PCDTBT:PC$_{70}$BM prepared with chloroform, chlorobenzene and o-dichlorobenzene. They also observed an increase in roughness in following order, from o-DCB, CF to CB.

Morphology and OPV performance

As we showed, the solvent significantly affects the final morphology of the polymer:fullerene layer. The question now is which film morphology to choose as an active layer in organic solar cells. In this section we will summarize and apply the extensive
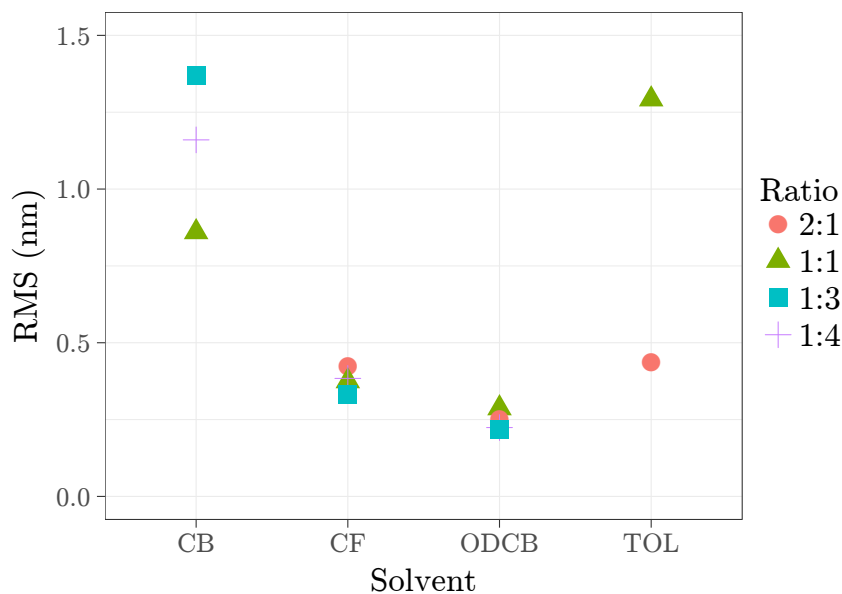
Figure 4.13: Surface roughness of PCDTBT:PC$_{70}$BM layers obtained from AFM images (Figure 4.12). The layers were prepared from solution by spin coating. We varied component mixing ratios (2:1, 1:1, 1:3, 1:4) and solvent (chlorobenzene (CB), chloroform (CF), o-dichlorobenzene (ODCB), toluene (TOL))

existing results on influence of solvent on the performance of OPV [109, 145, 148] to our particular solvents.

Park et al. [109] examined the effect of solvents – chloroform (CF), chlorobenzene (CB) and dichlorobenzene (DCB) – on the film morphology and device performance based on the bulk heterojunction PCDTBT:PC$_{70}$BM (1:4 ratio). Based on the J–V characteristics they demonstrated that the best performance was achieved for the devices fabricated with active layer coated from DCB. For this solvent they obtained a well defined nanoscale phase separation, whereas use of CF and CB result in the large 300 nm cluster. For such large structures the mismatch between exciton diffusion length (less then 10 nm) and the cluster size will result in recombination losses and therefore in a decrease in photocurrent and a reduction of efficiency.

The similar research was conducted by Shin et al. [145] in which authors examined the influence of three solvent CB, CF and o-DCB and four blend ratios of PCDTBT:PC$_{70}$BM on the OPV performance. Based on AFM images they showed that PCDTBT:PC$_{70}$BM films coated from CF and CB posses the granular domain with a size of hundreds of nanometer. This size of the granules increases with increasing ratio of PC$_{70}$BM in the mixture. For o-DCB they observed no PC$_{70}$BM aggregation only fiber-like nanostructures which according to authors indicates good miscibility between PCDTBT and PC$_{70}$BM. Similarly to [109], they obtained the best performance for OPV with active layers casted from o-DCB with PCDTBT:PC$_{70}$BM

in ratio 1:4.

To conclude the best performance was achieved for clearly defined fibrillar nanoscale phase–separated structures. Therefore the layer prepared from toluene, as we see in Figure 4.12, is not good candidate for the active layer in OPV.

4.2.3 Conclusion

We constructed ternary phase diagrams from the interaction parameters between components to describe the possible phase behavior in the polymer:fullerene mixture.

However, the morphology analysis of the final structures can not be inferred solely from ternary phase diagrams and other factors have to be taken into account such as dynamics of the solvent evaporation. This is necessary because phase separation is a dynamic process, while the phase diagrams only describe the stationary states of the system. To predict the morphology of the film formation one has to refer to more advanced techniques such as numerical simulations [122] or advanced experimental methods like in situ grazing incident X-ray diffraction [21].

Chapter 5

Light trapping layer in organic solar cells

Organic photovoltaics (OPV) are candidates for low cost solar cells; however, the efficiency of these cells is still lower than that of their inorganic counterparts. There are several factors determining the overall performance of photovoltaic devices to point the two most important: light absorption and charge collection. One way to enhance the absorption is to increase the thickness of the active layer. However, increasing the thickness of the active layer decreases the charge collection in OPV. Another way to improve the absorption is to add light trapping structures without increasing the actual thickness of the layer. This strategy is commonly used in the field of silicon photovoltaics [61, 150–152] but for organic solar cells it is still in an early development stage [44].

Inorganic light trapping layers (or anti-reflection coatings) used in silicon solar cells are fabricated by vapor deposition, etching or photolithography. The advantages of all of these methods are wear-resistance, size-control and high-precision but their production is complicated and expensive. On the other hand, organic light trapping layers can be manufactured by simple and cost effective methods such as solution casting or printing. By applying these methods it is possible to obtain a wide range of self-organized structures. Despite the advantages of self-organization, in the context of light trapping layers, there is no conclusive evidence on the influence of such structures on OPV performance. Instead, most studies have focused on the optical properties of these structures such as reflection or transmission [49, 50, 54].

Non self-organized structures prepared by soft lithography or chemical etching were recently investigated by several groups [64, 65, 153] . In [154] Cho et al. examined the organic textured films attached to the front side of OPV. The authors used the front side to avoid interfering with the insides of OPV, which simplified the process of adding the light-trapping layer. On the other hand, the techniques they used were

limited to a narrow set of commercially available masters.

The goal of this part of the doctorate project was to explore the effects of self-organized structures as external light trapping layers on OPV performance (Figure 5.1A). We compare periodic and porous structures prepared using soft lithography (Section 5.1) and breath figure formation (Section 5.2), respectively. Additionally, in Section 5.1.1, we tested the soft lithography technique as a method to prepare the imprinted active layer (Figure 5.1B).
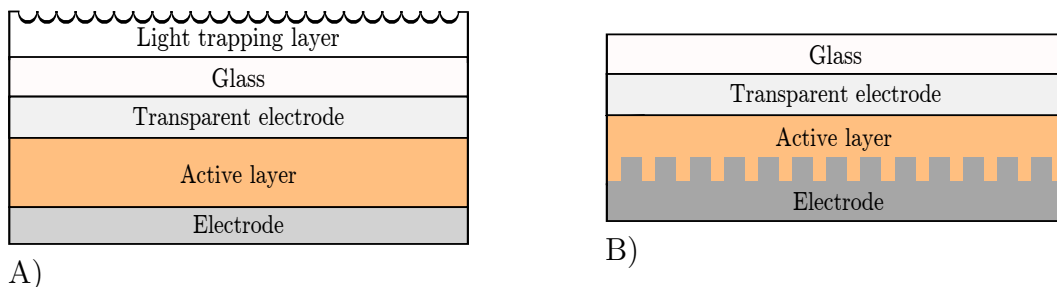

A)

B)

Figure 5.1: Schematic organic solar cell with A) external light trapping layer, B) imprinted active layer
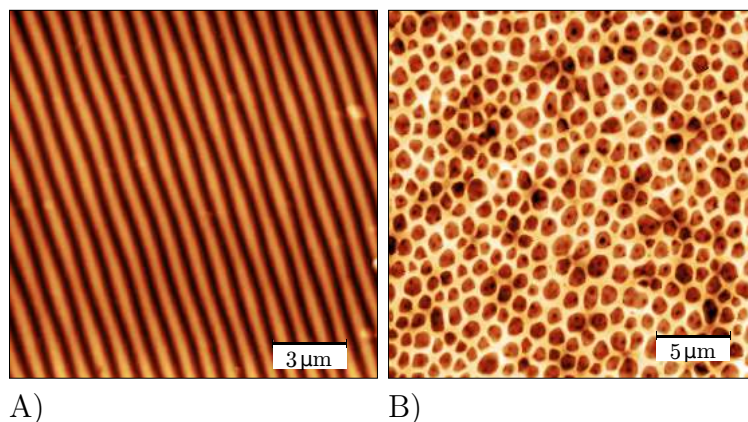

A)   B)

Figure 5.2: Examples of light trapping layer: A) Periodic structures with period $\sim$ 800 nm corresponding with DVD period. We used DVD as a master for PDMS stamp, a crucial element in soft lithography. B) Porous structures were obtained by deposition of a polymer solution either in a humid atmosphere or by adding the water into the solution.

5.1 Periodic structures

5.1.1 Imprinting active layer in blend solar cells

Introduction

In the last decade the imprinted organic solar cells have attracted an attention of researchers (see [59] for a comprehensive review). One of the first example of using the soft–lithography was presented by Roman et al. [68]. They reported the improvements in External Quantum Efficiency (EQE) after patterning the active layer with 416 nm period. Na et al. [64] investigated the influence of various periodic sub–micrometer structures formed on an active layer on solar cells performance. They showed that the overall device efficiency increased thanks to the improvement of photon absorption in the active layer. Park et al. [69] applied solvent–assisted soft stamp–based nanoimprinted lithography to prepare the periodic structures. They examined organic solar cells with the interpenetrated bilayer $P3HT/PC_{60}BM$ with four different period: 1600 nm, 810 nm, 420 nm, 360 nm. They showed the increase in power conversion efficiency, from 2.1% to 2.4%, compared to the flat reference layer. Kim et al. [155] used two molds with period 510 nm and 700 nm to imprint the structures in a polymer layer. They observed the increase in short current density as well as in efficiency for both structures compared to the control cell.

However, even if the authors use soft lithography methods the masters were fabricated by photolithography, for which expensive instruments are required. Inspired by the results presented in [64] and [156] we proposed to use commercially available CD, DVD and Blu–ray discs as templates for the PDMS stamps. Meanwhile, it appears that the idea of using commercial discs attracted much attention as reflected a recent paper by Smith et al. [157]. They showed that imprinting a quasi–random Blu–ray pattern on an active layer leads to higher absorption and efficiency of the organic solar cells.

Below we present the results of patterning the active layer with the structures coming from unrecorded discs with periods ∼1600 nm, 800 nm and 350 nm. Firstly, we reported the improvement in absorption after the patterning the absorbed layer. The biggest changes was observed for structures with period 800 nm. Based on this observation we prepared the solar cells with the imprinted active layer as is schematically presented in Figure 5.1B. We compared the performance of solar cells with the imprinted active layer to solar cells without the imprint and we observed an improvement in the short–circuit current, however the remaining parameters like fill factor, open current voltage or efficiency worsened.

Experimental

Elastomeric PDMS stamp preparation: As a master for the surface relief grating we used commercially available CD, DVD and Blu–ray discs composed of a polycarbonate substrate, reflective, recording and protective layer. The layers were firstly man-

ually separated and cut into smaller pieces, from which we prepared stamps using poly(dimethylsiloxane) PDMS (commercially known as Sylgard 184). The mixture of polymer base and a curing agent with a ration of 10:1 was placed into the ultrasonic cleaner for 15 min to remove trapped bubbles and then poured onto the previously prepared disc's polycarbonate layer and cured at 120°C for 25 minutes. After curing the stamp was peeled off from the polycarbonate substrate and was ready to use.

Sample preparation: For the optical measurement the samples were prepared on microscope slides, previously cleaned in acetone and dried with nitrogen. One side of each slide was cover by light absorbing thin layer prepared from poly(3-octylthiophene) P3OT dissolved in chloroform by spin-coating (1000 rpm, 30 s). After the absorption measurement we fabricated the periodic structures using Solvent-assisted micromolding (SAMIM) technique. A small amount of solvent was placed onto the stamps surface and then brought into the contact with polymer layers. After 10 s of gentle squeezing the image of the stamp was transferred into the polymer layer.

OPV fabrication: P3HT and $PC_{60}BM$ with a weight ratio of 1:0.8 was dissolved in chlorobenzene with total concentration 20 mg/ml and stirred on a hot plate at 50°C for 24 hours. Pre–patterned ITO (Ossila Limited) glass substrates were cleaned in acetone and isopropanol, dried with nitrogen and placed in a plasma cleaner for 20 s. PEDOT:PSS, previously filtered through a 0.2 μm filter, was spin-coated at 4000 rpm for 30 s and annealed on hot plate at 150°C for 5 min. Then the substrates were transferred into the glovebox were a drop of P3HT and $PC_{60}BM$ solution was placed on the PEDOT:PSS and spin–coated at 3000 rpm for 60 s. To imprint the pattern on the active layer the PDMS stamp was moisturized with chloroform and put in contact for 10 s. After removing the PDMS stamp an 80 nm aluminium layer was thermally evaporated on the top of active layer. After evaporation the devices were annealed at 150°C for 15 min. Finally, all devices were encapsulated by a glued top–glass in order to prevent the degradation of the OPV.

Characterization: The topography of the periodic structures was analyzed by atomic force microscopy AFM (Agilent 5500) working in contact mode. The images were preprocessed and analyzed using the Gwyddion software. The mean structures dimension were obtained based on the line profile and the Fourier transformations of the images. The absorption and reflection of samples were measured using system built in our laboratory [115] consisting of halogen lamp, computer-controlled monochromator (Cornerstone 260 1/4 m, Newport), two detectors (Amplified UV–Si Photodetector, Newport), lock–in amplifier (Stanford Research System). The current–voltage characteristics of fabricated organic solar cells were measured using the source meter under the solar simulator of 500 W/m^2 intensity in order to reduce degradation effect.

Choice of the method

In recent two decades soft lithography techniques found applications in disciplines in which the soft materials or elastic substrates are used, examples include organic–based microelectronics, medicine or biology. This increased interest sped up the development of new soft lithography techniques: replica molding, microcontact printing, micromolding in capillaries, solvent–assisted micromolding (see [100, 158, 159] for a comprehensive review). Despite the many advantages—like low cost, short time of pattern preparation, possibility of working with a broad range of materials—the soft lithography has also some limitations. The defects occur more often than in photolithography, the pattern in the stamp may be damaged due to swelling or shrinking and some techniques are limited only to small surfaces [100].

To determine which techniques are most suitable for our applications we performed a preliminary experiment where we compared Solvent-assisted micromolding (SAMIM) and Microtransfer molding (μTM). During SAMIM the elastomeric stamp is wetted with a solvent and next brought into contact with the polymer layer. In μTM the stamp is inked with the polymer solution and then the pattern is transferred to the substrate by direct contact.

Both techniques result in regular periodic structures but with differences in height profile and period (Figure 5.3). The height and period are also widely spread among the techniques which indicates poor reproducibility. Additionally, what is not visible in Figure 5.3, during the printing we encountered a problem. In the case of μTP pressing the stamp resulted in a pattern covering only small random areas. These might not be a problem in some experiments, where the position of the structures is is not crucial. However for application in organic solar cells it is necessary to print the pattern on the whole area of the active layer, to avoid short–circuits. The latter was the main cause for selecting the SAMIM as our method of choice, despite its deficiencies in reproducibility of period and height (cf. Figure 5.4). The exact experimental setup and results is described in the following paragraphs.

Solvent-assisted micromolding (SAMIM) vs. Microtransfer molding (μTM) The starting point in soft lithography is to prepare the stamps. It is made by casting the elastomeric polymer PDMS onto the master with appropriate pattern. Generally the masters with high quality pattern are fabricated by e-beam lithography or photolithography. However, these techniques are time–consuming and require specialized equipment. Inspired by Meenakshi et al. [160] we present here a different approach. As a master we use commercially available discs: CD, DVD and Blu–ray with corresponding period 1600 $\pm$100 nm, 740 $\pm$46 nm and 335 nm [161]. It turned out that in this way we are able to prepare the pattern on the top of elastomeric stamp with period of hundreds nanometers which is next reproduced by different soft lithography techniques. This approach is characterized by the advantage of simplicity and reproducibility of the master.
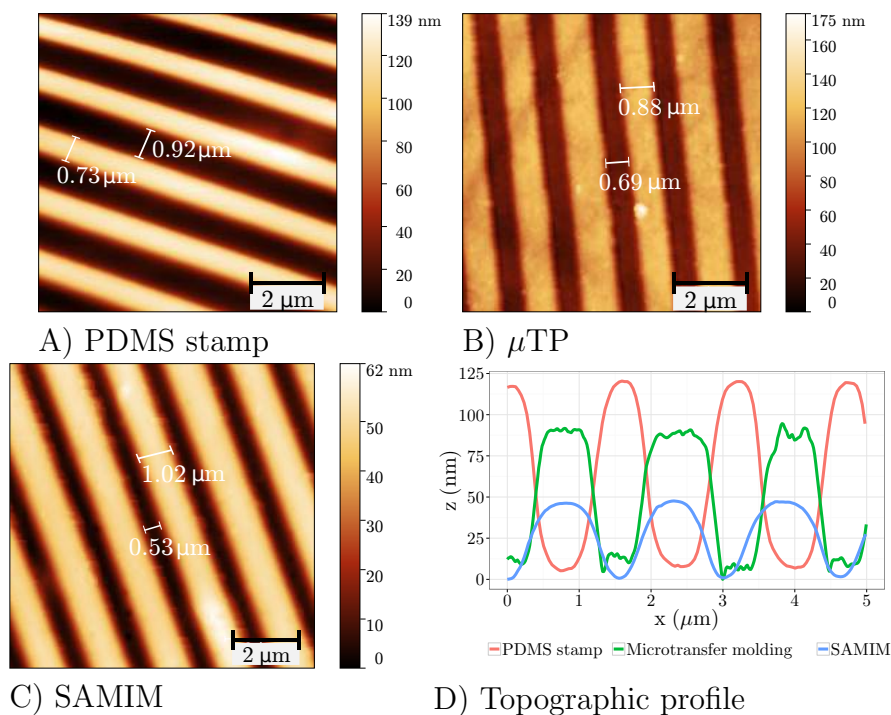
A) PDMS stamp

B) μTP

C) SAMIM

D) Topographic profile

Figure 5.3: AFM images of A) PDMS stamp prepared from CD disc and imprinted polymer absorbed layer poly(3–octylthiophene) obtained by two soft lithography techniques: B) Microtransfer molding (μTM) and C) Solvent-assisted micromolding (SAMIM) with the examples of the depth profiles D).

To test the geometry of pattern fabricated by Solvent–assisted micromolding (SAMIM) and Microtransfer molding (μTM) we concentrated only on structures made by elastomeric stamp with period corresponding to a CD disc prepared from poly(3–octylthiophene) solution. The typical CD's polycarbonate pattern dimensions are [101]: $\sim$ 1.2 μm width, $\sim$ 0.69 μm space between the line, $\sim$ 110 nm height. The elastomeric stamp prepared from CD has a negative pattern to CD disc. As it is shown in Figure 5.3A and D the patterns are almost sinusoidal with the line width 0.73 $\pm$0.07 μm being smaller that the space between them 0.92 $\pm$0.06 μm and height 118 $\pm$10 nm.

Using the μTP and SAMIM technique we prepared two sets of samples consisting at least 5 samples. Each sample was next characterized by AFM microscope. Examples of surface topography are shown in Figure 5.3B and C. In both cases we obtained the regular structures however differing in size. The structures prepared by μTP are higher and narrower compare to the pattern prepared by SAMIM, also the period is not equal. The difference is visible in Figure 5.4. The mean period of structures is equal to 1 570 $\pm$88 nm for μTP and 1650 $\pm$93 nm for SAMIM, the mean height amounts 87 $\pm$15 nm for μTP and 67 $\pm$14 nm for SAMIM. Moreover, the height spread

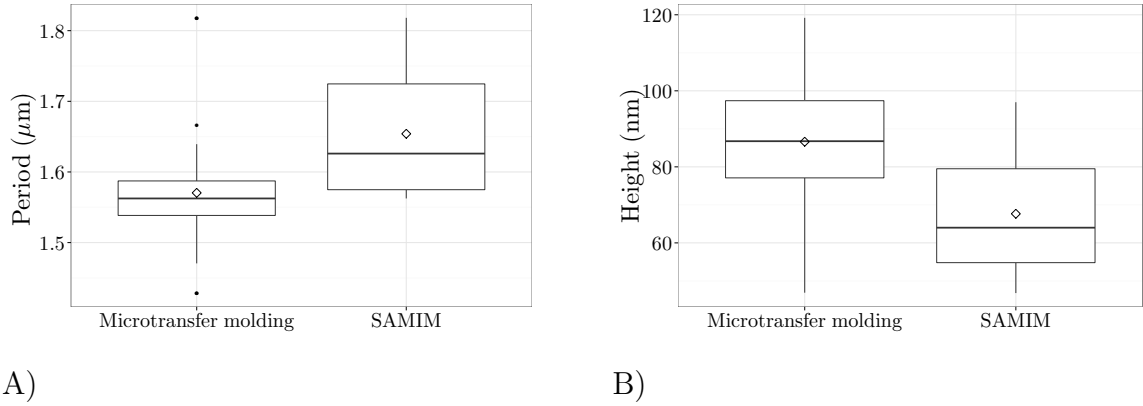A)   B)

Figure 5.4: Summarized A) period and B) height of all pattern prepared by Micro-transfer molding (μTM) and Solvent-assisted micromolding (SAMIM) with marked average value.

visible in the boxplot (Figure 5.4) indicates a relatively poor reproducibility of tested techniques (SAMIM and μTP).

It is worth to point out that similar difference in period and height between SAMIM and μTP we also observed for structures prepared using PDMS stamp with pattern corresponding to DVD disc. SAMIM techniques result in structures with larger period 813 ± 17 nm and lower height 51 ± 22 compare to these prepared by μTP for which period amount 763 ± 37 nm and height 109 ± 11 nm. The increase in period for SAMIM can be associated with swelling of PDMS stamps under the influence of solvent, in our case chloroform. As Lee et al. [103] showed chloroform, with solubility parameter $\delta =9.2$ (cal/cm)$^{1/2}$, has one of the highest swelling ability for PDMS ($\delta =7.3$ (cal/cm)$^{1/2}$) resulting in increase in length up to 39%. In our experiment we didn't observed such expansion probably due to much shorter exposition time (less then 1 min) of PDMS to the solvent compare to the 24 h presented in [103]. In case of μTP the PDMS stamp was inked with polymer dissolved in thiophene (with solubility parameter $\delta =9.8$ (cal/cm)$^{1/2}$). Unfortunately in [103] there are no results for this PDMS solvent combination. However, based on authors observation solvents with $\delta \sim 9.9$ (cal/cm)$^{1/2}$ characterize with moderate effect on PDMS with swelling about 10%. The changes in pattern size by swelling PDMS stamp was also observed by Xia and Whitesides [162]. In their work they also reported that the swelling process is reversible — the PDMS stamp return to the original size after solvent evaporation.

Optical properties of the imprinted pattern

After choosing the appropriate soft lithography technique, solvent–assisted micro-molding (SAMIM), we concentrated on the the main part of the experiment: the influence of patterning the absorbed polymer layer Poly(3–alkylthiophene) on the their optical properties. The experiment was conducted in following steps. To get the
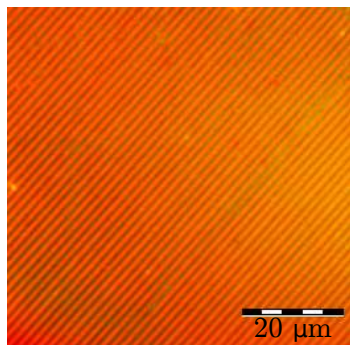
Figure 5.5: Optical images of long rages order of poly(3-octylthiophene) P3OT structures prepared by SAMIM taken at a 100x magnification

flat absorbed layer on one side of a glass substrate we spin coated polymer solution of poly(3–octylthiophene) P3OT. Then, we printed the periodic pattern on the polymer layer using a stamp covered by a small amount of solvent (as via SAMIM). Figure 5.5 shows that this methods allows to obtain regular structures over a large area.

Topographic measurements   Before optical measurement we examined the quality of the patterning by AFM microscopy. Figure 5.6A to C presents the resulting AFM images of periodic P3OT patterns imprinted by the PDMS stamps with period corresponding to the CD, DVD and Blu–ray disc. The highest quality layers, with long range order and almost sinusoidal shape, were achieved when using CD and DVD as a master. For the Blu–ray some discontinuities were visible: the pattern is ragged at the extrema. The periods of these structures were obtained by applying the Fourier transform to AFM images, the heights were calculated based on line profiles.

   The prepared structures characterized with three types of period: 1654 ±93 nm, 813 ±17 nm and 345 ±36 nm (Figure 5.6) and corresponding heights: 64 ±13 nm, 51 ±22 nm and 13 ±5 nm. The observed difference in the height are caused by various pit height for polycarbonate moulded discs used as the master: $\sim$ 140 nm (CD), $\sim$ 133 nm (DVD) [160] and $\sim$ 25 nm (Blu–ray) [161].

Optical measurement   To investigate the influence of periodic structures on the optical properties we measured light absorption and reflection. Each sample was measured twice: before and after imprinting the periodic structures, so the direct influence of the patterning could be determined. An example of the absorption spectra is presented in Figure 5.7A. The absorption was clearly enhanced for all of the imprinted layers over the whole spectrum. This result is consistent with other similar measurements reported by Smith et al. [157] who observed the increase in absorption after patterning an active layer with Blu–ray patterned mold.

   To quantitatively describe the changes in absorption we calculated the total absorptivity in the polymer layer as the $A_T = \frac{\int A(\lambda)S(\lambda)d\lambda}{\int S(\lambda)d\lambda}$ where A(λ) represents the
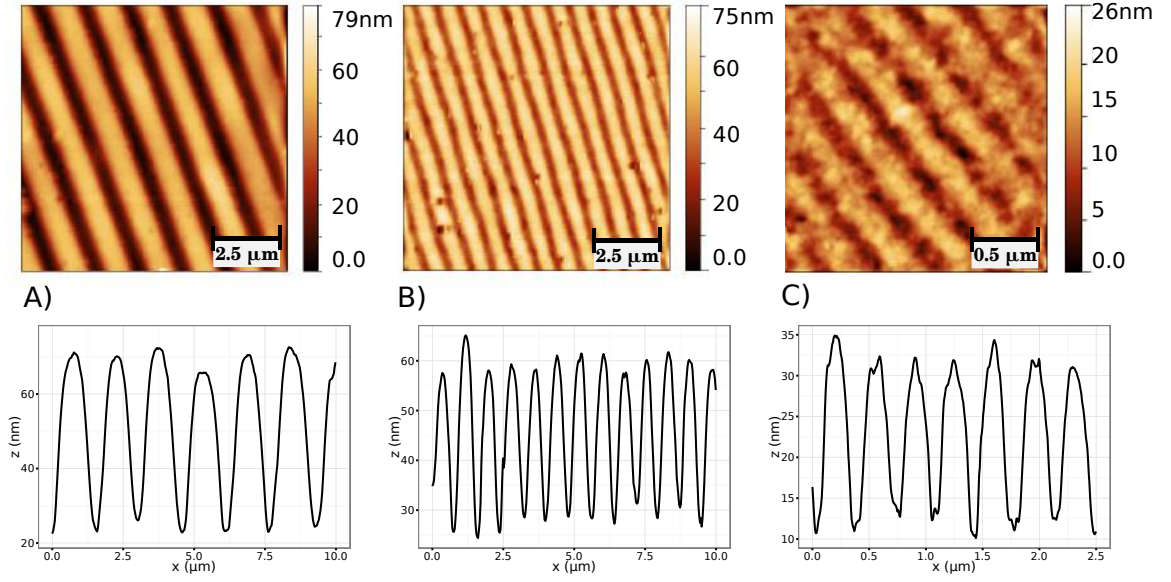
Figure 5.6: Topographic AFM images with corresponding cross-sections of the structured poly(3–octylthiophene) P3OT layer with different period fabricated by soft-lithography.
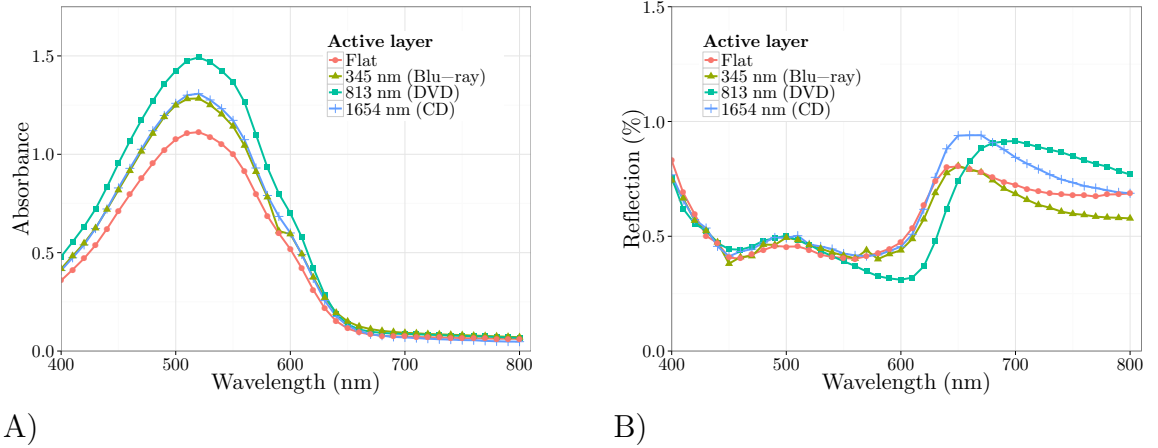

Figure 5.7: Comparison of A) absorbance and B) reflection spectra of flat and imprinted P3OT layer for periods correspond to Blu–ray, DVD and CD disc.
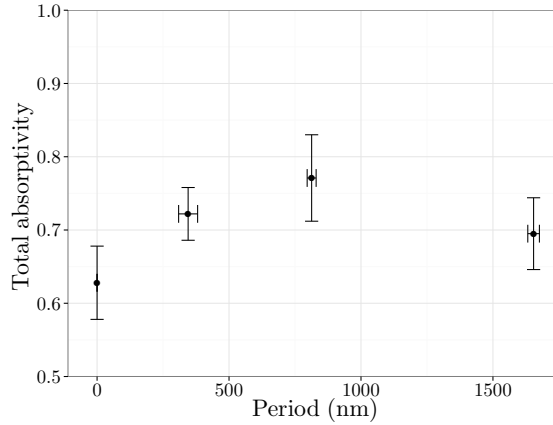
Figure 5.8: The mean values of total absorptivity in the P3OT layer with different periodic structures.

absorbance, S(λ) is Solar irradiance spectrum. As is seen in Figure 5.8 all three periods have positive influence on total absorptivity in P3OT layer. The highest improvement up to 23% compare with the flat layer ($A_T = 0.628 \pm 0.050$) was achieved for the structures with period around 813 nm, for which the total absorptivity amounted 0.771 $\pm$0.059. For the structures with period 345 nm and 1654 nm the 14% ($A_T = 0.722 \pm 0.036$) and 10% ($A_T = 0.695 \pm 0.049$) increase were observed. The enhancement in absorbance for layer with pattern with period 345 nm, corresponding to the Blu–ray structures, is lower than the results presented by Smith et al. [157], who reported 21.8% improvement. The results can not be, however, directly compared because in [157] the authors used a different polymer and a quasi-random pattern obtained from the recorded Blu–ray disc, whereas we examined the purely periodic pattern produced from the unrecorded Blu–ray. In the future it would be worth to examine which discs give better results in sense of light trapping application: unrecorded with period structures or recorded with the quasi-random arrangement. Also we would like to note that the results obtained by us were completely new at the time of performing the experiments and were presented on a conference in 2012.

Apart from the absorption spectra we monitored the back–side reflection (Figure 5.7B). In the range 400 nm - 550 nm the imprinted pattern doesn't have significant influence on the back–side reflection, but for higher wavelength up to 650 nm we observed a slightly drop in reflection for structures with period 813 nm. However, the changes are relatively low, of only about 0.25%. Based on these results we concluded that the increase in absorption is caused mainly by the scattering of the incoming light on the periodic structures, rather than by the expense of the back–side reflection.

Organic solar cells with blended active layer

As we have already shown in a previous paragraph the patterning of absorption layer increases the absorption. The question now is whether the increase in the absorption of the active layer can lead to an improvement of the overall performance of organic solar cells. Here we concentrated on the patterns prepared from DVD, which according to our previous study cause the highest improvement in absorbance.

The solar cells were prepared in a routine manner with one exception. After coating the active layer (composed of P3HT:PC$_{60}$BM) we used the solvent–assisted micromolding to prepare the periodic structures. As reference cells we took two flat devices without imprinted pattern with the total of 12 pixels. After the imprinting an Al electrode was evaporated and the solar cells were encapsulated. As expected, the imprinted devices show a visible optical grating effect, resulting in the rainbow spectrum similar to a DVD disc. The appearance of the rainbow spectrum was the first indicator whether the imprinted process was successful or not. To obtain the information about the pattern topography we left one device without encapsulation.

Figure 5.9A presents the AFM images of patterned active layer whereas Figure 5.9B the Al electrode. Based on the AFM images the period of active layer amounted 832 ±33 nm and the mean height of the pattern 82 ±8 nm. After the aluminum evaporation the peaks are visibly thicker with period 856 ±15 nm and 76 ±8 nm height.

Solar cells were then characterized through current–voltage measurement under the illumination 500 W/m^2. Commonly the solar cells are examined under the illumination 1000 W/m^2, however, during our preliminary experiment we observed a degradation of the devices under $1000 \ W/m^2$. Therefore to reduce the degradation we decreased the illumination to 500 W/m^2. Each set of solar cells either flat or with an imprinted active layer consists of 12 measurements. Figure 5.10 shows the example of the best J–V characteristics we obtained. In such case imprinting an active layer led to 20% increase in the short current (J_{sc}) from 2.63 to 3.17 mA/cm^2. Unfortunately, the imprinting causes the decrease in the remaining parameters and consequently to a decreased efficiency.

The decrease in fill factor (FF) manifests either with decrease of shunt resistance (R_{sh}) or increase in series resistance (R_s) or both of them. To check the changes in resistance we extracted both parameters (R_{sh}) and (R_s) from the J-V characteristic (Figure 5.10) by fitted the curved described by the equation 2.2. In fact we observed decrease in R_{sh} from 1150 to 520 $\Omega \cdot cm^2$ and increase in R_s from 3.9 to 16.7 $\Omega \cdot cm^2$ after imprinting the active layer. In our case, we suppose, that changes in resistivities may be explained by nonuniform metal contact of Al cathode similar as was observed by Na et al. [64] The problem with reduction of the fill factor for pattern organic solar cell was also reported by Nalwa et al. [71]. They observed a reduction in OPV performance (in all parameters) for organic solar cell with pattern substrates with periods 600 nm, 800 nm and 1 μm and an improvement only for the period 2 μm. Additionally, authors also showed that not only period but also height of pitch plays
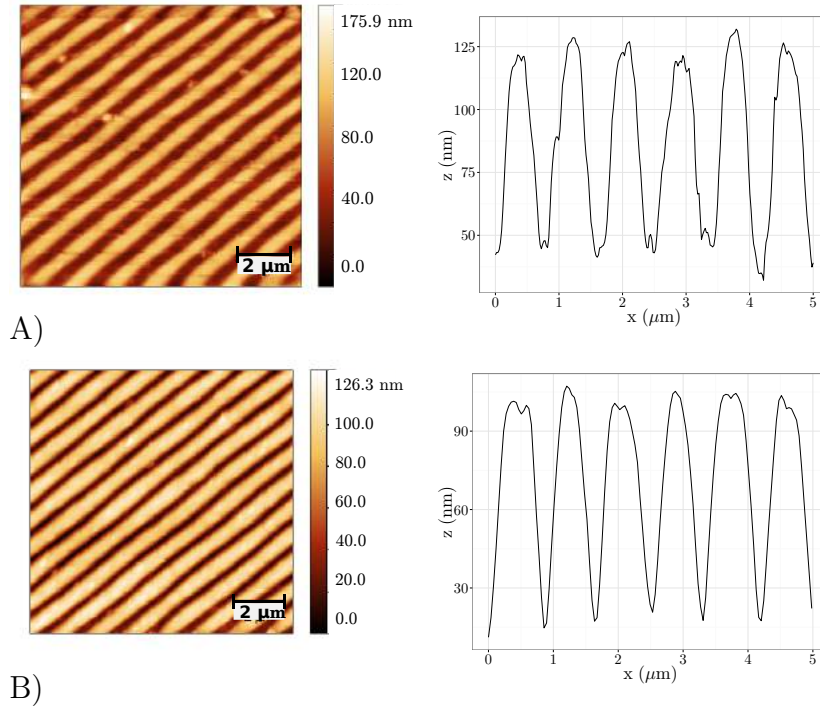
Figure 5.9: AFM images with the examples of the depth profiles: A) imprinted active layer with period 830 nm, B) Aluminium layer evaporated on the top of imprinted active layer.

an important role in device performance. Therefore we are aware that the better height control is crucial for further improvements of OPV.

Apart from decrease in FF we also observed significant drop in open–circuit voltage V_{oc}. In general, V_{oc} is related to the energy difference between donor HOMO level and acceptor LUMO level (equation 2.5) so on the first sight we should not observe such discrepancy in V_{oc} as the same donor and acceptor materials were used in flat and imprinted solar cells. However, as studies showed [41] there are a lot of additional factors which directly or indirectly affect the V_{oc} among others: defects state, micro structures, donor–acceptor interface, morphology, carrier density, recombination, temperature, illumination intensity. Here based on the shape of J–V curves, AFM images (Figure 5.9) and also [41, 156] we suppose that decrease in V_{oc} may be caused by non homogeneous film surface with visible microstructures which can be a source of additional traps or recombination centers and can induce local shunts. The similar decrease in V_{oc} was also observed by Maier [156], where the author examined OPV with imprinted periodic sinusoidal structure in PEDOT:PSS layer. The author attributes the decrease in V_{oc} to morphological changes in PEDOT:PSS layer. Additionally, the patterning of the active layer can change the crystallinity and molecular ordering in polymer films [163] and as a result modifying the charge transport properties and also
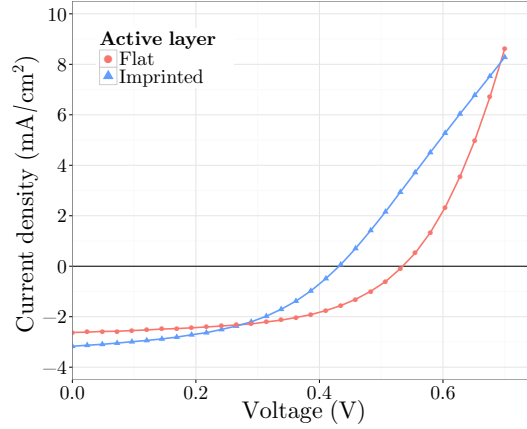
Figure 5.10: Comparison of current density–voltage characteristics for flat and imprinted P3HT:PC$_{60}$BM solar cell with period ~800 nm.

Layer	J_{sc} (mA/cm^2)	V_{oc} (V)	FF (%)	PCE (%)	R_s $(\Omega \cdot cm^2)$	R_{sh} $(\Omega \cdot cm^2)$
Flat	2.47 ±0.17	0.53 ±0.03	53 ±2	1.39 ±0.14	5.5 ±1.7	990 ±180
Imprinted	2.73 ±0.28	0.41 ±0.05	42 ±5	0.96 ±0.25	22 ±10	380 ±200

Table 5.1: Device parameters of solar cells based on the blend P3HT:PC$_{60}$BM with the flat and imprinted active layer. Mean values and standard deviations were calculated from 12 measurement. The period of the pattern was around 850 nm.

shift the molecular orbital level of polymers [164]. However, to determine whether in our case the molecular reorientation or changes in crystallinity occurred the additional measurement would be necessary (e.g. grazing incidence X–ray diffraction).

Figure 5.11 and Table 5.1 summarize the performance characteristics for all measurements with calculated mean values and standard deviations. We showed that apart from the short current density, which mean values increase from 2.47 mA/cm^2 to 2.73 mA/cm^2 resulting 10.5% improvement, the overall solar cell performance decrease. The reduce in quality displays also in device resistance. For the solar with the flat active layers the value of the serial resistance amounted 30 $\Omega \cdot cm^2$ compare to 49 $\Omega \cdot cm^2$ for the imprinted ones. The shunt resistance changed from 1330 $\Omega \cdot cm^2$ for flat solar cell to 470 $\Omega \cdot cm^2$ for imprinted ones. Even if the patterning caused the 10.5% increase in light absorption the improvement in efficiency has not been realized.

Conclusions

The presented results show that imprinting of the active layer influences the solar cells performance. Although we observed a decrease in the the efficiency, the improvement
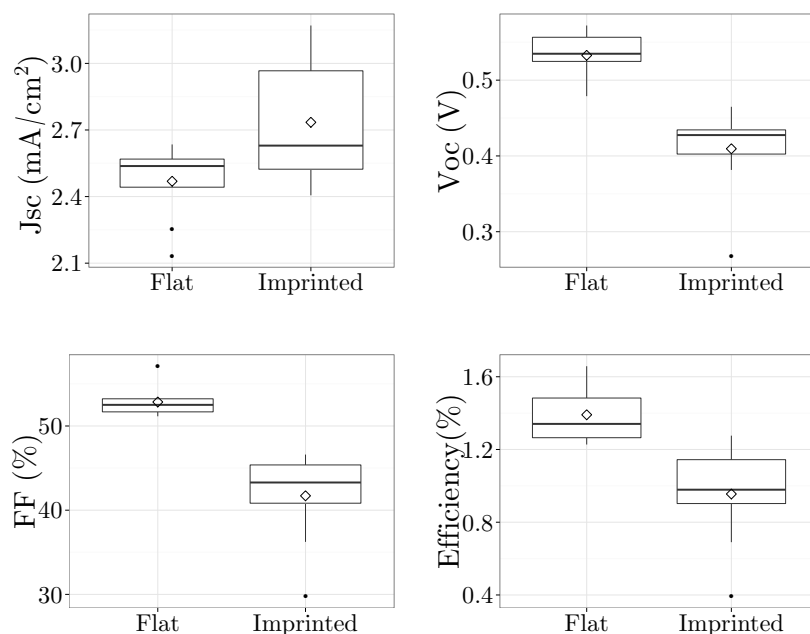
Figure 5.11: The summarized organic solar cells parameters for flat and imprinted active layer.

in the absorption and the short circuit current indicate a potential for using DVD stamps for patterning the active layer. Additionally, our experiment shows the cheap commercially available disc can successfully serve as a master for elastomeric stamps in soft lithography. We think that this idea may find many application not only in material science but also in biology or chemistry.

5.1.2   Periodic grating as the external light trapping structures

Introduction

In the previous section we showed that imprinting the active layer with periodic structures increases absorption and short-current density in the OPV. On the other hand, it turned out that such structures have a negative impact on other OPV parameters such as shunt resistance, fill factor or open circuit voltage thereby reducing the efficiency of the device. Nevertheless, there are several studies [64, 155, 157, 165] which showed that by optimizing the structure parameters or by fine tuning the preparation techniques an OPV with an imprinted active layer can perform better then their flat counterparts. From the commercial perspective, however, the internal light trapping layers are not the best solution due to low throughput of the manufacturing process.

Recently, however, Myers et al. [75] proposed an alternative approach — to attach an external light trapping layer on the incidence surface of an OPV device as depicted in Figure 5.1A. They examined microlens arrays attached to several OPVs with different types of active layers and showed that the efficiency improves in each case. As the authors emphasize, the main advantage of this approach is the ability to apply the light trapping layer on top of already optimized devices without having to interfere in their internal structures. Cho et al. [154] showed that even simple 1D V–shaped periodic arrays (with a period of 50 μm) can enhance the performance when attached to the external surface of an OPV.

Inspired by these results we investigated whether external periodic structures with periods corresponding to CD and DVD discs can have positive impact on the OPV performance. To our knowledge this is the first time CD and DVD structures were studied as external scattering layers (other groups have studied different structures). Below we present results for OPV devices based on two different active layers: conventional P3HT:PC$_{60}$BM as in [75] and PCDTBT:PC$_{70}$BM as in [154]. From the experimental design point of view, the advantage of the external light trapping layer over the integrated structures lies in the possibility to directly measure their impact on the OPV performance by comparing the device parameters before and after attaching the light trapping layer.

Experimental

Fabrication of periodic structures   The periodic structures were imprinted in the poly–(methyl methacrylate) PMMA layer using solvent–assisted micromolding (SAMIM) technique. As the first step PMMA ($M_w = 65kD$, polydispersity index 1.05) was dissolved in toluene with total polymer concentration 20 mg/ml. Then using spin–coating (rotation speed 1000 rpm for 30 s) an uniform PMMA layer was prepared on a glass substrate. Next, applying SAMIM we imprinted the periodic structures with period corresponding to CD and DVD discs. The elastomeric PDMS stamps were prepared in the same way as described in previous Section 5.1.1.

Absorption and topography measurement   As an absorption layer we used poly(3-hexylthiophene) P3HT cast on the back side of glass substrate with previously prepared periodic structures (Figure 5.12). P3HT was prior dissolved in chloroform (20 mg/ml) and then spin coated with rotation speed 1000 rpm for 30 s. Absorption spectra were collected using the same experimental apparatus described in Section 5.1.1

The topography of imprinted structures was examined by atomic force microscopy working in contact mode. The period of the structures and their height were calculated from the Fourier transformation of images and their line profile using Gwyddion software.
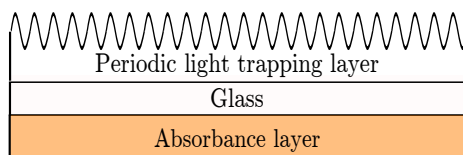

Figure 5.12: Samples used for absorption and topography measurement. Periodic structures were prepared on an glass substrate, whereas an absorption layer poly–(3–hexylthiophene) P3HT was placed on the opposite side of glass.

OPV fabrication and characterization   The first set of OPV devices was prepared based on the mixture of poly(3-hexylthiophene) P3HT and [6,6]-Phenyl C61 butyric acid methyl ester $PC_{60}BM$. Materials were dissolved separately in chlorobenzene (20 mg/ml) and kept on a hotplate for one day (60°C). Next, P3HT and $PC_{60}BM$ were blended in a vol. ration of 1 to 0.6. For the second set we used Poly[N-9'-heptadecanyl-2,7-carbazole-alt-5,5-(4',7'-di-2-thienyl-2',1',3'-benzothiadiazole)] PCDTBT as a donor and $PC_{70}BM$ as an acceptor, separately dissolved in chlorobenzene (7 mg/ml) and then blended in a vol. ration 1 to 4.

Pre–patterned ITO glass substrates (Ossila Limited) schematically presented in Figure 3.5B were cleaned by ultrasonication in acetone and isopropyl and then for 20 s treated with oxygen plasma. Next using spin coating (4000 rpm for 30 s) a thin PEDOT:PSS layer was prepared which was then annealed on a hotplate at 150°C for 5 min. The samples were transferred into a glove box where an active layer was spin coated. For a mixture of P3HT:$PC_{60}BM$ the speed coating parameters amount to 3000 rpm and 30 s, for PCDTBT:$PC_{70}BM$ 500 rpm and 60 s. As a next step an aluminium electrode with thickness 80 nm was thermally deposited. Devices based on P3HT:$PC_{60}BM$ were additionally post annealed at 150° for 15 min. To protect the devices against degradation all of them were encapsulated using UV curable epoxy.

For all devices the current–voltage characteristics were collected using computer–controlled source meter units. The measurements were carried out under the irradiance of 500 W/m^2 using a solar simulator with AM1.5G filter. Each solar cell pixel was measured before and after adding the periodic light trapping layer.
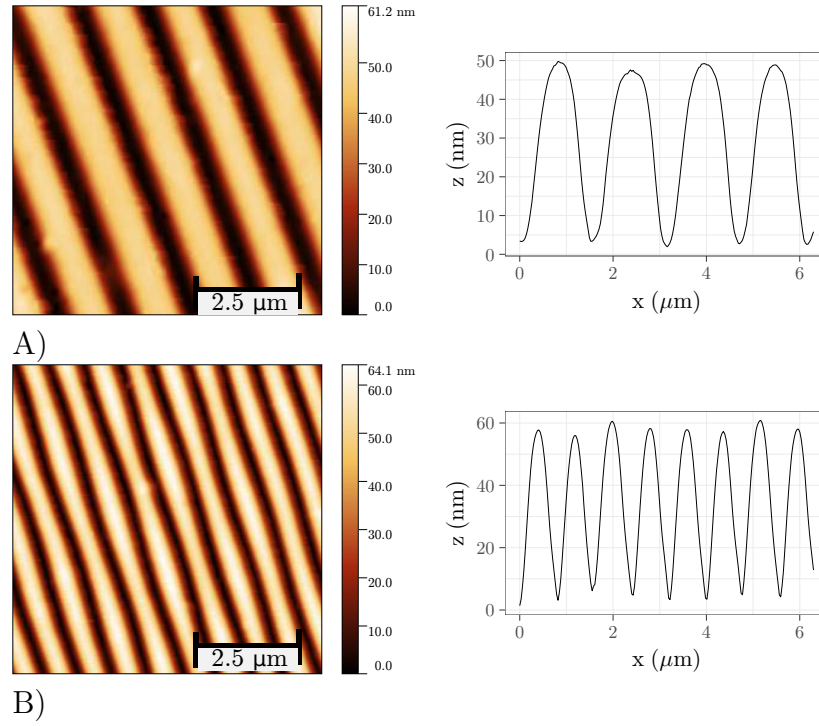
Figure 5.13: AFM images with the examples of the depth profiles for external periodic light trapping structures prepared in poly(methyl methacrylate) PMMA layer: structures A) with period 1620 nm corresponding to CD disc, B) and 820 nm as DVD disc.

Results and discussion

Before we examined the impact of external periodic structures on the OPV performance we conducted a preliminary experiment to check the quality of the imprinted periodic structures and how they influence the light absorption in the active layer. The test samples were prepared with two layers cast on the opposite sides of the same glass substrate as showed in Figure 5.12 — a transparent, non–conductive poly(methyl methacrylate) PMMA layer with imprinted periodic structures acting as light trapping layer and a flat absorbing poly(3–hexylthiophene) P3HT layer.

Figure 5.13 presents the topography and profile cuts of imprinted PMMA layers with periods corresponding to CD and DVD discs. The structures were prepared by solvent–assisted micromolding (SAMIM) using elastomeric PDMS stamps fabricated in the same way as in Section 5.1.1. As the AFM images reveal, in both cases we obtained well–defined periodic, sinusoidal structures with long range order similar to the pattern formed in conductive poly(3–octylthiophene) layer (described in Section 5.1.1 and presented in Figure 5.6). The period of these structures equals to 1620 ±60 nm and 820 ±23 nm while their mean heights amount to 47 ±4 nm and 45 ±8 nm, respectively. As can be seen using SAMIM technique one can successfully transfer the
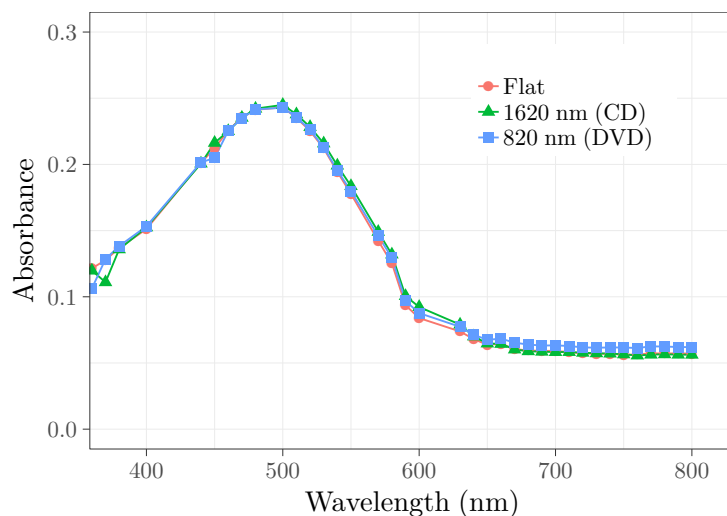
Figure 5.14: Comparison of absorbance spectra of P3HT with flat and imprinted PMMA layers.

pattern from the stamp onto the conductive or non-conductive polymer layers.

In the next step we analyzed the impact of these periodic structures on the light absorption in a P3HT layer coated on the opposite side of the glass (Figure 5.12). The collected absorption spectra, presented in Figure 5.14, showed no visible changes in absorbance for samples with both periodic structures 820 nm and 1620 nm. Additionally, the spectra overlap with the ones received for a sample with a flat PMMA layer. This result suggests that the analyzed external periodic structures do not change significantly the direction of light propagation thus do not increase the optical pathways inside the absorbed layer and therefore the chance of photon absorption. Our observations are consistent with the results obtained from the simulation, prepared by Dr Haberko, which showed that periodic structures similar to DVD and CD discs do not act well as neither the antireflection structures nor the scattering layers. In both cases the light transmission does not exceed 96.5% and mean scattering angle amounts to 5.4° for a period 1600 nm and 7.1° for 800 nm [77].

OPV with periodic light trapping layer   Despite the discouraging preliminary results we were interested whether the periodic structures change the parameters of an actual OPV as, according to the simulation, they should deflect the light, even if only by few degrees. To investigate that claim we compared the OPV performance of the same devices before and after attaching the periodic structures. Additionally, to explore the effect of the degradation of our OPVs throughout repeated measurements we prepared a control group by leaving some of the devices unmodified.

The OPV's active layers with bulk heterojunctions were based on two mixtures; P3HT:PC_{60}BM and PCDTBT:PC_{70}BM. The external periodic structures were pre-
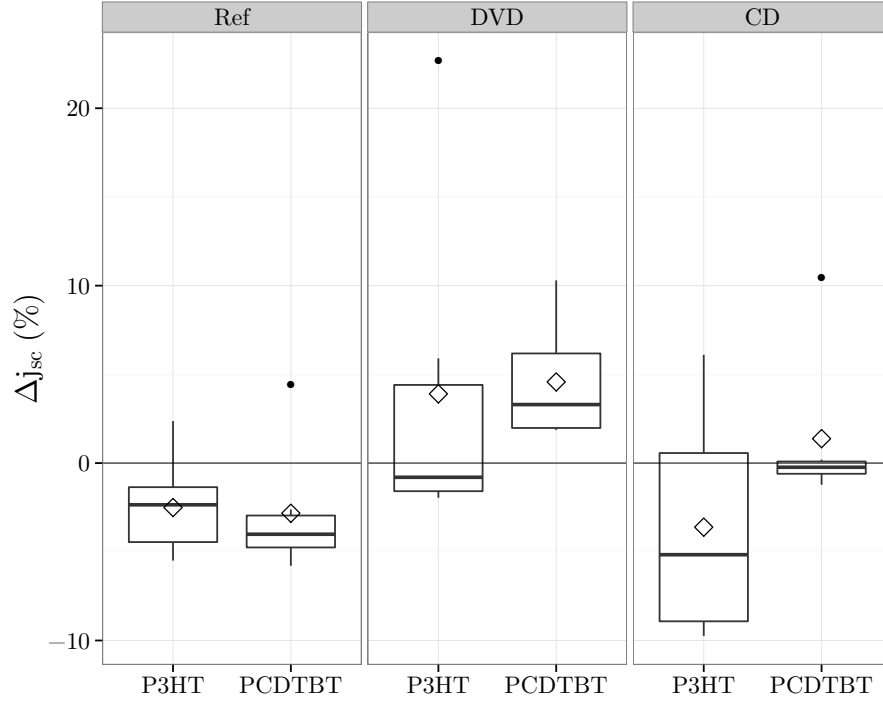
Figure 5.15: The changes in short current density (Δj_{sc}) due to external periodic light trapping layer with two different period corresponding DVD and CD disc prepared via soft lithography. Additionally, the results for unmodified reference devices (Ref) are presented.

pared on the light incidence side of the device (as schematically depicted in Figure 5.1A) by SAMIM techniques. Similar to the absorption measurements, the light trapping layers were made of PMMA. Each solar cell was characterized by a current-voltage measurement under illumination of 500 W/m². Based on at least 6 measurements we calculated the mean values and standard deviations of OPV parameters before and after patterning, the results are summarized in Table 5.2. Additionally, for each solar cell we determined the percentage change in short–current density Δj_{sc} because j_{sc} is influenced mainly by the amount of absorbed light. The results are presented as boxplots in Figure 5.15 with marked medians (lines inside the box) and the means (diamond symbols).

Let us concentrate on the changes in j_{sc} presented in Figure 5.15. Firstly, there is a drop in the current density observed for both types of reference samples based on P3HT:PC$_{60}$BM (median value for $\Delta j_{sc} = -2.3\%$) and PCDTBT:PC$_{70}$BM ($\Delta j_{sc} = -4.0\%$). Even if the the drop for PCDTBT is bigger than for the P3HT the interquartile range indicated the smaller spread of values. The problem with degradation and stability of organic solar cell is widely known [24,166–168] and it is one of the reasons

why OPVs have so far not successfully entered the market.

As for the imprinted samples, the best results were obtained for structures with periods corresponding to DVD discs for which, according to the simulation, we expected a slightly broader scattering angle compared to the CD structures. For solar cells based on PCDTBT:PC_{70}BM we observed an increase in j_{sc} for all measured devices with a median improvement of 3.3 % in short current density. This is not a big change, however if we compare it with the reference samples, where degradation after the first measurement is significant, the changes can be interpreted as up to 7% relative increase. In case of devices based on P3HT, the changes in j_{sc} oscillate around zero. For OPV devices with external structures corresponding to the pattern on CD disc (Figure 5.15) we observed either no changes in median short current density (j_{sc}) for solar cell PCDTBT:PC_{70}BM or decrease for P3HT:PC_{60}BM.

Table 5.2 summarizes performance characteristics for all measured devices. Compared to devices with internal light trapping layer (see Table 5.1 in the previous section) here we do not observe significant decrease in open–circuit voltage V_{oc} and fill factor FF. These results show that external light trapping layers do not negatively influence the electrical properties of our OPV devices.

PCDTBT	Flat	Ref	Flat	DVD	Flat	CD
J_{sc} (mA/cm^2)	1.39 ±0.15	1.36 ±0.12	1.86 ±0.20	1.93 ±0.17	1.72 ±0.17	1.74 ±0.14
V_{oc} (V)	0.76 ±0.02	0.74 ±0.02	0.77 ±0.01	0.77 ±0.01	0.72 ±0.09	0.71 ±0.10
FF (%)	60 ±6	60 ±2	50 ±9	51 ±8	43 ±10	43 ±10
Efficiency(%)	1.27 ±0.16	1.21 ±0.16	1.43 ±0.28	1.52±0.27	1.07 ±0.21	1.06 ±0.23

P3HT	Flat	Ref	Flat	DVD	Flat	CD
J_{sc} (mA/cm^2)	2.09 ±0.22	2.04 ±0.19	1.71 ±0.41	1.77 ±0.40	1.74 ±0.31	1.68±0.30
V_{oc} (V)	0.58 ±0.02	0.57 ±0.02	0.57 ±0.01	0.55 ±0.01	0.55 ±0.02	0.53 ±0.02
FF (%)	54 ±3	53 ±3	56±4	54 ±4	54 ±4	54 ±4
Efficiency(%)	1.31 ±0.18	1.23 ±0.16	1.09 ±0.30	1.05±0.27	1.03 ±0.26	0.96 ±0.21

Table 5.2: Performance parameter of OPV before (Flat) and after assembling the external light trapping layer with period corresponding to DVD (800 nm) and CD disc (1600 nm) and also without any pattern (Ref). The first table presents the results for devices based on PCDTBT:PC_{70}BM, the second one for P3HT:PC_{60}BM.

Conclusions

To our knowledge this is the first time CD and DVD structures were studied as external scattering layers (other groups have studied different structures). Based on the absorption measurements and OPV characteristics we demonstrated that the external periodic light trapping layers with periods 1600 nm and 800 nm do not significantly

affect the performance of OPV devices. In most cases we observed no change in absorbance in active layer and short–current density with a singular exception of devices based on PCDTBT:PC$_{70}$BM with an external light trapping layer corresponding to DVD disc where an increase in j_{sc} for all measured samples was recorded. These observations are compatible with simulation results showing slightly higher deflection angles for structures corresponding to DVD patterns.

To conclude, we showed that such periodic structures are not good candidates for external light trapping structures. At the end, however, it is worth mentioning that the adding these layers to the previously prepared and characterized OPV devices does not degrade the solar cells. The challenge now is to explore other structures, possibly with higher scattering angles. In the following sections we show that random porous structures can fulfill this role.

5.2 Breath figure structures

In this part of the thesis, we use self–organized breath figure structures as external light trapping layers for organic solar cells. Such porous structures are formed by deposition of a polymer solution in a humid atmosphere (Figure 5.16). Due to evaporative cooling during solution deposition, droplets of water condense on the surface of polymer solution. These droplets sink into the solution and form so called breath figure patterns after complete drying [169]. Porous structures formed this way are uniform over large areas and can be used as light trapping or antireflective coatings [55, 97]. Light trapping behaviour is sensitive to the structures size [46]. With the breath figure approach it is possible to control the pore size by varying relative humidity, type of polymer, solution concentration or amount of water in the solution (see [95, 170] for a comprehensive review). In this work we extend the previous studies on the influence of different parameters on the breath figure formation with the main emphasis on the practical application of the structures as the light trapping layers for organic solar cells.

Firstly, in Section 5.2.1, we discuss the influence of the breath figures prepared under high humidity onto the optical properties. The results are compared with the theoretical simulation prepared by dr Jakub Haberko. In Section 5.2.2 we implement the breath figures layers as the external light trapping layer in organic solar cells and we measure the changes in efficiency of the OPV. Finally, in Section 5.2.3, for the first time we present the breath figure with diameter and depth gradients prepared by h-dipping methods.
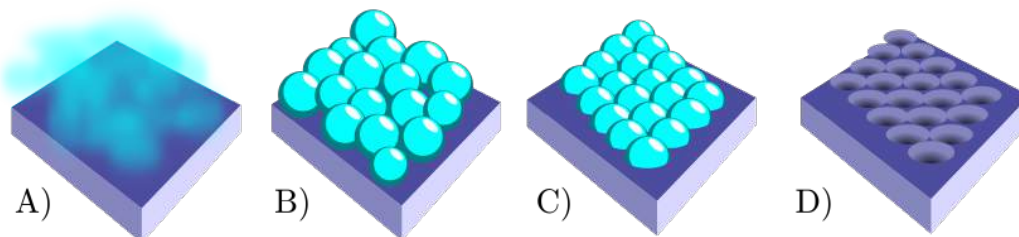

Figure 5.16: The illustration of the breath figure mechanism. Due to evaporation of the solvent (A) the solution surface is cooled and caused the nucleation of the droplets (B), which then sink into the polymer solution (C). After the evaporation the porous pattern is formed (D).

5.2.1 Breath figure structures and optical measurement

In the first experiment we were interested how breath figure structures affect the light absorption in a polymer layer. To test this we prepared the breath figure pattern on one side of a glass slide and we placed the absorbance layer on the opposite side (Figure 5.17). We observed that all of the breath figure patterns increase the absorbance but the biggest improvement comes from the patterns which have their diameter and depth distributions concentrated around 0.40 μm and 0.15 μm, respectively. In fact, the more concentrated the distribution is, the higher the absorbance. To get the structures with different depths and diameters we varied the relative humidity between 40% to 90% during the breath figure creation. We also compared our experimental results with simulations performed by dr Jakub Haberko in which the dependence of light scattering and transmittance on holes shapes was examined.

Experimental

Fabrication of thin layers: For the preparation of the breath figure layer, poly–(methyl methacrylate) PMMA, $M_w = 58300$, polydispersity index $M_w/M_n = 1.06$, was dissolved in tetrahydrofuran (THF) with total polymer concentration 20 mg/ml. The solution was spin-coated onto glass substrate using a coater(KW–4A, Chemat Technology) extended with a home–made system [171] to monitor and adjust the relative humidity (RH) in the coating bowl. Samples were prepared with rotation speed 1000 rpm under relative humidity values varying from 40% to 90%. As an absorption layer we used poly(3–octylthiophene) P3OT spin–coated from 20 mg/ml solution in chloroform on the back side of glass substrate with previously prepared breath figure structures.
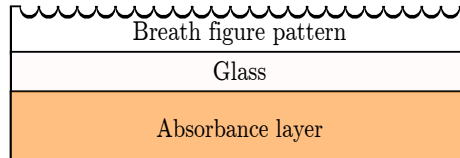

Figure 5.17: Breath figures, acting as light scattering structures, were prepared on an glass substrate, whereas an absorption layer, poly(3–octylthiophene), was placed on the opposite side of glass.

Morphology characteristics: The breath figure layer was characterized using atomic force microscopy (Agilent 5500). Topographic images were analyzed by Gwyddion software using Grain analysis [112]. Additionally, raw data from Gwyddion were exported and explored using statistical program R.

Optical spectra measurements: The absorption and reflection spectra of P3OT layer were measured by a system built in our laboratory [115]. The entrance slit with was set
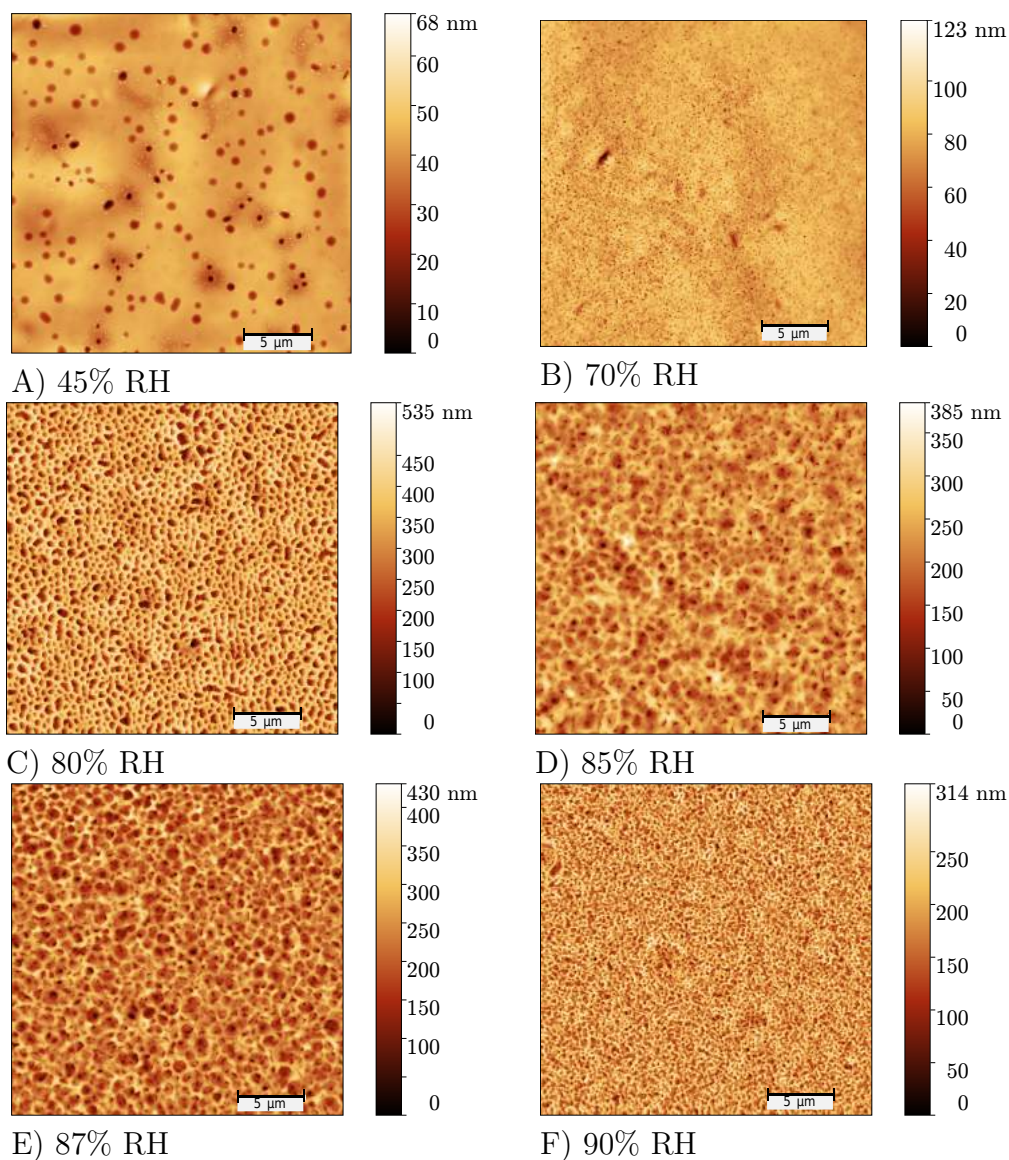
Figure 5.18: AFM images of breath figure patterns prepared under different relative humidity conditions varied from 45% RH to 90% RH. The structures were prepared by spin coating (1000 rpm) of PMMA in THF.

to 40 μm, the output slit to 10 μm. The data was collected by the Silicon Detector (Newport Model 71889) with transimpedance gain 10^7 and the chopper constant 75 Hz.

Results and discussion

Breath figure methods allow to prepare roughly spherical cavities of varying geometry, differing with respect to their shapes, dimensions and the way of packing. Generally,

however, we can divide these structures into two groups: regular array of pores in a hexagonal lattice and irregularly packed pores with broad size distribution. As studies show, the final appearance depends on many factors: relative humidity, type of polymer and solvent, solution concentration, polymer molecular weight, type of substrate, preparation methods, temperature and many others [95,170,172]. In this study we concentrated on structures formed from PMMA (molecular weight 58300 g/mol) dissolved in THF (concentration 20 mg/ml) and spin-coated (1000 rpm) on the glass substrate under the moist atmosphere (varying from 40% to 90% RH). For such parameters, as AFM measurement showed (see Figure 5.18), we obtained irregular pores with relatively small dimensions. Below we present a more detailed analysis.

Topographic measurement We examined the breath figure patterns topography with AFM microscopy, representative AFM images are shown in Figure 5.18. Under the ambient conditions (45% RH) the layers are mostly flat with sparsely placed small holes. With increasing humidity the irregular porous structures become more pronounced, covering up to 40% of the total surface area. To quantitatively describe the packing of the holes we used the Voronoi polygons [96, 173] and we performed the conformation entropy analysis [174].

For the analyzed images the conformation entropy, defined as $S = -\sum P_z \ln P_z$ where P_z is the probability of pores with z nearest neighbors, varies from 1.37 to 1.49 but there seems to be no correlation between the humidity and the entropy. For comparison, these values are much closer to 1.71 for randomly organized arrays, so our structure seem slightly more ordered. As for the packing analysis, the structures are dominated by pores with six neighbors (40%) with other neighbor counts closely following: 30% of pores have five and 20% have seven neighbors. The neighbor counts are again independent of the humidity.

According to observations [174] the growth of breath figures evolves through several phases. In the first phase, so called initial stage, the droplets are isolated and do not interact with each other. The surface coverage is low, the entropy remains above 1.4 and the average droplet size $\langle R \rangle$ changes with exposition time as $t^{1/3}$. In the second phase, crossover stage, the droplet growth rate significantly increases, the surface coverage is high and the closed hexagonal packing is starting to dominate. In the last stage, coalescence phase, the surface coverage is high and doesn't change in time, $\langle R \rangle$ grows linearly with time. The hexagonal packing still dominates and droplets with five and seven neighbors are scarce but also visible. Comparing our entropy measurements and the distribution of polygons with the results presented in [174] we see that the geometry of our breath figures corresponds perfectly to the ends of initial stage. This was caused by too short evaporation time, preventing the system from entering the second stage.

To quantitatively evaluate the changes in holes depth and area we extracted pore parameters from the AFM images with the grain analysis tool from Gwyddion software [112]. A key element in grain analysis it to mark the structures with an appro-

A)   B)
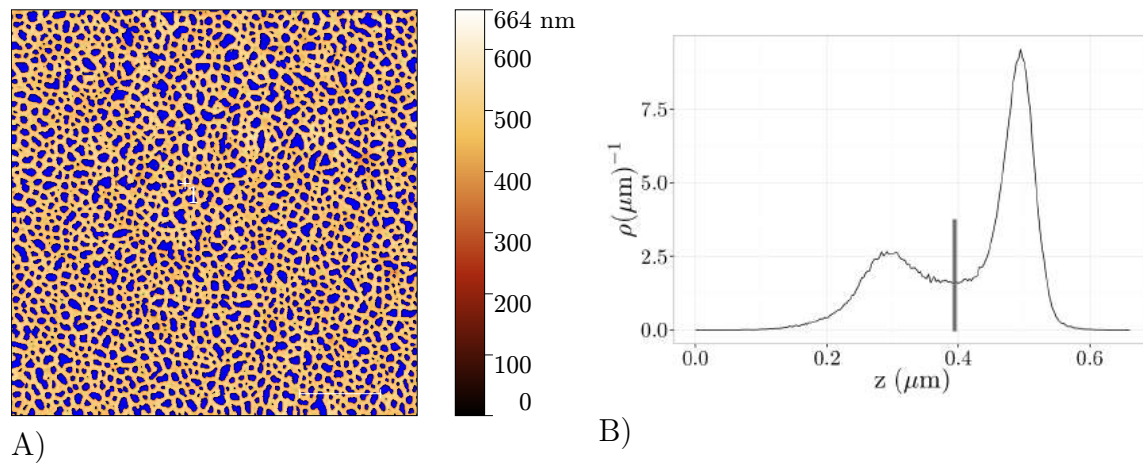
Figure 5.19: A) AFM image of breath figure with the marked pores which were subsequently analyzed by grain analysis tool. The threshold was picked based on the pores height distribution B) as a value between position of two peaks.
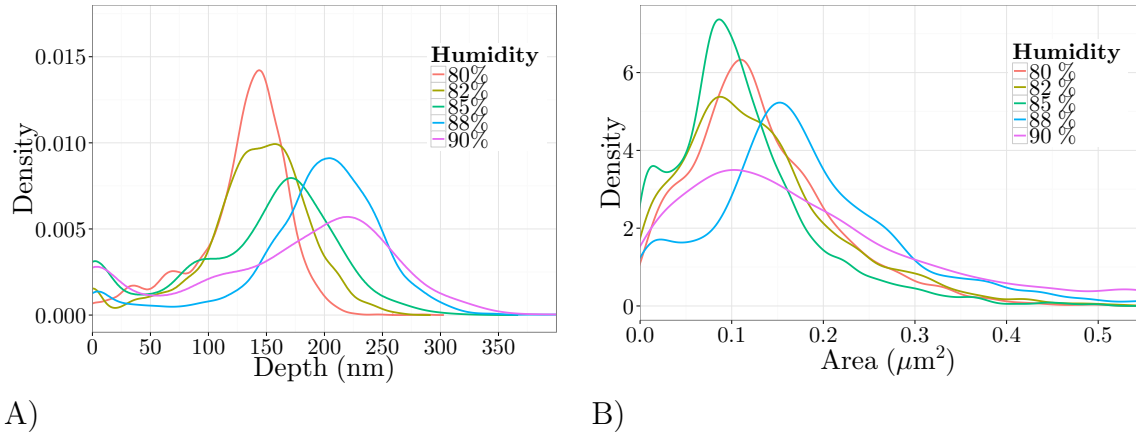

A)   B)

Figure 5.20: A) Depth and B) area distributions of breath figures structures prepared under various humidity.

priately selected threshold (see Figure 5.19A). In this experiment we calculated the threshold based on the bimodal height distribution (Figure 5.19B) [175]. We pick the threshold at a value between the positions of the peaks (the first peak correspond to porous depth distribution and the second the boundary distribution). It is worth to point that in this experiment all the height distributions had the two peaks significantly separated, therefore it was relatively easy to obtain the thresholds. However, in some other experiments we dealt with there were no visible distinctions between the two peaks. In these cases we used different methods to mark the pores: either the watershed or the multi level masks.

After marking the structures different quantities can be obtained like depth, vol-

ume, area, size of each pore. Below we concentrate on two of them – area and depth. However, instead of only calculating the mean values and standard deviation of parameters we firstly present the distribution of the values, which give us more complete pictures of structures.

As Figures 5.20A and B show the depth and area distributions of breath figures change with humidity in which the structures where formed. For humidity 80% distributions are uniform with maximum value about 140 nm for depth and 0.1 μm^2 for area. With increasing humidity the maximum of the depth shifts to the higher value and distributions become broader. In case of area there is no visible shift. However, for the high humidity 90% we observed bimodal distributions with additional holes smaller than 0.05 μm^2.

Despite the fact that there are visible changes in holes distributions it is hard, based only on Figures 5.20, to conclude whether there is any relation between pores dimensions and humidity. To answer this question we propose to present holes distributions as 2D maps (Figure 5.21). Here, instead of holes areas, however, we concentrated on their diameters. This change was dictated by the fact that in optical simulation, in which influence of holes dimension on transmission and light scattering was analyzed (Figure 5.26, 5.24), holes diameters were taken into account. In the next part we confront these simulation with our experimental results.

In Figure 5.21 each 2D map represents depth and diameter distributions for holes prepared under different humidity (the top left map corresponds to 80% RH whereas the last bottom map 90% RH). In the top left picture we see a localized distribution of holes dimensions: the diameters and depths are tightly focused on values (0.35 μm, 0.14 μm). With increasing humidity the distribution of dimensions becomes more spread out. In the final picture, corresponding to the highest humidity the length–scales seem to vanish completely, holes of large diameters coexist with holes of small diameters.

To conclude based on the 2D maps we found that the relation between the humidity and the geometry of the arising structures is involved and difficult to control. In the next part, however, we will show that there is an interesting relationship between these maps and the optical properties of such structures.

Light scattering The breath figure pattern can be used either as the antireflection or light scattering layer. The functionality depends mainly on the dimensions of the structures [48, 60, 176]. In classical silicon solar cells high light reflection has negative impact on the efficiency of devices [60]. As was recently shown by Galeotti et al. [98] the breath figure structures reduce the reflection from the silicon wafers. However, there is still lack of evidence of efficiency improvement for silicon solar cells due to the presence of breath figure structures. In organic solar cells we struggle with other problem. Due to the short diffusion times of charges the absorbing layer should be thin, which decreases the chance of photon absorption. To overcome this issue we can use breath figures as the scattering layer. Due to light scattering optical paths inside
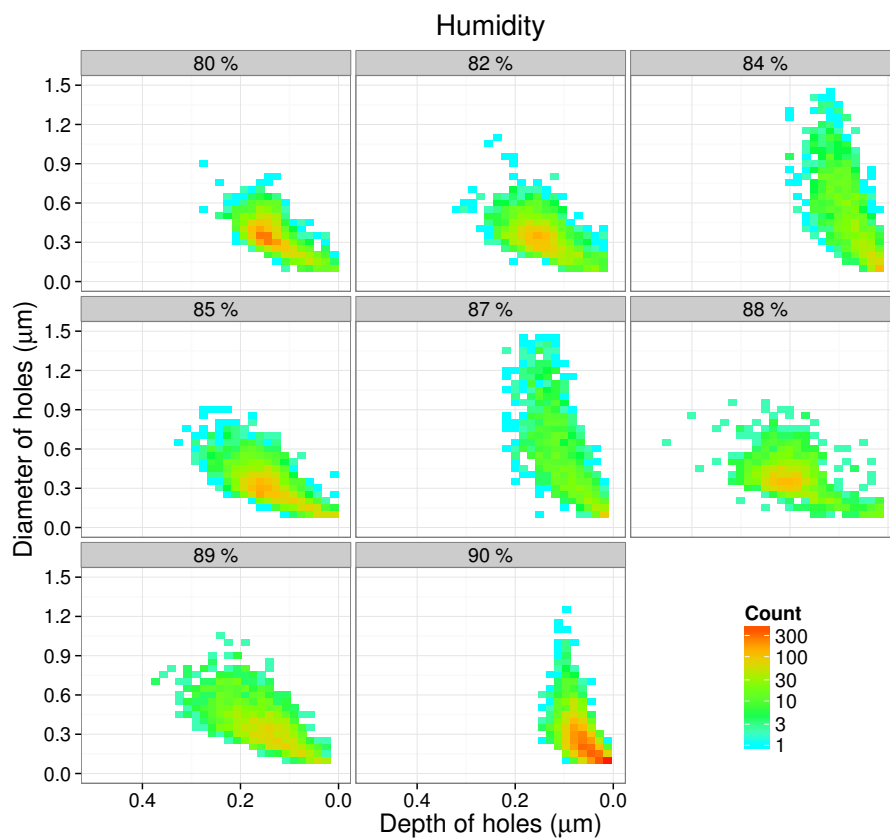
Figure 5.21: 2D map representing the distribution of holes depth and diameter with marked on the top humidity values. The pores dimensions were received on the basis of AFM images using grain analysis tool.
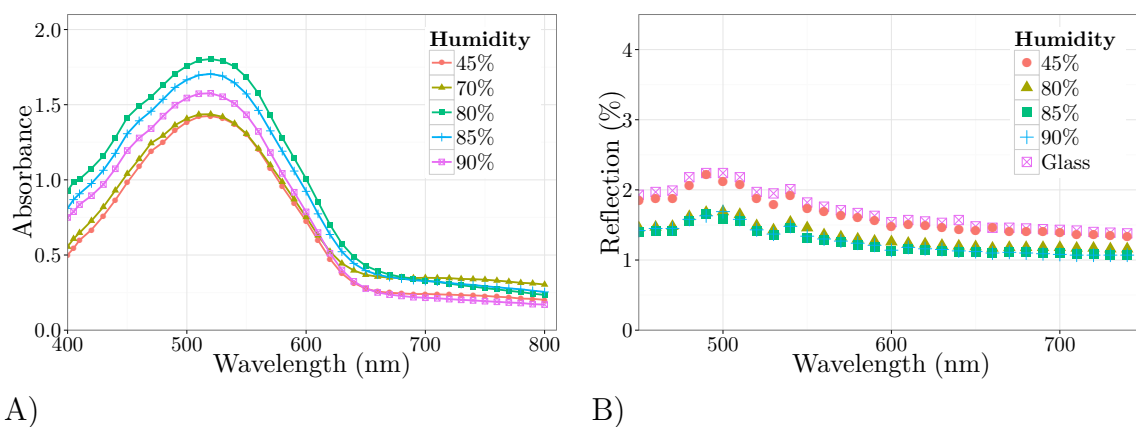

Figure 5.22: The changes in absorbance A) and reflection B) in P3OT films due to the presence of breath figure structures prepared from PMMA solution under various humidity.
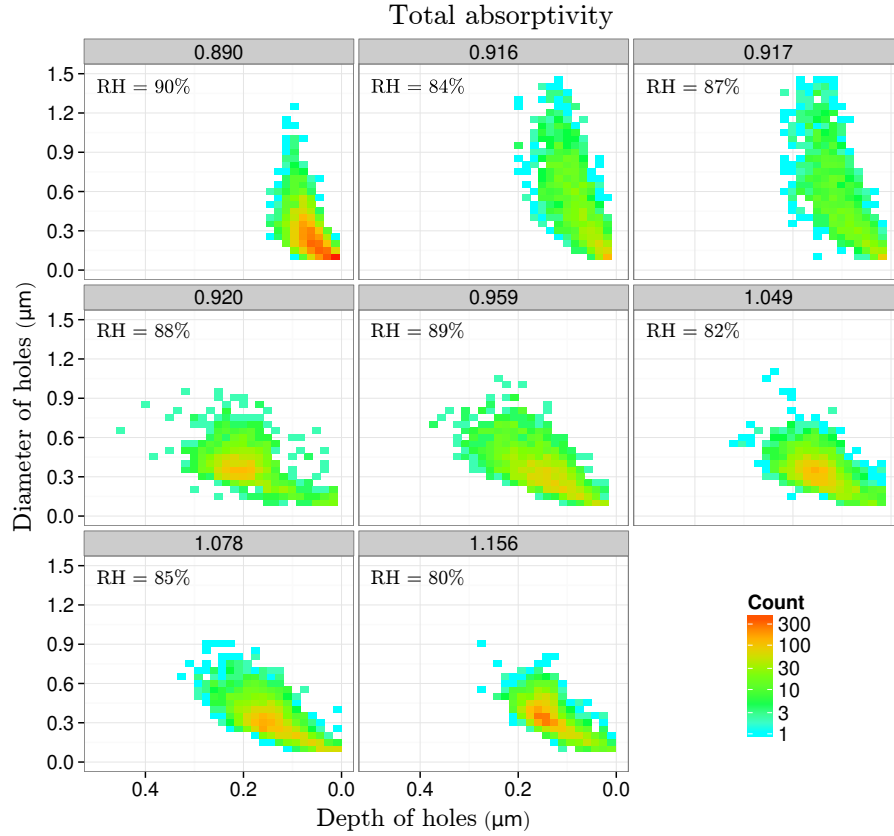
Figure 5.23: 2D map representing the distribution of holes depth and diameter with marked on the top total absorptivity values.

the absorbing layer increase, in consequence the chance of absorption also increases. Below we present the changes in light absorption in poly-octylthiophene (P3OT) films due to the presence of breath figure structures. The results are also compared with the simulation.

The absorption layer was coated on the back side of the glass substrate with previously prepared and examined breath figure structures (Figure 5.17). The representative absorption spectra are presented in Figure 5.22. The samples with flat PMMA layer, prepared under 45% RH and 70% (Figure 5.18A, B), have the lowest absorption in whole spectra. The visible absorption increase is achieved through breath figure structures with the best results for breath figure structures prepared under 80% RH.

What piqued our interest was whether there is some relationship between pores dimensions and absorption. To answer this question we also used 2D map representing the distribution of depths and diameters of the holes, we labeled each plot with total absorptivity values (Figure 5.23). Such presentation leads to interesting observations. Compared to the previous Figure 5.21, here the 2D maps seem to form a more con-
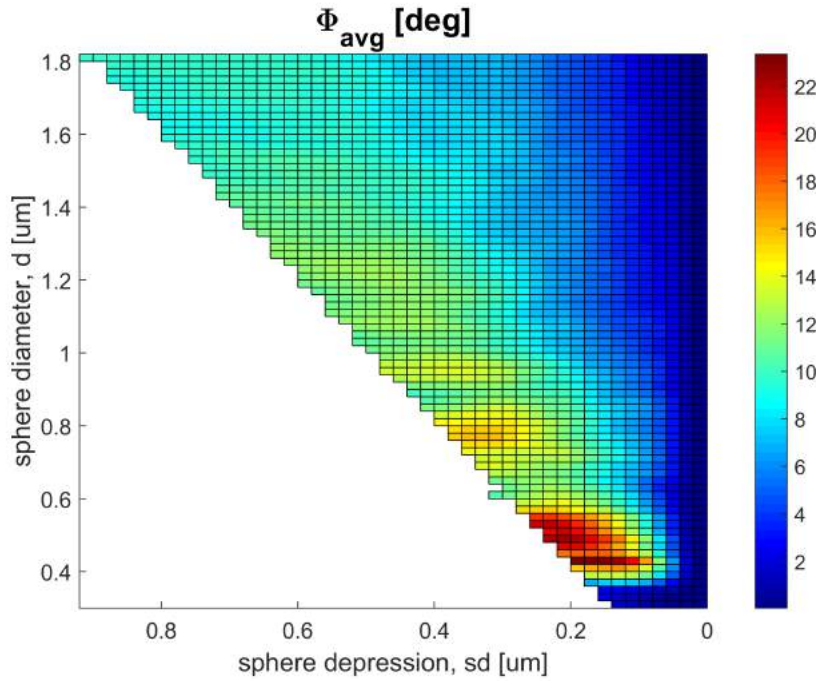
Figure 5.24: Calculated effective scattering angle for different hole depression (sd) and diameter (d). The simulation and calculation was performed by dr Jakub Haberko.

sistent series. The lowest total absorptivity $A_T = 0.890$ corresponds to the structures with depth centered around 0.1 μm but with large spread in diameter. The next two samples with $A_T = 0.916$ and 0.920 have the similar shapes distribution; the pores with broad range of diameter and with narrow depth band below 0.20 μm. The significant increase in absorptivity is evident starting from the second row in Figure 5.23. Here the distribution of shapes is less spread out with visible concentration around 0.20 μm (depth) and 0.4 μm (diameter). The best improvement, up to 30 % ($A_T = 1.156$), was achieved for the narrowest distribution with median 0.15 μm in depth and 0.35 μm in diameter.

As visible even a small changes in dimensions cause significant changes in absorbance. We confronted our results with simulation conducted by dr Jakub Haberko. He simulated the behavior of electromagnetic waves propagating through a model of a porous structure. The simulation analyses the deviation (in terms of angle) of the Poynting vector from the glass normal after the wave passes through a polymer layer with holes. The results are presented in Figure 5.24. The average φ depends strongly on both shape parameters: their diameter and depth. The highest deflection, exceeding 22°, was observed for structures with diameter 0.42 μm and depth from 0.12 to 0.2 μm. In general, however, the structures within the range of 0.38 – 0.54 μm in diameter and 0.12 – 0.26 μm in depth also caused a significant light deflection. Such structures are suitable for light scattering applications. In this experiment we dealt

with holes within this optimal depth range (median values from 0.10 to 0.19 μm) but slightly smaller median diameter values (from 0.22 to 0.45μm). However, as we show in Figure 5.23, the size distribution of holes is broad enough to contain holes with appropriate size in the context of light deflection. In the future it would be interesting to prepare and test the structures with slightly bigger diameters.

Reflection and transmission   As we have shown the breath figure structures can be applied as a light scattering layer. However, as simulations showed (Figure 5.25 and Figure 5.26), such structures can also improve the light transmission and therefore can be applied as an antireflection layer. To check this we measured the back light reflection. Figure 5.22B presents the slight decrease in reflection (by roughly 0.5 %) due to the presence of breath figures compared with uncoated glass or a flat PMMA layer. The decrease seems independent of the breath figures dimensions which differs from the results of the simulation.

According to the results of the simulation, in Figure 5.25 the distance between holes (d) as well as their depression (sd) should have great impact on the transmission of the light. The polymer layer without any holes (sd = 0 in Figure 5.25) would be expected to have the transmission maximum around 500 nm; above it the transmittance drops to value 0.9. In the simulation, the best transmission improvement was achieved when the holes were close to each other, the distance between the holes was about 0.3 - 0.4 μm and the depression was around 0.2 - 0.25 μm. The differences between the simulation and the experimental results might be caused by either us measuring only the back-scattered portion of reflected light or by breath figures being randomly distributed in contrast to regularly spaced holes in the simulation.

Conclusion

Based on the simulations and presented 2D maps (Figure 5.24 and Figure 5.26) there is an overlap, in the context of pores dimension, between the high scattering region and high transmission region. The optimal pores should be within the following size range 0.12 – 0.26 μm (pores depth) and 0.38 – 0.54 μm (diameter).

In our experiment by changing humidity we were able to vary holes depths and diameters. We reported the highest increase in absorptivity, up to 30 %, for structures with depth and diameter both concentrated around 0.15 μm and 0.40 μm respectively, which is in accordance with the results obtained from simulations.

Appendix

Based on the positive influence of breath figures on absorption we made our first attempts to apply the breath figures directly onto the organic solar cells. The preparation of the organic solar cells took place in the different laboratory with the different set-up for humidity control. The main difference in breath figure preparation was using argon instead the nitrogen flux as a carrier of water into the chamber where high
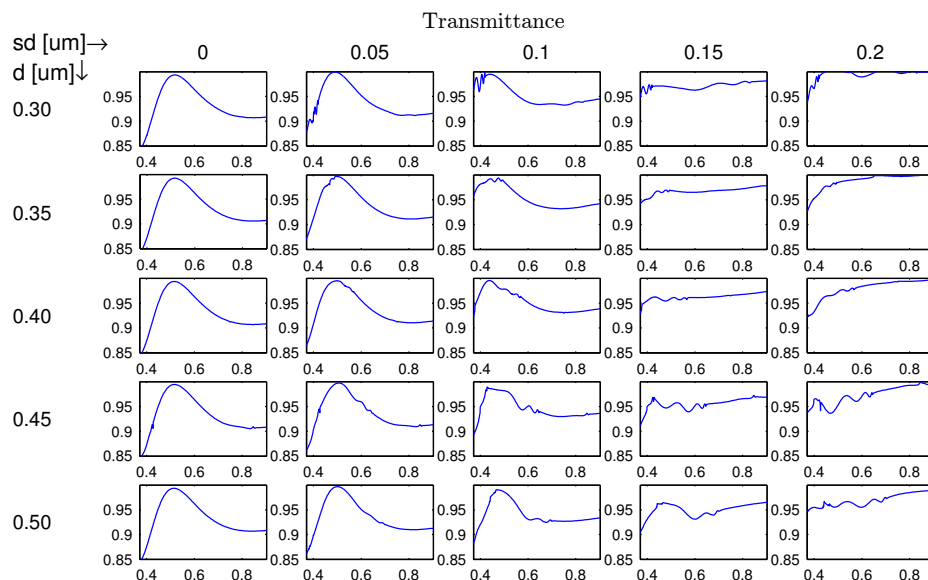
Figure 5.25: The simulation results for light transmission made by dr Jakub Haberko. The graph presents the transmission spectra for holes with different depression (sd) and the distance between the hole center (d).

humidity environment was created. This had a negative impact on the creation breath figures. Even under high humidity no visible breath figures pattern was created as is visible in Figure 5.27. It was clear that for the next experiments we had to alter the method of breath figure preparation: instead of working in high humidity environment we decided on pouring small amounts of water directly into the polymer solution. This strategy allows breath figures to develop even in low humidity.
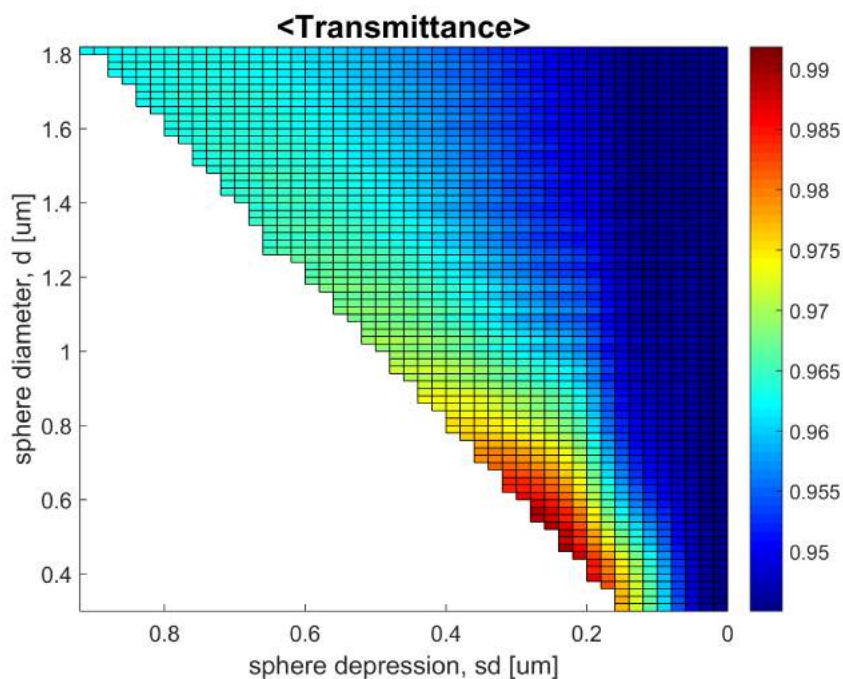
Figure 5.26: Simulation of transmittance prepared by dr Jakub Haberko. The 2D map presents the transmittance for holes with different depression (sd) and the distance between the hole center (d) The transmittance was calculated as a weighted mean (the weight was solar radiance spectrum).
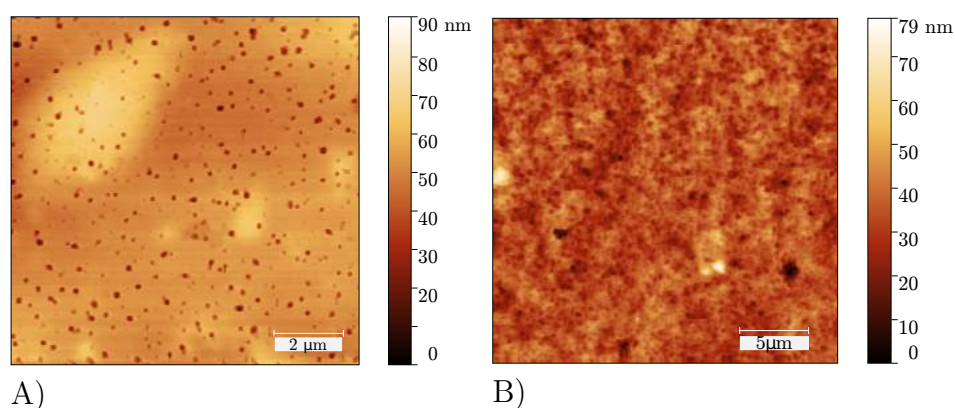

Figure 5.27: Breath figure structures prepared under high humidity A) RH = 84%, B) RH = 90%. However, instead of using nitrogen flux as a carrier here the argon was used.

5.2.2   Breath figure structures as the light trapping layer in organic photovoltaic cells

As we showed in the previous section, when the light passes through a glass coated with breath figures it is scattered in different directions and scatter angles depend on the dimensions of breath figures. The scattering capability of breath figures can find application in organic solar cells for which the increase in optical path inside the absorbed polymer layer is desired.

To check whether the breath figures have a positive influence on the organic solar cell performance we examined OPV devices with breath figures differing in depths (from 80 to 600 nm) and diameters (from 0.5 to 1.6 μm). We reported that the changes in short current density strongly depend on the structures dimensions. The highest improvement, up to 6%, was observed for pores with depths smaller than 320 nm and diameters below 1 μm. On the other hand, deeper and bigger pores turned out to have negative influence and they caused visible decrease in solar cells performance.

Compared to the previous experiment (see Section 5.2.1), here we used a different breath figure preparation strategy. This change was dictated by the fact that breath figures prepared under high humidity characterized with low structures reproducibility and were thus difficult to control. As Park showed [97], by adding water directly into the solution it is possible to obtain similar breath figures, even under ambient conditions. Additionally, it is easier to control water content in the solution rather then high humidity of the environment. As the first step we extended the previous studies [96, 97] on the influence of spin coating parameters, total polymer concentration and water content in solution on the breath figure morphology. We examined not only the size of the pores but also their depth which is an important parameter for light trapping [177].

Experimental

Fabrication of thin layers: For the preparation of the light trapping layer, poly–(methyl methacrylate) (PMMA), $M_w = 65000$, polydispersity index $M_w/M_n = 1.05$, was dissolved in tetrahydrofuran (THF), with two total polymer concentrations: 60 mg/ml and 100 mg/ml. To the prepared solutions we added water (between 2% and 10% vol.) and spin- coated the solution onto glass substrates using a coater (KW–4A, Chemat Technology) extended with a home–made system to monitor and adjust the relative humidity (RH) in the coating bowl. Samples were prepared with two rotation speeds 1000 rpm and 2000 rpm under relative humidity values varying from 5% to 90%.

OPV device fabrication: Electronic grade poly 3-hexyltiophene (P3HT) (Rieke Metals, $M_w \approx 48900$ g/mol) and [6,6]-phenyl-C61-butyric acid methyl ester (PC$_{60}$BM) (Solenne BV, purity $> 99\%$) were dissolved separately in chlorobenzene with polymer concentration 20 mg/ml and kept on a hot plate (at 60°C) for one day. Subsequently,
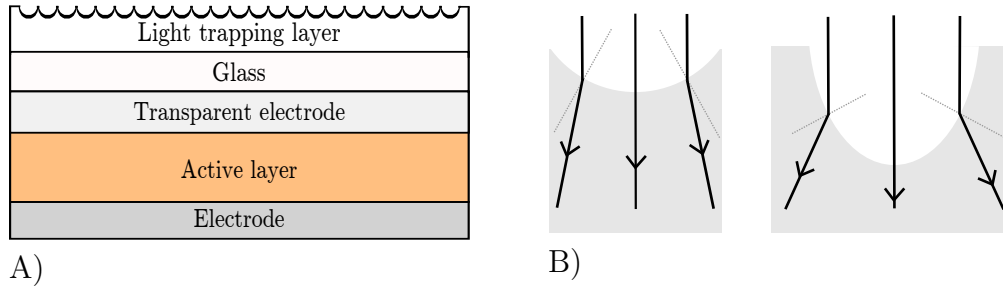
Figure 5.28: A) Schematic solar cell structure with light trapping layer on the top: breath figure layer/glass/ITO/PEDOT:PSS/P3HT:PC$_{60}$BM/Al. B) A schematic figure of light spread at the interface of air and PMMA for two holes with the same diameter but different depth. The deeper hole is more concave and consequently the incident ray is more divergent at the air/PMMA interface, which leads to a longer optical path within the active layer.

the blend of P3HT and PC$_{60}$BM in a vol. ratio of 1 to 0.6 was prepared and left overnight at 60°C.

Pre–patterned ITO glass substrates, with 6 pixels per substrate (Ossila Limited), were cleaned by ultrasonication in acetone and isopropyl and blown dry with nitrogen. As the next step all substrates were treated with oxygen plasma (Zepto plasma cleaner, Diener Electronic, Germany) for 20 s.

Cleaned ITO substrates were transferred into a glove box, covered with PEDOT:PSS (passed through a 0.45 μm filter) spun at 4000 rpm for 30 s and then annealed at 120°C for 20 min on a hotplate. On the top of the PEDOT:PSS a layer of P3HT:PC$_{60}$BM was spin-coated at 3000 rpm for 30 s. An aluminium electrode (80 nm thick) was thermally deposited on the top of the active layer.

After aluminium deposition all devices were annealed (at 150°C for 15 min) and encapsulated using UV curable epoxy (Ossila Limited) and a glass slide. The resulting active area of one pixel of the solar cell was 6 mm^2. At the end the breath figure light trapping structures were prepared on the front side the organic solar cells (Figure 5.28A) as described above.

Characterization: The surface of the light trapping layer was characterized using atomic force microscopy (Agilent 5500) in contact mode. Topographic images were analyzed by Gwyddion software using Grain analysis [112]. The mean and standard deviation of depth and area of holes were calculated from several AFM images (at least 5). The current-voltage characteristics of the solar cells were measured with computer-controlled source meter units (Keithley 2400) under the irradiance of a solar simulator with AM1.5G filter (Newport 150 W). In most cases we used 500 W/m^2 flux density to reduce the degradation of the solar cells. For each solar cell pixel the J-V characteristics were measured before and after adding the light trapping layers in order to determine its effect on the performance of the photovoltaic device.
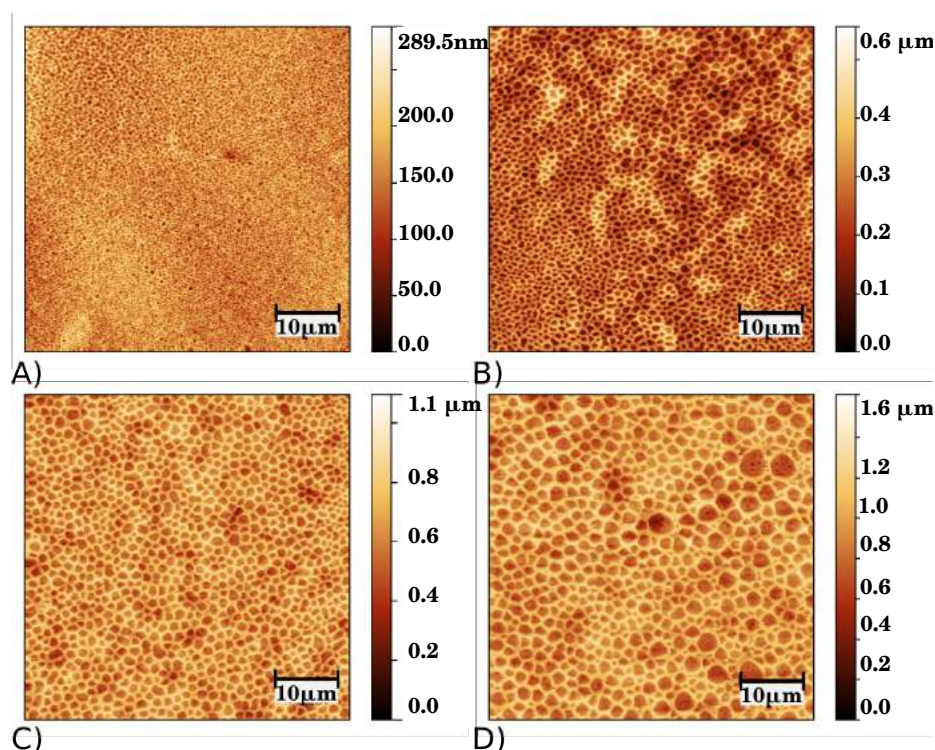
Figure 5.29: AFM images of breath figure patterns prepared under different relative humidity conditions A) 5% RH, B) 45% RH, C) 70% RH, D) 82% RH. The structures were prepared by spin coating (1000 rpm) of PMMA in THF mixed with 5% of water (total polymer concentration 60 mg/ml).

Results and discussion

Breath figure formation   At the beginning we were interested how adding the water into the solution influences the porous structures prepared under high humidity and how these structures differ from the ones prepared without additional water. The similar experiments were conducted by Madej et al. [96], which obtained the pores differing in diameters from 0.13 μm to 0.84 μm. However, the authors did not investigate the changes in porous depth which is an important parameter in the context of light scattering, as was presented in Figure 5.24.

Figure 5.29 shows AFM images of PMMA films prepared by spin coating (1000 rpm) of PMMA solution in THF (60 mg/ml) containing 5% water under relative humidity (RH) between 5% and 90%. If we compare these images with results discussed in the previous section (see Figure 5.18) we see the visible differences in shapes and dimensions. Under low humidity (RH = 5%, Figure 5.29 A), PMMA films exhibit disordered porous structures with surface roughness value of 12 nm. With increasing humidity irregular holes become separated by narrow walls (Figure 5.29 B–D). The depth of the holes changes from 100 nm to 400 nm and the area of the holes increases
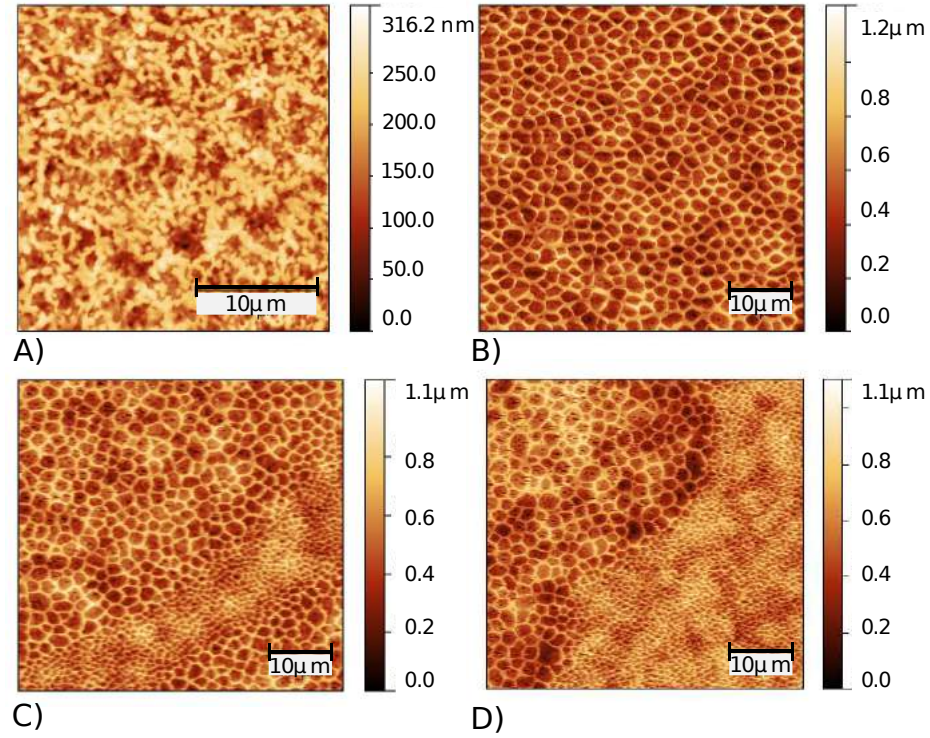
Figure 5.30: AFM images of breath figure patterns prepared by spin coating (1000 rpm) under low humidity (40% RH) from 60 mg/ml PMMA solutions with: A) 3%, B) 4%, C) 5%, D) 7% of water.

from 0.4 to 1.4 μm^2. If the holes are approximated as disks, their average diameter changes from 0.70 μm (45 % RH) to 1.34 μm (82% RH). Here we obtained holes with a wider range of sizes and depths, compared to the previous structures prepared under high humidity without additional water in the solution (Figure 5.23).

Our results are consistent with the results obtained by Madej et al. [96], even though they used PMMA with significantly lower molecular weight. In contrast to previous studies on star– and block–copolymers [178, 179] we did not observe any significant impact of the molecular weight on the pore size. Additionally, for higher humidity (RH > 55%) we observed the creation of smaller holes in the bottom of the large holes. Such structures were previously reported for breath figure layers formed from poly(3–hydroxyburate) [180], polyphenylene oxide [181], and the block copolymer PMMA–co–HEMAGI [182] and suggest the presence of additional structures below the surface.

Another method to control the size of the pores was proposed by Park et al. [97], where the authors changed the amount of water in the polymer solution. This approach seems to be more suitable for fabrication of light trapping layers on organic solar cells as porous structures can be formed in a dry atmosphere reducing the risk for OPV degradation. As Figure 5.29B shows, by adding 5% of water into the solution
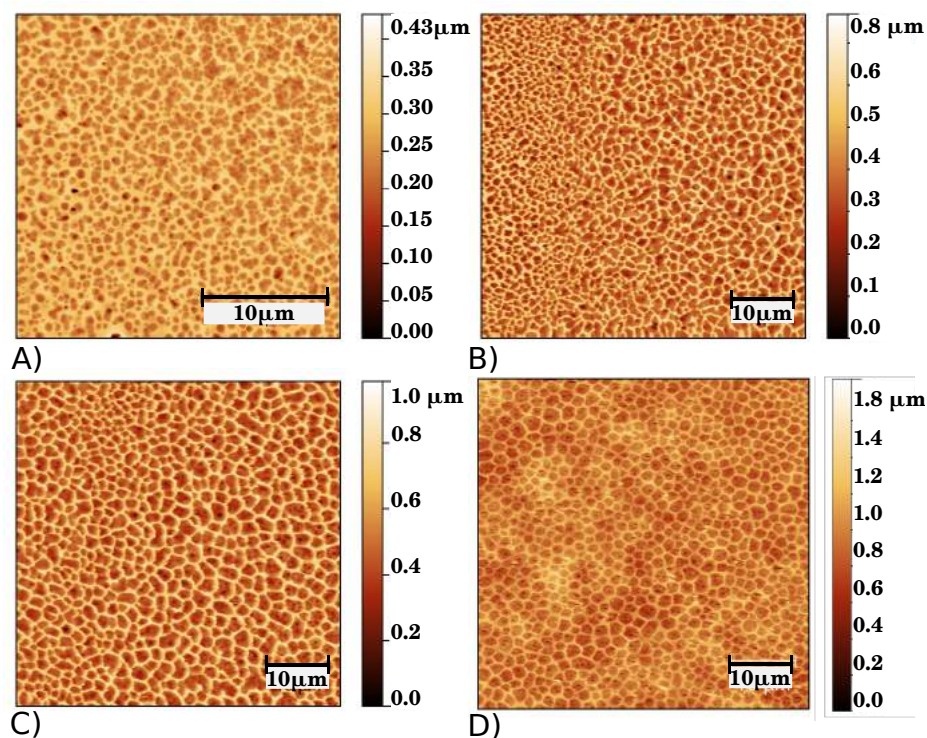
Figure 5.31: AFM images of breath figure patterns prepared by spin coating (1000 rpm) under low humidity (40% RH) from 100 mg/ml PMMA solutions with: A) 3%, B) 4%, C) 5%, D) 7% of water.

we can form breath figure structures even under low humidity (RH = 45%).

Below we present results for two different polymer concentrations: 60 mg/ml and 100 mg/ml. Figures 5.30 and 5.31 show that the size of the breath figures increases with the water content for solutions cast under ambient conditions (RH = 40%). Unfortunately, the monotonic growth of pores collapses in films cast from solutions with polymer concentrations of 60 mg/ml and water content higher than 4%. In this case domains with large and small pores are visible at the surface of polymer films and the area covered by the latter increases with the water content (see Figure 5.30C and D). Formation of multi–scale breath figure structures in films cast from solutions with 60 mg/ml of polymer (Figure 5.30) results in a decrease of the average pore area and depth calculated for samples with higher amounts of water. Such trend is not observed in the case of films cast from solutions with total polymer concentration of 100 mg/ml, as seen in Figure 5.31. In the subsequent analysis we focused only on structures prepared from 100 mg/ml solution and not 60 mg/ml.

If we look back at structures prepared under different relative humidity (Figure 5.29) and with different amounts of water in the PMMA solution (Figure 5.31) we see that they seem to be similar. To quantitatively compare these porous structures we used the grain analysis [112] approach. In parallel to the calculation of the
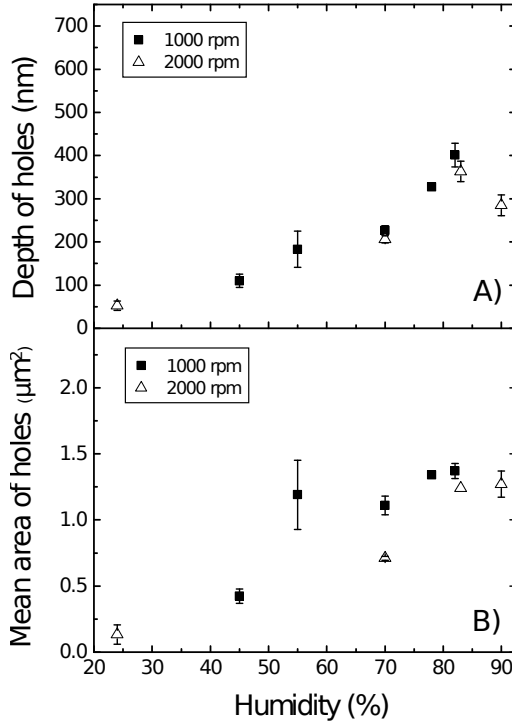
Figure 5.32: Mean depth (A) and area (B) of holes plotted against relative humidity for two rotating speeds 1000 rpm and 2000 rpm.
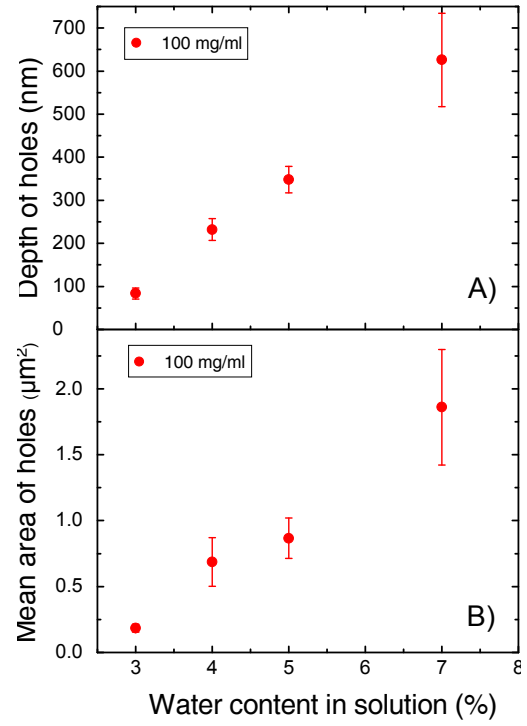
Figure 5.33: Mean depth (A) and area (B) of holes versus water content in solution of PMMA for concentrations 100mg/ml prepared under low humidity (RH = 40%).

mean pore area, we also estimated their depth, which was not studied earlier. The latter parameter plays an important role for light trapping as it can influence the way light spreads [177]. A deeper hole is more concave (Figure 5.28B) so the light is more divergent at the air/PMMA interface, which leads to a longer light path in the active layer. Figure 5.32 shows a monotonic increase in the depth and pore area with increasing humidity for two spin coating speeds 1000 rpm and 2000 rpm. A slight decrease in the mean pore area for higher rotation speed visible in Figure 5.32B is in accordance with previous reports [97]. Figures 5.32A show that the depth of the pores increases with the relative humidity and in contrast to the mean area the depth is almost independent of the rotation speed. The area of the largest pores achieved this way was less than 1.5 μm^2 and the depth ca. 400 nm. We also observed a monotonic increase in the depth (Figure 5.33 A) and area (Figure 5.33 B) of the structures presented in Figure 5.31. Both measures grow linearly with the amount of water added to the solution with polymer content 100 mg/ml.

The results presented in Figures 5.32 and 5.33 demonstrate that by changing the water content in the solution we were able to create a wider range of hole geometries than by changing the humidity. In further analysis of the influence of breath figures
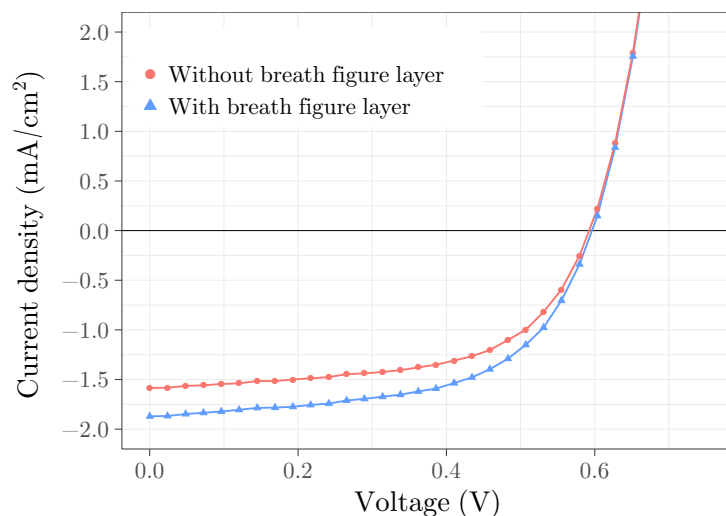
Figure 5.34: Representative J-V characteristics of P3HT:PC$_{60}$BM solar cell without and with light trapping structures

on the performance of OPVs we used light trapping layers cast from solutions with 100 mg/ml of polymer and various amounts of water. For these conditions, the pore area varies from 0.2 to 1.8 μm^2 (corresponding diameters range 0.5 – 1.5 μm) and the depth from 85 to 700 nm.

Solar cells with light trapping structures   In order to evaluate the effect of porous structures on the performance of organic solar cells we prepared the light trapping layer on the top of the cells (Figure 5.28A). The geometry of the device consisted of the following layers: light trapping layer, glass, transparent electrode (ITO), buffor layer (PEDOT:PSS), active layer (P3HT:PC$_{60}$BM) and electrode (Al). The advantage of the external trapping layer is that the influence of the breath figure structures on the cell performance could be measured directly. First we measured the current-voltage characteristics of the cell without any light trapping layers, then the breath figure structures were fabricated on the front size of the glass and the measurement was repeated. Figure 5.34 gives an example of the current-voltage (J-V) characteristics of a solar cell with and without porous structures under 500 W/m^2 illumination.

   To investigate the influence of the breath figures size on the solar cell performance, we exploited the linear relation between the amount of water in the PMMA solution and the pore size, presented in Figure 5.33. As in experiments we previously described, by changing the amount of water in the solution we obtained holes of varying depth and area. Figure 5.35 presents the relative changes in short circuit current density ($\Delta\, j_{sc}$) as a function of water content in the PMMA solution. Short-circuit current density j_{sc} displays two regimes depending on the water content: it increases at lower water content but drops even below the initial performance at higher water content.

Before we discuss the morphology of these two regimes in detail, let us look at the leftmost point in Figure 5.35, corresponding to 0% of water content. This OPV was covered with a uniform PMMA film, without any breath figure structures. By comparing the results before and after PMMA fabrication we see that the j_{sc} slightly decreased around $1.7 \pm 0.6\%$. This decrease of j_{sc} could be attributed either to OPVs degradation or to imperfect transimttance of the PMMA film.

Moving further on to water content of the order 3–5%, we see a slight increase in j_{sc} by roughly 5–7%. The breath figures arising for this water content are roughly 0.5–1.5 μm in diameter and 0.085–0.350 μm deep. These sizes correspond to the region in Figure 5.24 representing the largest values of scattering angles.

We would like to point out that the relationship of the hole sizes with the simulated scattering angle is rather weak. The simulation assumed spherical structures of uniform sizes and distributions, while in the experiments we observed a large variety of sizes within a single sample and the placement of the depressions is far from uniform. Nevertheless, the simulations give us a rough idea about the structure sizes we should aim for to get large scattering angles and transmittance. This lack of relation to the simulations is further demonstrated with the j_{sc} degrading for structures of diameter 1.5 μm and 0.6 μm, for which the scattering angle should be still at 10% and similar to the smaller structures.

Based on AFM data, holes with depth above 600 nm and mean diameter larger than 1.6 μm have a negative influence on the performance of the solar cell; an improvement was only achieved when the depth of holes was between 85 and 350 nm and their area was below 1.1 μm. The presented optimal structures are much smaller than those reported by Cho et al. [154].

Conclusions

We demonstrated that breath figure structures, as external light trapping layers, can increase the current density by around 5 to 6%. To achieve this the diameter and depth of the pores needs to be optimized and should not exceed 1.6 μm and 600 nm, respectively. The largest improvement was achieved with pore depths between 85 and 350 nm and diameters below 1.1 μm. This increase in performance could be explained by the large scattering angles observed in simulations. However, the relation of the simulation results to our experiments is relatively weak. This is likely due to a large variety of breath figure structures present within each experimental sample, while simulations were conducted for an idealized layer where all holes were of the same dimensions. On top of that, the simulations assumed the hole packing was strictly hexagonal, which was not the case for the experimental samples.

One way to improve the simulations would be to take into account nonuniform structures that we obtained in our experiments. It would also be interesting to recreate the uniform structures from the simulations experimentally to see how they actually perform. In the end, we believe that there is a potential for further improving the

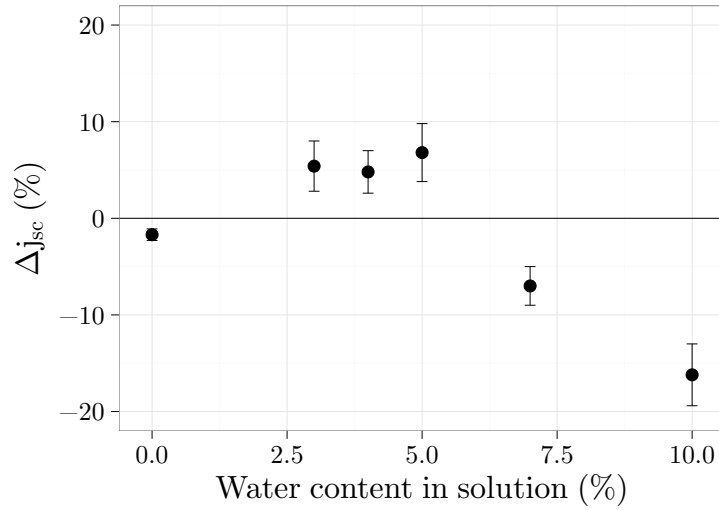Figure 5.35: Influence of breath figures A) diameter and B) depth on the changes in short current density. The variation in structures' sizes was achieved by varying the amount of water in PMMA solution.
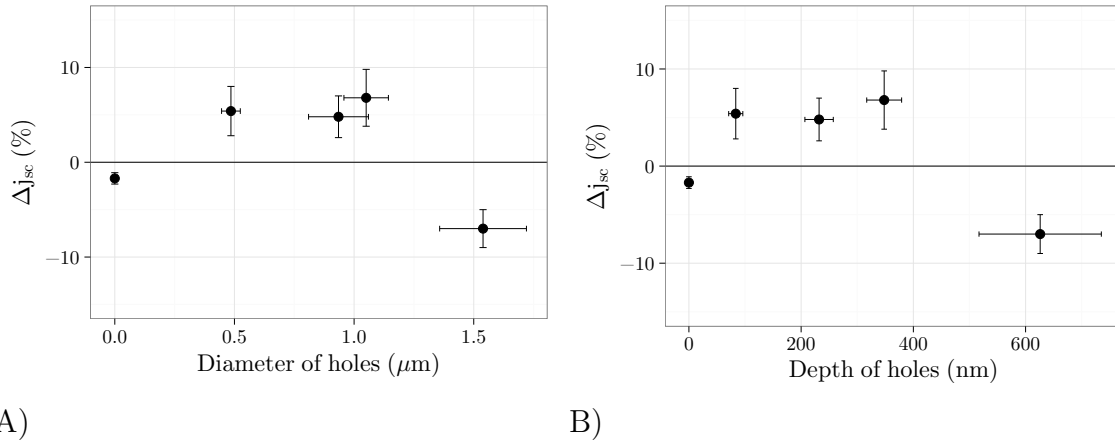

A)   B)

Figure 5.36: The changes in short–current density Δj_{sc} due to the presence of breath figures attached on the top of organic solar cells.

Water content	J_{sc} (mA/cm^2)	V_{oc} (V)	FF (%)	PCE (%)	ΔJ_{sc} (%)	ΔPCE (%)
Ref.	1.85 ±0.09	0.58 ±0.01	58.1 ±1.1	1.25 ±0.07		
3%	1.95 ±0.09	0.58 ±0.01	57.1 ±1.0	1.29 ±0.06	5.4	3.2
Ref.	1.81 ±0.06	0.57 ±0.01	59.5 ±0.3	1.23 ±0.04		
4%	1.90 ±0.06	0.57 ±0.01	58.1 ±0.2	1.26 ±0.05	5.0	2.5
Ref.	1.79 ±0.06	0.51 ±0.01	54.9 ±0.9	1.00 ±0.06		
5%	1.90 ±0.04	0.50 ±0.01	54.9 ±0.9	1.04 ±0.06	6.1	4.1
Ref.	1.70 ±0.05	0.50 ±0.01	53.6 ±0.9	0.91 ±0.08		
7%	1.58 ±0.03	0.49 ±0.01	53.7 ±0.9	0.84 ±0.06	-7.1	-8.7
Ref.	3.22 ±0.09	0.49 ±0.01	42.5±0.9	0.67 ±0.02		
10% (*)	2.70 ±0.08	0.48 ±0.01	40.6 ±0.9	0.53 ±0.03	-16.1	-21.5

Table 5.3: Performance parameter of organic solar cells without (Ref.) and with breath figure structures. The devices were prepared under ambient atmosphere using different amounts of water in the PMMA solution (3%, 4%, 5%, 7%, 10%). The J-V characteristics were measured under irradiance of 500 W/m^2 (for 10% amount of water under irradiance of 1000 W/m^2 (*)). The relative increase/decrease as a consequence of the added breath figure is given.

OPV performance with breath figure structures, as in the simulations we definitely see areas with large scattering angles.

5.2.3   Breath figure with depth and diameter gradients

In the previous sections we examined breath figures prepared by spin–coating techniques. We showed that by changing solution concentration, amount of water in the solution, relative humidity it is possible to vary the scale of the structures [95, 170]. Although spin–coating is a versatile technique widely used in laboratories it is labor intensive and inextensible to industrial scales. In this section we investigate an alternative technique called horizontal–dipping which can be described as a combination of dip–coating and blade–casting. All of these techniques have so far enjoyed relatively little attention in context of breath figure preparation [25].

Dip–coating and blade–casting are very similar to techniques used for large–scale printing. In dip–coating a substrate is firstly soaked in a polymer solution and then raised vertically with a certain speed. In blade–casting a blade scrapes the solution over a substrate. Horizontal–dipping (H–dipping for short) combines both of these ideas: the substrate is placed horizontally and a small cylinder wetted with the polymer solution slides along its surface hovering slightly above it, the polymer is deposited on the substrate in a form of a thin layer with its properties depending on the speed of the movement. By changing the coating conditions we can manipulate the thickness and morphology of the film.

As for the dip–coating and blade–casting there are a few existing results. Hiwatari et al. [183] used dip–coating to prepare highly ordered breath figure structures from graft copolymer and chloroform solution. They observed that morphology of macropores is similar to that obtained by solvent–casting methods. Recently Mansouri et al. [184] also presented isoporous polysulfone membranes combining the dip–coating and breath figures technology. However, to our knowledge, the H–dipping has never been studied in context of breath figures.

In this section we present the first of a kind study on H–dipping [86, 89, 185] for breath figures preparation. This method allows to prepare not only the thin layer with the constant thickness but also with gradient one, which is the main advantage: the thickness gradients of the layers coming from H–dipping provides a rich sample of different breath figures from a single experiment.

Our attention was focused not only on the preparation and morphology examination of breath figure structures but also on their practical applications as the light trapping layers. The best breath figures, in sense of their optical properties, were replicated by elastomeric stamps used in soft lithography. In this way we were able to transfer an optimal light trapping structures onto organic photovoltaics and check their influence on the devices performance.

Experimental

Sample preparation: Poly–(methylmethacrylate) PMMA, $M_W = 65\ 000$, was dissolved in tetrahydrofuran (THF) with total concentration 60 mg/ml and next different amount of water 5%, 8% and 10% was added into the solutions. Polymer gradient

layers were prepared by H–dipping using a home–build system [90]. A drop of solution was placed near the microscope slides edge, between the glass substrate and the glass bar (Figure 5.37). Than the substrate was set in motion by a computer-controlled linear stage (Newport UTS100) with constant acceleration a = 1 mm/s^2. During this process the gradient breath figure pattern was formed. To estimate solution drawing velocity (v) we measured the distance between initial and final positions (s) and used the relation: $v = \sqrt{2 \cdot s \cdot a}$.

Soft lithography: The patterned structures on the PDMS stamp were obtained by pouring of PDMS prepolymer (Sylgard 184) and curing agent with a ration 10:1 directly on the previously prepared breath figures films. The mixture was cured in an oven at 70°C for 1 h. After this time the stamp was peeled off from the breath figure substrate and ready to use. Then we transferred the breath figure pattern from the PDMS stamp into the front side the organic solar cells with microtransfer molding. The microtransfer molding was performed with a drop of polymer solution (PMMA M_W = 65 000 dissolved in toluene with total concentration 15 mg/ml) being placed directly into a patterned PDMS stamp and then the stamp being brought into the contact with the substrate and press until solvent evaporates.

Organic solar cells: OPV devices based on heterostructure of poly 3–hexylthiophene (P3HT) and [6,6]-Phenyl-C61-butyric acid methyl ester (PC$_{60}$BM) were prepared using the same procedure as described in Experimental Section 3.3. ITO substrates (with 6 pixels) were cleaned by acetone and isopropanol, dried with nitrogen and than treated with oxygen plasma for 20 s. A PEDOT:PSS was spin–coated at 4000 rpm for 30 s and than annealed at 120°C for 20 min on a hotplate. P3HT and PC$_{60}$BM dissolved in chlorobenzene in a vol. ration 1 to 0.6 was spin-coated at 2500 rpm for 30 s in a glove-box. After that an aluminum electrode was thermally deposited on the top of the active layer. At the end all devices were annealed at 150°C for 15 min and encapsulated using the curable epoxy.

Characterization: The surfaces of the gradient samples were characterized by atomic force microscope in contact mode. Topographic images were analyzed with Gwyddion software using Grain analysis [112]. Images of macroscopic breath figures structures were taken through an optical microscope (Olympus BX series) and were analyzed within integral geometry approach [186].

Results and discussion

Our first task was to prepare the breath figures of varying dimensions using H–dipping methods. The procedure is schematically presented in Figure 5.37. Like in dip–coating a wet layer of dissolved material is formed by withdrawing a substrate under a meniscus of the coating solution. On the other hand, as in blade–casting, the substrate is drawn horizontally and the meniscus is kept at a constant height during

Figure 5.37: Schematic presentation of H-dipping process. A drop of solution is placed between the bar and the substrate. The substrate is moved either with constant velocity or with constant acceleration resulting the fixed or thickness gradients layer.
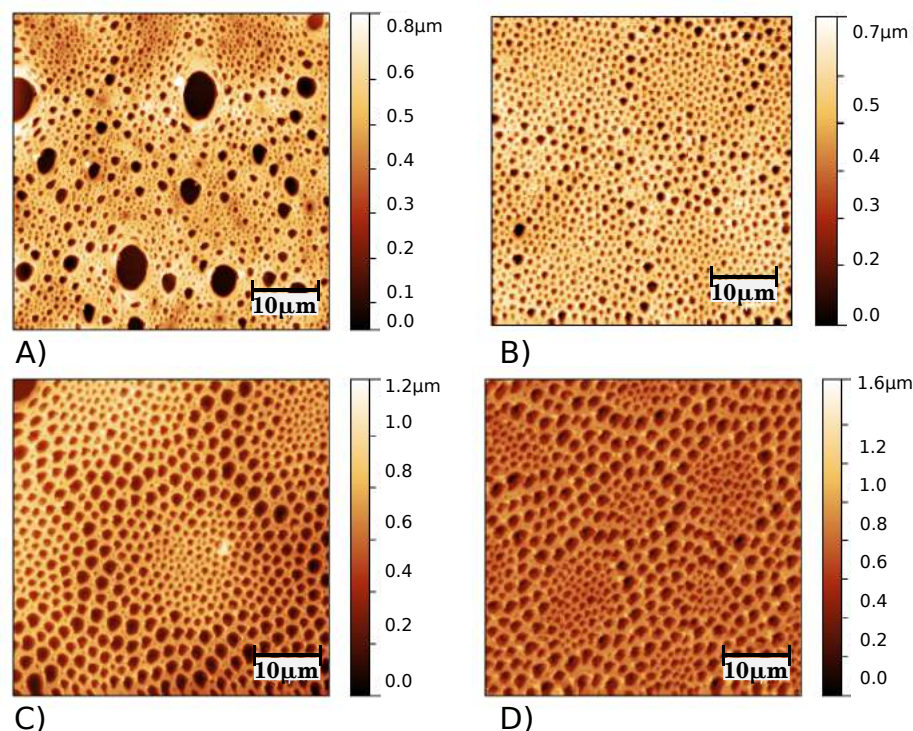
Figure 5.38: AFM images of breath figure patterns prepared from PMMA solutions with 5% of water using h-dipping. The recorder position corresponding with local velocity values of: A) 4.5 mm/s, B) 6.3 mm/s, C) 8.4 mm/s, D) 10.5 mm/s.

the substrate movement. At the beginning we examined the structures prepared from the solution of PMMA in THF containing 5% water. A small amount of solution was placed between the cylindrical bar and the glass substrate, which was then set in motion with constant acceleration 1 mm/s^2. The resulting structures with thickness gradients are presented in Figure 5.38. The first centimeter of the sample, which correspond to the the local velocity 4.5 mm/s, is illustrated in Figure 5.38A. In this region the breath figures are inhomogeneous with distinguishable large holes. With an increasing velocity the pattern becomes more regular, for higher velocity above

Table 5.4: Probabilities (P_i) of pores with i nearest neighbors and the conformation entropy of hole prepared under different humidity.

velocity (mm/s)	P4	P5	P6	P7	P8	S
4.5	0.08	0.31	0.35	0.17	0.07	1.58
6.3	0.06	0.27	0.39	0.22	0.05	1.42
8.4	0.06	0.27	0.41	0.21	0.04	1.42
10.5	0.06	0.27	0.42	0.19	0.05	1.43
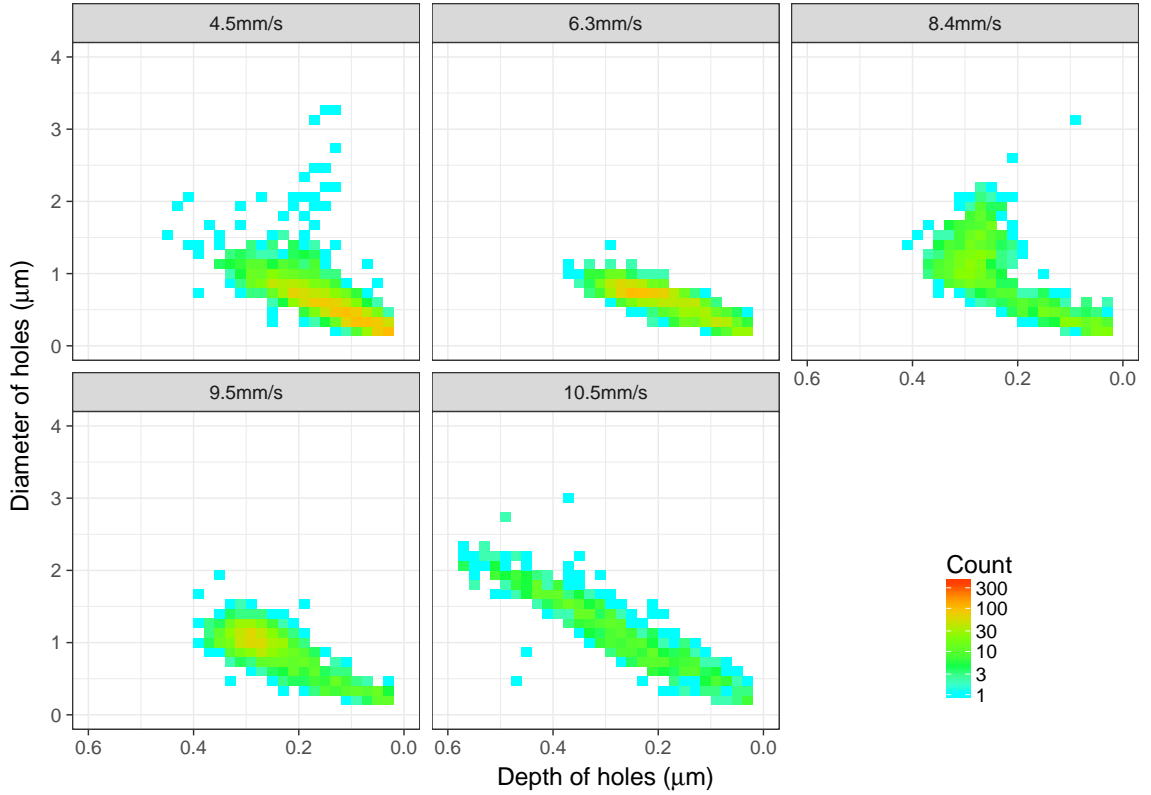
Figure 5.39: 2D map representing the distribution of holes depth and diameter with marked on the corresponding local velocity values.

8 mm/s the breath figure structures arrange in the visible clusters.

To evaluate the degree order of breath figure packing we used the Voronoi polygon construction [187]. A Voronoi polygon is the smallest convex polygon surrounding a point whose sides are perpendicular bisectors of lines between a point and its neighbors. To obtain the order parameter from the Voronoi polygon construction we first determine the probabilities P_i of the pores being formed with i nearest neighbors. Than the confirmation entropy of breath figures is calculated: $S = -\sum P_n \ln P_n$.

Table 5.4 summarizes the probabilities P_i of the pores with i nearest neighbors

A)   B)

Figure 5.40: Holes median values of diameters A) and depth B) with marked 1st – 3rd quantile.

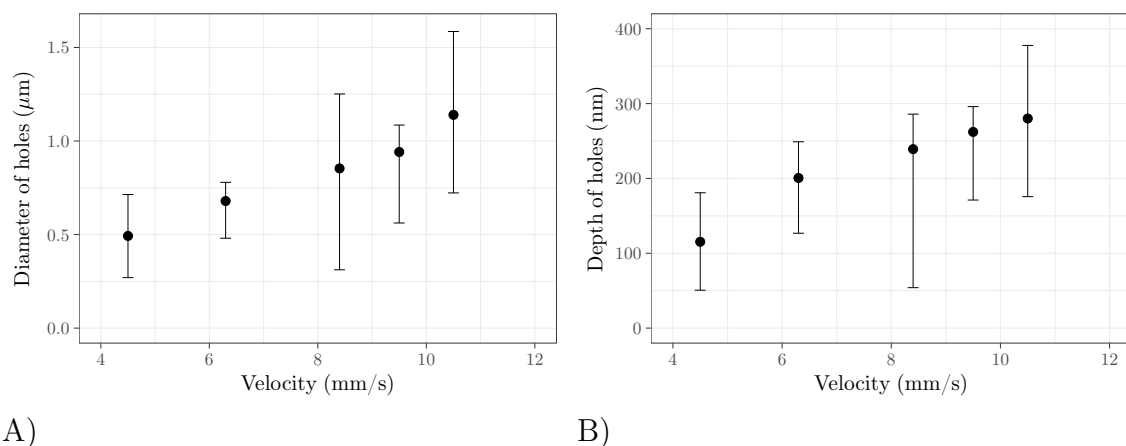for the different positions on the samples (Figure 5.38). The values in Table 5.4 show the highest probabilities for the pores having six nearest neighbors. However, the difference between six and five neighbors is rather small. The highest conformation entropy S = 1.58 was obtained for the smallest velocity. This value is close to the 1.71, which correspond to the randomly distributed pores [173]. For higher velocity the entropy slightly decrease to value 1.42 - 1.43, however it is still close to the randomly packed pores. Based on the Voronoi diagram analysis we concluded that the obtained patterns are not highly ordered.

To quantitatively describe the porous structures we used grain analysis [112]. As in the previous section, we constructed 2D maps depicting distributions of depth and diameter, based on the AFM images (Figure 5.38). As can be seen in Figure 5.39 for each velocity the shape of distribution differs. The top left pictures correspond to the start of the sample where the local velocity of the substrate amounted 4.6 mm/s. Here, apart from holes with diameter less then 1 μm, additional singular large holes are visible. For 6.3 mm/s and 9.5 mm/s the distributions are more concentrated. In case of 8.4 mm/s we observed bimodal structures, whereas for 10.5 mm/s the distribution is narrow but longitudinal. To better see how distributions change with increasing velocity of samples during breath figure formation we calculated median values of depth and diameter. The results are presented in Figure 5.40 with additional marked 1st to 3rd quantile. As can be seen, with increasing velocity the hole depth also increases in a non-linear way starting from 115 nm at the beginning of the sample and ending up at 280 nm at the end of it. Also the diameter of the holes varies with the velocity from 0.5 μm to 1.2 μm.

It is worth to emphasize that H–dipping led to holes of similar areas as in our previous experiments (see Figure 5.32 and 5.33 in the Section 5.2.2) in which the breath figures were prepared in high humidity atmosphere or by adding small amounts of water into the solution. However, compared to the previous experiments the holes
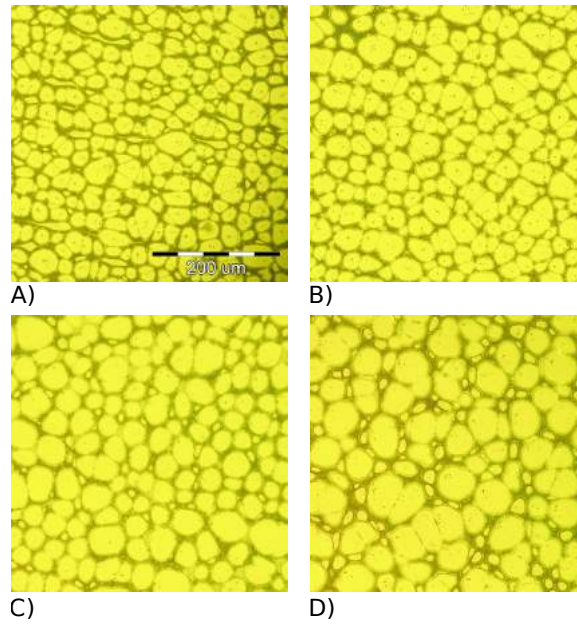
Figure 5.41: Optical micrographs illustrating the holes deposited on microscope glass with acceleration 1 mm/s² from PMMA solutions with 10% of water. Recorded positions correspond to local velocity of: A) 4.5 mm/s, B) 6.3 mm/s, C) 8.9 mm/s, D) 10 mm/s.
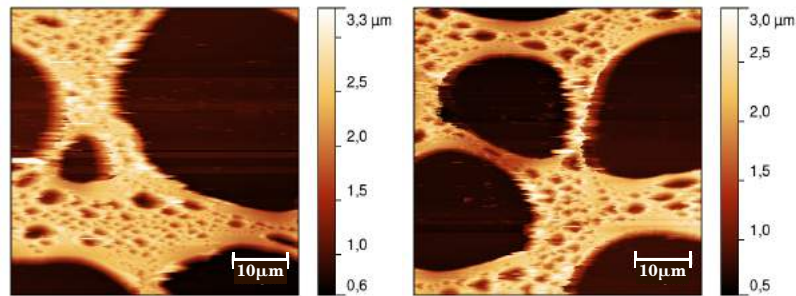
Figure 5.42: AFM images of breath figure patterns obtained from PMMA solutions with 10% of water. The A) image presents the beginning of the sample (4.5 mm/s), the B) the end of the sample (11.8 mm/s)

presented in Figure 5.40 are shallower.

The second type of structures were prepared using higher amount of water. After adding 10% water into the solution PMMA in THF the macroscopic structures became visible through optical microscope (Figure 5.43). The pattern resembled a random lattice structure rather then spherical holes.

Each optical image was threasholded into black–and–white and characterized by three morphological measures provided by the Minkowski functionals: the covered area
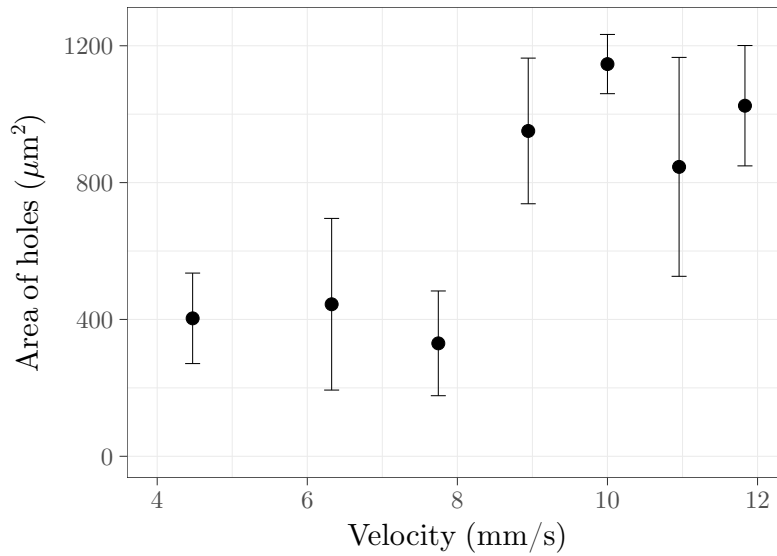
Figure 5.43: Mean area of breath figures structures prepared by adding 10% of water into the PMMA solutions. The values were calculated based on optical pictures by using Minkowski functionals.

F, the boundary length U, and the Euler characteristic χ, defined as the difference between the number of separated white and black features. We used the Minkowski measure as a base to calculate the average area $S = \frac{F}{\chi}$ of breath figures. Figure 5.42 presents the calculated mean area of holes, for velocities smaller then 8 mm/s the size of the structures is about 400 μm^2, for higher velocities the bigger structures are obtained form 900 to 1200 μm^2. Compared to previous results for structures with 5% of water, here the relation between shapes and velocity has a more discreet character.

Due to large differences in heights and a macroscopic character of the holes we were unable to examine the topography of structures using the AFM microscopy apart from a single case presented in Figure 5.42. In this picture we can clearly see small hierarchical structures inside a larger hole. Based on cross–section topography we estimated the thickness of the layers to be 1410 ±140 nm at the edge of the sample and 1461 ± 131 nm in the center.

Optical properties of the structures   To explore the optical properties of breath figures prepared with h–dipping method we measured the light reflection. As it is shown in Figure 5.44 breath figures prepared from both polymer solution (containing 5% and 10% of water) decrease the reflection of the light when compared to a bare glass substrate. The better performance in sense of antireflection layer presents the layer with micrometer structures (Figure 5.38). This improvement is even better then the one obtained through breath figures prepared in a high humidity environment (see Section 5.2.1). On the other hand, for the gradient sample we did not observe any

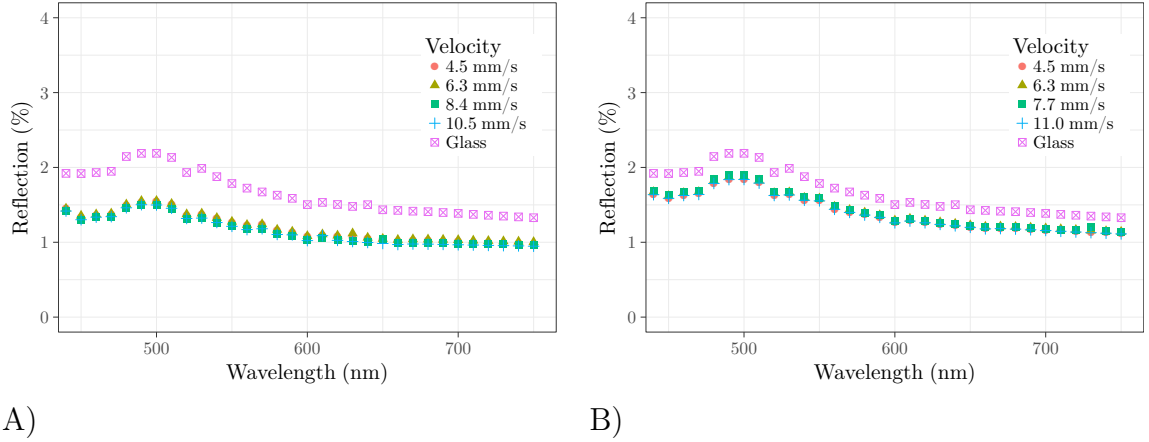A)   B)

Figure 5.44: Reflection measurement for the breath figures structures with thickness gradients prepared from 60 mg/ml PMMA solutions with A) 5% of water, B) 10% of water

visible relation between the reflection and the depth or area of the breath figures. The same applies also to the macroscopic structures.

As in our previous experiments (Section 5.2.1) for h–dipping we observed a wide distribution of shapes which makes it difficult to directly compare our optical measurements with simulations presented in Figure 2.10. However, if we restrict ourselves to the median values and map them to simulation results we see that for all cases the transmission should slightly increase. Compared to bare glass, for which the transmission amounts 0.949, the glass with breath figures has the transmission ranging from 0.957 (for pores prepared under 10.5 mm/s) to 0.972 (for 6.3 mm/s).

The main limitation of presented experiment was the lack of an integrating sphere during reflection measurements. Our system detected only the specular reflection but not the diffusive reflection. However, as reported by Ji et al. [188] the specular reflection is not dominant in a random arrangement of structures. In [188] they observed a decline in transmission in the short wavelength due to diffusive reflection for particles with 200 nm diameter and height about 350 nm. Despite these results in future research it would be desirable to use an integrating sphere to get complex information about the reflective light.

Soft lithography and organic solar cells As we showed in Section 5.2.2 the breath figure structures can improve the performance of solar cells. However, preparing the breath figures via various type of coating techniques has several drawbacks. Firstly, the reproducibility of breath figures is rather low due to their high sensitivity to external conditions like temperature, humidity. Secondly, the breath figures prepared with spin-coating, can only cover a small area of the devices. The most effective approach to overcome these obstacles is to use soft lithography, strictly speaking to use the breath figures as a master for a PDMS stamp which allows to repeatably

reproduce the pattern.

In the last decade this approach was successfully presented by several groups. To the author's knowledge the Yabu and Shimomura [102] were the first to demonstrate that breath figures can be used as a templates for the fabrication of PDMS spherical microlenses. Also Connal and Quia [189] successfully obtained negative images of honeycomb structures via replica molding technique. Since then several groups have reported variety of structures prepared with replica molding of breath figures templates [190, 191]. Moreover, Galeotti et al. [55, 192] have shown that the elastomeric PDMS layer with structures negative to breath figure patterns placed on the a flat glass surface not only improve the transmission of the light and but also enhance the light extraction from the organic light-emitting diodes (OLED) [193].

Inspired by the above results we have gone a step further. We used the PDMS stamp and by microtransfer molding we replicated the breath figures onto the organic solar cells. The procedure was the following. We started with breath figure layer prepared by h–dipping (Figure 5.45A). Than the liquid PDMS was poured on top of the structures and placed into an oven. After an hour the PDMS was pealed off resulting in negative of the structures on the top of the stamp (Figure 5.45B). At the end this stamp was used for microtransfer molding. The small amount of polymer solution was placed on the top of the stamp and then the stamp was gently pressed onto the substrate. After a while a breath figure pattern emerged (Figure 5.45C). The dimensions of the final structures were compatible with the original matrix but the holes turned out to be slightly shallower.

Using this method we showed that it is possible to transfer the whole pattern previously prepared on the microscope slide (76 x 26 mm). In the next part of experiment, however, we restricted ourselves to the end part of the stamps due to small size of the tested solar cells (20 x 15 mm). We chose this part of the sample based on our previous observation which showed that the highest increase in short-current density was obtained for breath figure with diameter around 1 μm (Figure 5.36 in the previous section). As can be seen in Figure 5.40 in the second part of the sample, where the velocity during h–dipping exceeded 8 mm/s, the structures diameter is around 1 μm.

In the future it would be worth to take a full advantage of a larger stamp. In the context of the tested organic solar cell it would require to enlarge OPV devices and replace the layer preparation technique from spin–coating to printing or h–dipping. This modification, however, was not a part of the presented work. Here, we focused mainly on checking whether it is possible to transfer patterns on the OPV and, if yes, we tried to answer how they influence the devices performance.

We were also interested whether we will observe the similar changes in short–current density as was presented in the previous section. To test that we perpetuated through two PDMS stamps the breath figure patterns prepared from PMMA solution containing 5% and 8% of water. Based on AFM images, the structures on the first stamp were in range 1.10 - 1.22 μm large and 110 - 140 nm deep, whereas in the second stamp the structures have diameter between 1.50 – 1.75 μm and depth 130 –
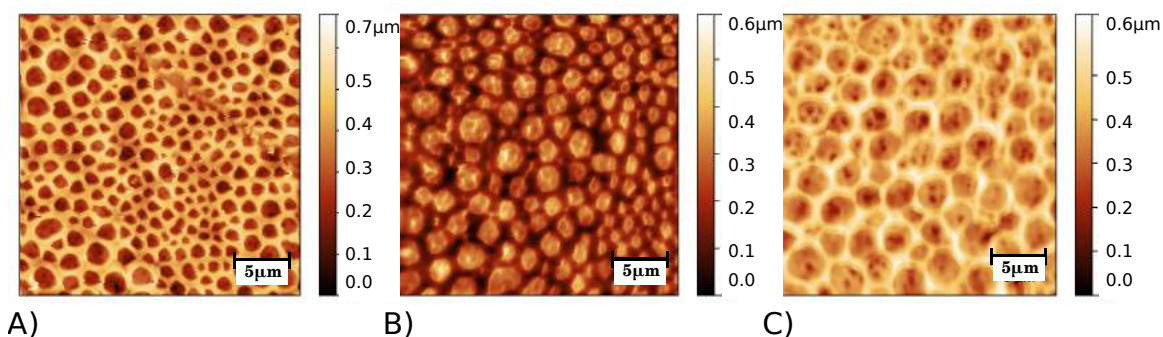
Figure 5.45: Three steps of soft lithography. A) presents the breath figure as a master, B) the resulted PDMS stamp and C) the final imprinted pattern.
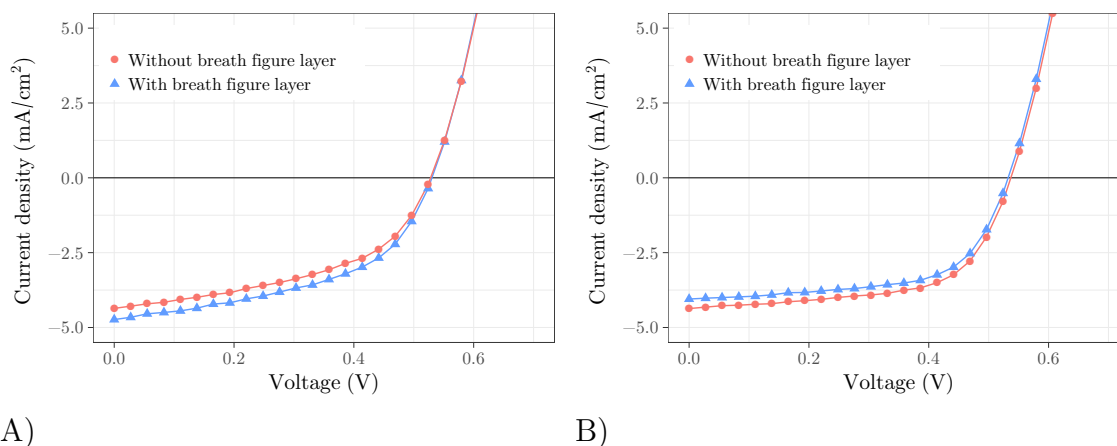
Figure 5.46: J-V characteristics of P3HT:PC$_{60}$BM solar cell without and with light trapping structures prepared by soft lithography using stamps with different pores dimensions. Structures correspond to the breath figure pattern prepared from PMMA solution with additional A) 5% of water and B) 8% of water.

200 nm.

To investigate the influence of the breath figures on the performance of organic solar cell we again used similar methodology as in the previous Section 5.2.2. Firstly, we prepared and measured the performance of solar devices without any additional light trapping layers. Then we used soft lithography to imprint the breath figures on the same solar cells. The final geometry of the devices was as following: external light trapping layer, glass, transparent electrode (ITO), buffor layer (PEDOT:PSS), active layer (P3HT:PC$_{60}$BM) and electrode (Al).

Figure 5.46 presents an example of the current–voltage characteristics of the solar cells measured without and with porous pattern prepared using two stamps with different pores dimensions. Depending on which stamps were used we observed either an increase (Figure 5.46A) or decrease (Figure 5.46B) in short–current density. For the

Water content	J_{sc} (mA/cm^2)	V_{oc} (V)	FF (%)	PCE (%)	ΔJ_{sc} (%)	ΔPCE (%)
Ref.	4.31 ±0.19	0.52 ±0.01	51.0 ±0.9	1.14 ±0.04		
5%	4.60 ±0.08	0.52 ±0.01	51.5 ±0.9	1.25 ±0.05	6.7	9.6
Ref.	4.50 ±0.12	0.52 ±0.01	53.3 ±0.8	1.25 ±0.09		
8%	4.20 ±0.09	0.50 ±0.04	50.1 ±0.9	1.08 ±0.09	-6.6	-13.6

Table 5.5: Performance parameter of organic solar cells without (Ref.) and with breath figure structures. The pattern were prepared by soft lithography using stamps with patterns corresponding to pores obtained from PMMA solution with additional 5% and 8% of water. The J-V characteristics were measured under irradiance of 1000 W/m^2. The relative increase/decrease as a consequence of the added breath figure is given.

first set of solar cells the mean current density amounts 4.31 mA/cm^2, by applying the breath figure pattern with hole diameter 1.2 μm j_{sc} increases to 4.60 mA/cm^2. For the second set of solar cells the decrease in current density is observed from 4.50 mA/cm^2 to 4.20 mA/cm^2. In this case the mean diameter of breath figures amounts 1.6 μm. The performance parameters of the devices are summarized in Table 5.5.

If we now look back to the OPV parameter presented in the previous Section 5.2.2 in Table 5.3 we see here some similarities. In both cases either using the spin coating or soft lithography to prepare the breath figures structures we observed depending on size of structures increase or decrease in short–current density. In Figure 5.47 we depicted changes in j_{sc} depending on holes diameters and depth. In both experiments for small structures below 1.2 μm the visible improvement in short current was achieved, on the other hand the larger structures than 1.5 μm have a negative influence on the performance of the solar cells. In case of holes depth the results are less compatible therefore we can not determine the optimal holes depth.

Conclusion

In this section we presented a first of a kind procedure to produce breath figure patterns with thickness gradients using h–dipping. Our results show that combing h–dipping with the soft lithography it is possible to prepare and transfer the breath fgure structures onto solar cells in an efective way. Fabricated light trapping layers improved performance of tested devices. We observed a relative 6.7% increase in j_{sc} on average, for structures whose the diameter and depth were 1.22 μm and 127 nm on average. On top of that we observed a the noticeable decrease of -6.6% for bigger structures with diameter 1.65 μm and depth 180 nm.

As we mentioned, due to small size of our OPV devices which we analyzed, we were unable to fully exploit the potential of gradient breath figures as light trapping layers. In the future research it would be interesting to use h–dipping not only for preparation of breath figures but also to produce gradient active layers and other
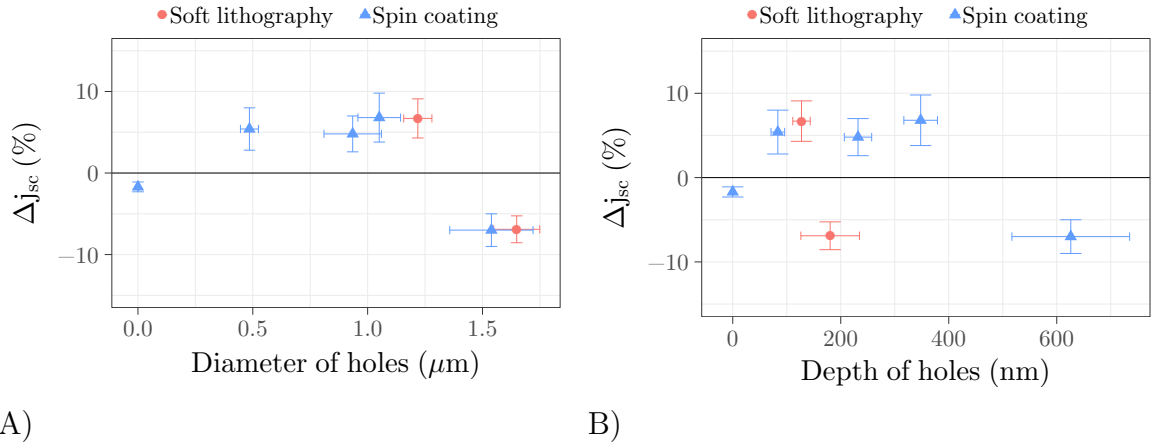
Figure 5.47: Influence of breath figures A) diameter and B) depth on the changes in short–current density j_{sc} of organic devices. Red circles correspond to results for breath figures prepared by soft-lithography (Section 5.2.3), whereas blue triangles represent structures prepared by spin–coating from PMMA solution with added water (Section 5.2.2).

parts of OPVs. Using layers with thickness gradients will enable us to find optimal parameters of such layers more efficiently leading to further improvements in OPVs performance.

Chapter 6

Conclusions

In the first part of the thesis our attention was paid to carbazole-based copolymer PCDTBT, one of the conductive polymers used as a donor material in organic solar cells. Our first aim was to experimentally determine the Flory-Huggins interaction parameters, χ, between PCDTBT and several solvents. This parameter determines compatibility of a given solvent and polymer pair. As the active layer in OPV is commonly prepared from solution and the final morphology is influenced by interaction between the solvent and polymer [22] it is important to know the value of χ for a given mixture.

We conducted a swelling experiment to determine χ between PCDTBT and four solvents: chlorobenzene, chloroform, toluene and o-dichlorobenzene. We found that chlorobenzene and chloroform are good solvents (both had χ well below 0.5 and formed homogeneous mixtures), toluene turned out to be a bad solvent (χ above 0.5), while o-dichlorobenzene was a borderline case (χ close to 0.5). To our knowledge, this is the first study reporting χ for these pairs of solvents and PCDTBT.

Next, we shifted our attention towards a ternary mixture of PCDTBT and fullerene dissolved in a common solvent. Such mixture is a popular choice to prepare the active layer in OPVs. We were interested whether it is possible to predict the final morphology of a PCDTBT:PCPBM layer based on the ternary phase diagram. Our results showed that there are incompatibilities between the final morphology and the phase diagram. We found that despite the similarities between the ternary diagrams for chloroform and chlorobenzene these two solvents had visible differences in the final layer morphology. This inconsistency may have arisen from the deficiencies of the phase diagram as a model of the layer formation: the phase diagram describes a stationary state, whereas the layer formation is a dynamic process. We believe that the dynamic (ternary) phase separation models could explain these discrepancies, this would be an interesting direction for further studies.

The second part of the thesis was dedicated to polymer light trapping layers, where

we focused on external layers that can be added on the incident side of existing OPVs. As the main mechanism of such layers is to scatter the incident light (to increase the effective light path) we studied these layers in isolation to measure that effect. We then attached the studied layers to OPVs to measure their net influence on the OPVs efficiency.

We studied two classes of light trapping layers coming from either periodic structures or random porous structures. For periodic structures we used the DVD and CD tracks transferred to a polymer layer via soft lithography. Our results showed that such structures do not improve the light absorption in polymer layer nor the efficiency of OPVs. As a side–project we re–used the soft–lithography stamps to replicate periodic structures on the active layer, where we saw some improvement in both absorption and short circuit current for the DVD stamps. As expected, such approach was technically much more challenging then adding an external absorption layer.

In our opinion a much more interesting results were obtained for porous structures based on breath figures. We first showed how the distribution of depths and diameters of the pores depends on the manufacturing parameters, which extends the existing results on breath figures. We also demonstrated the relationship between dimensions of the pores and absorption in polymer layer. The biggest improvement in absorption was obtained for the narrowest distribution of depths and diameters focusing around 0.15 μm and 0.35 μm respectively. These results were in accordance with a simulation of scattering angles performed by dr Jakub Haberko. Finally we found that external light–trapping layers based on breath figures increase the short–current density in OPVs up to 6% for structures with diameters below 1.1 μm and depths below 350 nm.

Although the results we obtained were promising, the breath figures we used were produced with a spin–casting technique which would be difficult to apply on industrial scale. We showed how this issue could be alleviated by replicating the breath figures via soft lithography instead of creating them directly on the light–trapping layer. We verified that the end results of a soft–lithography approach are comparable with spin–casting in terms of short–circuit current and the geometric structure of the pores. On top of that, we introduced horizontal–dipping as a method to create the matrix for the stamps, which turned out to be a more practical alternative to spin–casting as it allowed us to create a wide range of geometries in a single run. These geometries could be individually studied and transferred to the OPVs.

To summarize, in our research we touched a wide range of subjects related to OPVs including basic research on polymer–fulerene mixtures and novel light–trapping layers, both of which can find applications outside of OPVs. In particular, the light–trapping layers can be applied to any third–generation photovoltaic cells.

Acknowledgements

During these past years I have met many people whose experience, knowledge and support helped me in finishing this work. I would like to warmly thank to:

- dr hab. Jakub Rysz, my supervisor, for his guidance and support in field of organic electronics.

- dr Jakub Haberko and dr Paweł Biernat for numerical simulations.

- Prof. Ellen Moons for her hospitality during a month I spent with her research group in Karlstad.

- Paweł Dąbczyński, dr Mateusz Marzec and dr Rickard Hansson for sharing their experience, good advice and technical help.

- My collegues from Macromolecular Nanofilms Group for their help and creating a friendly working atmosphere.

- My family and friends, whom I could always rely on.

- Finally, to my beloved husband, for his great support and tremendous faith in me. I dedicate this thesis to him.

Bibliography

[1] K. A. Mazzio and C. K. Luscombe, "The future of organic photovoltaics.," *Chemical Society reviews*, vol. 44, pp. 78–90, jan 2015.

[2] S. Beaupré and M. Leclerc, "PCDTBT: en route for low cost plastic solar cells," *Journal of Materials Chemistry A*, vol. 1, no. 37, p. 11097, 2013.

[3] "Photovoltaics report," Tech. Rep. 6 June, Franhofer Institute for Solar Energy Systems, ISE, Freiburg, 2016.

[4] M. A. Green, K. Emery, Y. Hishikawa, W. Warta, and E. Dunlop, "Solar cell efficiency tables (version 48)," *Prog. Photovolt: Res. Appl.*, vol. 24, pp. 905–913, 2016.

[5] L. Zang, ed., *Energy Efficiency and Renewable Energy Through Nanotechnology.* Springer, 2006.

[6] J. Nelson, "Polymer:fullerene bulk heterojunction solar cells," *Materials Today*, vol. 14, pp. 462–470, oct 2011.

[7] A. C. Mayer, S. R. Scully, B. E. Hardin, M. W. Rowell, and M. D. McGehee, "Polymer-based solar cells," *Materials Today*, vol. 10, no. 11, pp. 28–33, 2007.

[8] S. Günes, H. Neugebauer, and N. S. Sariciftci, "Conjugated Polymer-Based Organic Solar Cells," *Chemical Reviews*, vol. 107, pp. 1324–1338, apr 2007.

[9] J. D. Servaites, M. A. Ratner, and T. J. Marks, "Organic solar cells: A new look at traditional models," *Energy & Environmental Science*, vol. 4, no. 11, p. 4410, 2011.

[10] W. Brütting, ed., *Physics of Organic Semiconductors.* Wiley-VCH Verlag GmbH & Co. KGaA, 2005.

[11] P. G. Nicholson and F. A. Castro, "Organic photovoltaics: principles and techniques for nanometre scale characterization," *Nanotechnology*, vol. 21, p. 492001, dec 2010.

[12] Q. D. Ou, Y. Q. Li, and J. X. Tang, "Light manipulation in organic photovoltaics," *Advanced Science*, vol. 3, no. 7, pp. 1–25, 2016.

[13] E. Bundgaard and F. C. Krebs, "Low band gap polymers for organic photovoltaics," *Solar Energy Materials and Solar Cells*, vol. 91, no. 11, pp. 954–985, 2007.

[14] L. Lu, T. Zheng, Q. Wu, A. M. Schneider, D. Zhao, and L. Yu, "Recent Advances in Bulk Heterojunction Polymer Solar Cells," *Chemical Reviews*, vol. 115, pp. 12666–12731, dec 2015.

[15] Q. Qiao and K. Iniewski, eds., *Organic Solar Cells: Materials, Devices, Interfaces, and Modeling*. CRC Press, Taylor&Francis Group, 2015.

[16] S. M. Menke and R. J. Holmes, "Exciton diffusion in organic photovoltaic cells," *Energy Environ. Sci.*, vol. 7, no. 2, pp. 499–512, 2014.

[17] G. Yu, J. Gao, J. C. Hummelen, F. Wudl, and A. J. Heeger, "Polymer Photovoltaic Cells - Enhanced Efficiencies Via a Network of Internal Donor-Acceptor Heterojunctions," *Science*, vol. 270, no. 5243, pp. 1789–1791, 1995.

[18] J. E. Slota, X. He, and W. T. Huck, "Controlling nanoscale morphology in polymer photovoltaic devices," *Nano Today*, vol. 5, pp. 231–242, jun 2010.

[19] F. Liu, Y. Gu, J. W. Jung, W. H. Jo, and T. P. Russell, "On the morphology of polymer-based photovoltaics," *Journal of Polymer Science Part B: Polymer Physics*, vol. 50, pp. 1018–1044, aug 2012.

[20] S. Kouijzer, J. J. Michels, M. van den Berg, V. S. Gevaerts, M. Turbiez, M. M. Wienk, and R. A. J. Janssen, "Predicting Morphologies of Solution Processed Polymer:Fullerene Blends," *Journal of the American Chemical Society*, vol. 135, pp. 12057–12067, aug 2013.

[21] B. Schmidt-Hansberg, M. Sanyal, and M. F. G. Klein et al., "Moving through the Phase Diagram: Morphology Formation in Solution Cast Polymer–Fullerene Blend Films for Organic Solar Cells," *ACS Nano*, vol. 5, pp. 8579–8590, nov 2011.

[22] F. Machui and C. J. Brabec, "Solubility, Miscibility, and the Impact on Solid-State Morphology," *Semiconducting Polymer Composites: Principles, Morphologies, Properties and Applications*, pp. 1–38, 2013.

[23] V. Coropceanu, J. Cornil, D. A. da Silva Filho, Y. Olivier, R. Silbey, and J.-L. Brédas, "Charge Transport in Organic Semiconductors," *Chemical Reviews*, vol. 107, pp. 926–952, apr 2007.

[24] F. C. Krebs, ed., *Stability and Degradation of Organic and Polymer Solar Cells.* Wiley-VCH Verlag GmbH & Co. KGaA, 2012.

[25] B. P. Rand and H. Richter, eds., *Organic solar cells: Fundamentals, Devices, and Upscaling.* No. 9, Taylor & Francis Group, LLC, 2014.

[26] F. Machui, M. Hösel, N. Li, and G. D. Spyropoulos et al., "Cost analysis of roll-to-roll fabricated ITO free single and tandem organic solar modules based on data from manufacture," *Energy & Environmental Science*, vol. 7, p. 2792, jun 2014.

[27] European Commission, "Report lists 14 critical mineral raw materials," Tech. Rep. June, MEMO/10/263, 2010.

[28] R. Po, C. Carbonera, A. Bernardi, F. Tinti, and N. Camaioni, "Polymer- and carbon-based electrodes for polymer solar cells: Toward low-cost, continuous fabrication over large area," *Solar Energy Materials and Solar Cells*, vol. 100, pp. 97–114, 2012.

[29] N. Espinosa, R. García-Valverde, A. Urbina, F. Lenzmann, M. Manceau, D. Angmo, and F. C. Krebs, "Life cycle assessment of ITO-free flexible polymer solar cells prepared by roll-to-roll coating and printing," *Solar Energy Materials and Solar Cells*, vol. 97, pp. 3–13, 2012.

[30] Y. Zhou, C. Fuentes-Hernandez, T. M. Khan, J.-C. Liu, J. Hsu, J. W. Shim, A. Dindar, J. P. Youngblood, R. J. Moon, and B. Kippelen, "Recyclable organic solar cells on cellulose nanocrystal substrates," *Scientific Reports*, vol. 3, pp. 24–26, 2013.

[31] C. W. Tang, "Two-layer organic photovoltaic cell," *Applied Physics Letters*, vol. 48, no. 2, pp. 183–185, 1986.

[32] J. Seok, T. J. Shin, S. Park, C. Cho, J.-Y. Lee, D. Yeol Ryu, M. H. Kim, and K. Kim, "Efficient Organic Photovoltaics Utilizing Nanoscale Heterojunctions in Sequentially Deposited Polymer/fullerene Bilayer," *Scientific Reports*, vol. 5, p. 8373, jul 2015.

[33] C. J. Brabec, S. Gowrisanker, J. J. M. Halls, D. Laird, S. Jia, and S. P. Williams, "Polymer-Fullerene Bulk-Heterojunction Solar Cells," *Advanced Materials*, vol. 22, pp. 3839–3856, sep 2010.

[34] M. T. Dang, L. Hirsch, and G. Wantz, "P3HT:PCBM, best seller in polymer photovoltaic research," *Advanced Materials*, vol. 23, no. 31, pp. 3597–3602, 2011.

[35] M. O. Reese, S. A. Gevorgyan, M. Jørgensen, and E. Bundgaard et al., "Consensus stability testing protocols for organic photovoltaic materials and devices," *Solar Energy Materials and Solar Cells*, vol. 95, pp. 1253–1267, may 2011.

[36] M. Jørgensen, K. Norrman, S. A. Gevorgyan, T. Tromholt, B. Andreasen, and F. C. Krebs, "Stability of Polymer Solar Cells," *Advanced Materials*, vol. 24, pp. 580–612, feb 2012.

[37] P. Cheng and X. Zhan, "Stability of organic solar cells: challenges and strategies," *Chem. Soc. Rev.*, vol. 45, no. 9, pp. 2544–2582, 2016.

[38] J. Yan and B. R. Saunders, "Third-generation solar cells: a review and comparison of polymer:fullerene, hybrid polymer and perovskite solar cells," *RSC Adv.*, vol. 4, no. 82, pp. 43286–43314, 2014.

[39] B. Qi and J. Wang, "Fill factor in organic solar cells.," *Physical Chemistry Chemical Physics*, vol. 15, pp. 8972–82, jun 2013.

[40] M.-H. Jao, H.-C. Liao, and W.-F. Su, "Achieving High Fill Factor for Organic Solar Cells," *J. Mater. Chem. A*, vol. 4, pp. 5784–5801, 2016.

[41] N. K. Elumalai and A. Uddin, "Open circuit voltage of organic solar cells: an in-depth review," *Energy & Environmental Science*, vol. 9, no. 2, pp. 391–410, 2016.

[42] M. Scharber, D. Mühlbacher, M. Koppe, P. Denk, C. Waldauf, a.J. Heeger, and C. Brabec, "Design Rules for Donors in Bulk-Heterojunction Solar Cells—Towards 10% Energy-Conversion Efficiency," *Advanced Materials*, vol. 18, pp. 789–794, mar 2006.

[43] X. Yang and A. Uddin, "Effect of thermal annealing on P3HT:PCBM bulk-heterojunction organic solar cells: A critical review," *Renewable and Sustainable Energy Reviews*, vol. 30, pp. 324–336, feb 2014.

[44] C. C. Chueh, M. Crump, and A. K. Y. Jen, "Optical Enhancement via Electrode Designs for High-Performance Polymer Solar Cells," *Advanced Functional Materials*, no. 26, pp. 321–340, 2015.

[45] H. G. Tompkins and E. A. Irene, eds., *Handbook of Ellipsometry.* Springer, feb 2005.

[46] S. Chattopadhyay, Y. Huang, Y. Jen, a. Ganguly, K. Chen, and L. Chen, "Anti-reflecting and photonic nanostructures," *Materials Science and Engineering: R: Reports*, vol. 69, pp. 1–35, jun 2010.

[47] H. K. Raut, V. A. Ganesh, A. S. Nair, and S. Ramakrishna, "Anti-reflective coatings: A critical, in-depth review," *Energy & Environmental Science*, vol. 4, no. 10, p. 3779, 2011.

[48] X. Li, X. Yu, and Y. Han, "Polymer thin films for antireflection coatings," *Journal of Materials Chemistry C*, vol. 1, no. 12, p. 2266, 2013.

[49] S. Walheim, J. Walheim, S., Schaffer, E., Mlynek, and U. Steiner, "Nanophase-Separated Polymer Films as High-Performance Antireflection Coatings," *Science*, vol. 283, pp. 520–522, jan 1999.

[50] M. Zhao, Z. Yang, D. Zhu, X. Jin, and D. Huang, "Influence of the fabrication technique on the porous size of the polymer nanoporous antireflection coatings," *Journal of the Optical Society of America B*, vol. 22, no. 6, p. 1330, 2005.

[51] W. Joo, M. S. Park, and J. K. Kim, "Block copolymer film with sponge-like nanoporous strucutre for antireflection coating.," *Langmuir : the ACS journal of surfaces and colloids*, vol. 22, pp. 7960–3, sep 2006.

[52] W. Lee, X. Zhang, and R. Briber, "A simple method for creating nanoporous block-copolymer thin films," *Polymer*, vol. 51, pp. 2376–2382, may 2010.

[53] X. Li, J. Gao, L. Xue, and Y. Han, "Porous Polymer Films with Gradient-Refractive-Index Structure for Broadband and Omnidirectional Antireflection Coatings," *Advanced Functional Materials*, vol. 20, pp. 259–265, jan 2010.

[54] M. S. Park and J. K. Kim, "Broad-band antireflection coating at near-infrared wavelengths by a breath figure.," *Langmuir : the ACS journal of surfaces and colloids*, vol. 21, pp. 11404–8, nov 2005.

[55] F. Galeotti, F. Trespidi, G. Timo, and M. Pasini, "Broadband and Crack-Free Antirefl ection Coatings by Self- Assembled Moth Eye Patterns," *ACS Applied Materials & Interfaces*, vol. 6, no. 8, pp. 5827–5834, 2014.

[56] W. Luk, K. Yeung, K. Tam, K. Ng, K. Kwok, C. Kwong, A. Ng, and A. Djurišić, "Enhanced conversion efficiency of polymeric photovoltaic cell by nanostructured antireflection coating," *Organic Electronics*, vol. 12, pp. 557–561, apr 2011.

[57] J. D. Chen, L. Zhou, Q. D. Ou, Y. Q. Li, S. Shen, S. T. Lee, and J. X. Tang, "Enhanced light harvesting in organic solar cells featuring a biomimetic active layer and a self-cleaning antireflective coating," *Advanced Energy Materials*, vol. 4, no. 9, pp. 1–8, 2014.

[58] D.-H. Ko, J. R. Tumbleston, L. Zhang, S. Williams, J. M. DeSimone, R. Lopez, and E. T. Samulski, "Photonic crystal geometry for organic solar cells.," *Nano letters*, vol. 9, pp. 2742–6, jul 2009.

[59] D.-H. Ko, J. R. Tumbleston, A. Gadisa, M. Aryal, Y. Liu, R. Lopez, and E. T. Samulski, "Light-trapping nano-structures in organic photovoltaic cells," *Journal of Materials Chemistry*, vol. 21, no. 41, p. 16293, 2011.

[60] A. N. Sprafke and R. B. Wehrspohn, "Light Trapping Concepts for Photon Management in Solar Cells," *Green*, vol. 2, pp. 177–187, jan 2012.

[61] S. Mokkapati and K. R. Catchpole, "Nanophotonic light trapping in solar cells," *Journal of Applied Physics*, vol. 112, no. 10, p. 101101, 2012.

[62] Q. Gan, F. J. Bartoli, and Z. H. Kafafi, "Plasmonic-enhanced organic photovoltaics: Breaking the 10% efficiency barrier," *Advanced Materials*, vol. 25, no. 17, pp. 2385–2396, 2013.

[63] Z. Tang, W. Tress, and O. Inganäs, "Light trapping in thin film organic solar cells," *Materials Today*, vol. 17, pp. 389–396, oct 2014.

[64] S.-I. Na, S.-S. Kim, J. Jo, S.-H. Oh, J. Kim, and D.-Y. Kim, "Efficient Polymer Solar Cells with Surface Relief Gratings Fabricated by Simple Soft Lithography," *Advanced Functional Materials*, vol. 18, pp. 3956–3963, dec 2008.

[65] M. Niggemann, M. Glatthaar, A. Gombert, A. Hinsch, and V. Wittwer, "Diffraction gratings and buried nano-electrodes - architectures for organic solar cells," *Thin Solid Films*, vol. 451-452, pp. 619–623, mar 2004.

[66] R. M. de Oliveira Hansen, Y. Liu, M. Madsen, and H.-G. Rubahn, "Flexible organic solar cells including efficiency enhancing grating structures.," *Nanotechnology*, vol. 24, p. 145301, apr 2013.

[67] F. Monestier, J.-J. Simon, P. Torchio, L. Escoubas, F. Flory, S. Bailly, R. de Bettignies, S. Guillerez, and C. Defranoux, "Modeling the short-circuit current density of polymer solar cells based on P3HT:PCBM blend," *Solar Energy Materials and Solar Cells*, vol. 91, no. 5, pp. 405–410, 2007.

[68] L. S. Roman, O. Inganäs, T. Granlund, T. Nyberg, M. Svensson, M. R. Andersson, and J. C. Hummelen, "Trapping light in polymer photodiodes with soft embossed gratings," *Advanced Materials*, vol. 12, no. 3, pp. 189–195, 2000.

[69] J. Y. Park, N. R. Hendricks, and K. R. Carter, "Solvent-assisted soft nanoimprint lithography for structured bilayer heterojunction organic solar cells," *Langmuir*, vol. 27, no. 17, pp. 11251–11258, 2011.

[70] M. Niggemann, M. Riede, A. Gombert, and K. Leo, "Light trapping in organic solar cells," *Physica Status Solidi (a)*, vol. 205, pp. 2862–2874, dec 2008.

[71] K. S. Nalwa, J.-M. M. Park, K.-M. M. Ho, and S. Chaudhary, "On realizing higher efficiency polymer solar cells using a textured substrate platform.," *Advanced Materials*, vol. 23, pp. 112–6, jan 2011.

[72] E. Yablonovitch and G. Cody, "Intensity Enhancement in Textured Optical Sheets for Solar Cells," *IEEE Transactions on Electron Devices*, vol. 5*, no. 2, pp. 300–306, 1982.

[73] M. Otto, M. Kroll, T. Käsebier, R. Salzer, A. Tünnermann, and R. B. Wehrspohn, "Extremely low surface recombination velocities in black silicon passivated by atomic layer deposition," *Applied Physics Letters*, vol. 100, no. 19, pp. 1–5, 2012.

[74] Z. Yu, A. Raman, and S. Fan, "Fundamental limit of nanophotonic light trapping in solar cells," *Proceedings of the National Academy of Sciences*, vol. 107, no. 41, pp. 17491–17496, 2010.

[75] J. D. Myers, W. Cao, V. Cassidy, S.-H. Eom, R. Zhou, L. Yang, W. You, and J. Xue, "A universal optical approach to enhancing efficiency of organic-based photovoltaic devices," *Energy & Environmental Science*, vol. 5, no. 5, p. 6900, 2012.

[76] K. Tvingstedt, S. Dal Zilio, O. Inganäs, and M. Tormen, "Trapping light with micro lenses in thin film organic photovoltaic cells.," *Optics express*, vol. 16, no. 26, pp. 21608–21615, 2008.

[77] M. Biernat and J. Haberko, "Breath figure structures as the light trapping layer in organic photovoltaic cells," *in preparation*, 2018.

[78] M. Rubinstein and R. Colby, *Polymer Physics*. Oxford University Press, jun 2003.

[79] P. Flory, *Principles of polymer chemistry*. Cornell University Press, 1953.

[80] I. Teraoka, *Polymer Solutions: An Introduction to Physical Properties*, vol. 3. John Wiley & Sons, Inc., 2002.

[81] J. Brandrup, E. Immergut, and E. Grulke, eds., *Polymer Handbook*. John Wiley & Sons, Inc., 4th ed., 1999.

[82] L. M. Robeson, *Characterization of Polymer Blends*. Weinheim, Germany: Wiley-VCH Verlag GmbH & Co. KGaA, nov 2014.

[83] J. Raczkowska, "Self-organization, structure formation and pattern replication in nanometer polymer blend films," no. June, 2005.

[84] M. Biernat, P. Dąbczyński, P. Biernat, and J. Rysz, "Phase separation in PCDBT:PCBM blends: from Flory–Huggins Interaction Parameters to Ternary Phase Diagrams," *in preparation*, 2008.

[85] C. J. Lawrence, "The mechanics of spin coating of polymer films," *Physics of Fluids*, vol. 31, no. 10, pp. 2786–2795, 1988.

[86] J. Rysz, M. Josiek, M. M. Marzec, and E. Moons, "Pattern replication in blends of semiconducting and insulating polymers casted by horizontal dipping," *Journal of Polymer Science Part B: Polymer Physics*, vol. 51, pp. 1419–1426, oct 2013.

[87] B. Park and M.-y. Han, "Organic light-emitting devices fabricated using a premetered coating process.," *Optics express*, vol. 17, no. 24, pp. 21362–21369, 2009.

[88] B. Park and M.-Y. Han, "Photovoltaic characteristics of polymer solar cells fabricated by pre-metered coating process.," *Optics express*, vol. 17, pp. 13830–40, aug 2009.

[89] F. Nickel, C. Sprau, M. F. G. Klein, P. Kapetana, N. Christ, X. Liu, S. Klinkhammer, U. Lemmer, and A. Colsmann, "Spatial mapping of photocurrents in organic solar cells comprising wedge-shaped absorber layers for an efficient material screening," *Solar Energy Materials and Solar Cells*, vol. 104, pp. 18–22, sep 2012.

[90] M. Kowalcze, "Budowa stanowiska do wytwarzania warstw organicznych o zadanym gradiencie wlasciwosci fizykochemicznych," *Praca magisterska*, p. 58, 2010.

[91] L. Landau and B. Levich, "Dragging of a Liquid by a Moving Plate," *Acta Physicochimica U.R.S.S.*, vol. XVII, no. 1-2, 1942.

[92] R. Kelsall, I. Hamley, and M. Goeghegan, eds., *Nanoscale Science and Technology.* Wiley-VCH Verlag GmbH & Co. KGaA, 2005.

[93] J. Aitken, "Breath figures," *Nature*, vol. 86, no. 2172, pp. 516–7, 1911.

[94] G. Widawski, M. Rawiso, and B. François, "Self-organized honeycomb morphology of star-polymer polystyrene films," *Nature*, vol. 369, pp. 387–389, jun 1994.

[95] A. Muñoz-Bonilla, M. Fernández-García, and J. Rodríguez-Hernández, "Towards hierarchically ordered functional porous polymeric surfaces prepared by the breath figures approach," *Progress in Polymer Science*, vol. 39, pp. 510–554, mar 2014.

[96] W. Madej, A. Budkowski, J. Raczkowska, and J. Rysz, "Breath figures in polymer and polymer blend films spin-coated in dry and humid ambience.," *Langmuir*, vol. 24, pp. 3517–24, apr 2008.

[97] M. S. Park and J. K. Kim, "Breath figure patterns prepared by spin coating in a dry environment.," *Langmuir : the ACS journal of surfaces and colloids*, vol. 20, pp. 5347–52, jun 2004.

[98] F. Galeotti, F. Trespidi, and M. Pasini, "Breath Figure-Assisted Fabrication of Nanostructured Coating on Silicon Surface and Evaluation of Its Antireflection Power," *Journal of Nanomaterials*, vol. 2016, no. April, pp. 1–8, 2016.

[99] W. Madej, "Wpływ warunków samoorganizacji na morfologię wieloskładnikowych warstw polimerów," *Praca magisterska*, p. 63, 2006.

[100] Y. Xia and G. M. Whitesides, "Soft Lithography," *Angewandte Chemie International Edition*, vol. 37, pp. 550–575, mar 1998.

[101] V. Meenakshi, Y. Babayan, and T. W. Odom, "Benchtop Nanoscale Patterning Using Soft Lithography," *Journal of Chemical Education*, vol. 84, p. 1795, nov 2007.

[102] H. Yabu and M. Shimomura, "Simple fabrication of micro lens arrays," *Langmuir*, vol. 21, no. 5, pp. 1709–1711, 2005.

[103] J. N. Lee, C. Park, and G. M. Whitesides, "Solvent Compatibility of Poly(dimethylsiloxane)-Based Microfluidic Devices," *Analytical Chemistry*, vol. 75, no. 23, pp. 6544–6554, 2003.

[104] X.-m. Zhao, Y. Xia, and G. M. Whitesides, "Fabrication of Three-Dimensional Micro-Structures: Microtransfer Molding," *Advanced Materials*, vol. 8, no. 10, pp. 837–840, 1996.

[105] K. I. C. Ossila Ltd, "The Ossila Organic Photovoltaic (OPV) and Organic Light Emitting Diode (OLED) Fabrication Manual," 2016.

[106] G. Ho Jung, K.-G. Lim, T.-W. Lee, and J.-L. Lee, "Morphological and electrical effect of an ultrathin iridium oxide hole extraction layer on P3HT:PCBM bulk-heterojunction solar cells," *Solar Energy Materials and Solar Cells*, vol. 95, pp. 1146–1150, apr 2011.

[107] A. Wagenpfahl, D. Rauh, M. Binder, C. Deibel, and V. Dyakonov, "S-shaped current–voltage characteristics of organic solar devices," *Physical Review B*, vol. 82, no. 115306, pp. 1–9, 2010.

[108] Y. Sun, C. J. Takacs, S. R. Cowan, J. H. Seo, X. Gong, A. Roy, and A. J. Heeger, "Efficient, air-stable bulk heterojunction polymer solar cells using MoO x as the anode interfacial layer," *Advanced Materials*, vol. 23, no. 19, pp. 2226–2230, 2011.

[109] S. H. Park, A. Roy, S. Beaupré, S. Cho, N. Coates, J. S. Moon, D. Moses, M. Leclerc, K. Lee, S. Beaupre, and A. J. Heeger, "Bulk heterojunction solar cells with internal quantum efficiency approaching 100%," *Nature Photon.*, vol. 3, no. 5, pp. 297–302, 2009.

[110] G. Binnig, C. F. Quate, and C. Gerber, "Atomic Force Microscope," *Physical Review Letters*, vol. 56, pp. 930–933, mar 1986.

[111] S. Sheiko and S. Magonov, "Scanning Probe Microscopy of Polymer," in *Polymer Science: A Comprehensive Reference* (K. Matyjaszewski, M. Moller, T. Hashimoto, H. W. Spiess, and M. Takenaka, eds.), vol. 2, p. 41, Elsevier Inc., 2013.

[112] P. Klapetek, D. Necas, and C. Anderson, *Gwyddion user guide.* 2013.

[113] G. E. Jellison and F. A. Modine, "Parameterization of the optical functions of amorphous materials in the interband region," *Appl. Phys. Lett*, vol. 69, no. 3, pp. 371–373, 1996.

[114] D. Goustouridis, K. Manoli, S. Chatzandroulis, M. Sanopoulou, and I. Raptis, "Characterization of polymer layers for silicon micromachined bilayer chemical sensors using white light interferometry," *Sensors and Actuators, B: Chemical*, vol. 111-112, no. SUPPL., pp. 549–554, 2005.

[115] M. Josiekova, "Badanie właściwości elektrooptycznych cienkich warstw polimerów sprzężonych," *Praca magisterska*, p. 61, 2011.

[116] L. Xue, J. Zhang, and Y. Han, "Phase separation induced ordered patterns in thin polymer blend films," *Progress in Polymer Science*, vol. 37, pp. 564–594, apr 2012.

[117] A. Budkowski, A. Bernasik, E. Moons, M. Lekka, J. Zemla, J. Jaczewska, J. Haberko, J. Raczkowska, J. Rysz, and K. Awsiuk, "Structures in Multi-component Polymer Films: Their Formation, Observation and Applications in Electronics and Biotechnology," *Acta Physica Polonica A*, vol. 115, no. 2, pp. 435–440, 2009.

[118] J. J. M. Halls, K. Pichler, R. H. Friend, S. C. Moratti, and A. B. Holmes, "Exciton diffusion and dissociation in a poly(p-phenylenevinylene)/C60 heterojunction photovoltaic cell," *Applied Physics Letters*, vol. 68, no. 22, pp. 3120–3122, 1996.

[119] H. Hoppe and N. S. Sariciftci, "Morphology of polymer/fullerene bulk heterojunction solar cells," *Journal of Materials Chemistry*, vol. 16, no. 1, p. 45, 2006.

[120] J. J. Michels and E. Moons, "Simulation of Surface-Directed Phase Separation in a Solution-Processed Polymer/PCBM Blend," *Macromolecules*, vol. 46, pp. 8693–8701, nov 2013.

[121] S. Coveney, *Fundamentals of Phase Separation in Polymer Blend Thin Films.* PhD thesis, University of Sheffield, 2015.

[122] C. Schaefer, J. J. Michels, and P. Van Der Schoot, "Structuring of Thin-Film Polymer Mixtures upon Solvent Evaporation," *Macromolecules*, vol. 49, no. 18, pp. 6858–6870, 2016.

[123] S. Nilsson, A. Bernasik, A. Budkowski, and E. Moons, "Morphology and Phase Segregation of Spin-Casted Films of Polyfluorene / PCBM Blends," *Macromolecules*, vol. 40, pp. 8291–8301, nov 2007.

[124] J. Jaczewska, I. Raptis, A. Budkowski, D. Goustouridis, J. Raczkowska, M. Sanopoulou, E. Pamuła, A. Bernasik, and J. Rysz, "Swelling of poly(3-alkylthiophene) films exposed to solvent vapors and humidity: Evaluation of solubility parameters," *Synthetic Metals*, vol. 157, pp. 726–732, sep 2007.

[125] E. C. Baughan, "The absorption of organic vapours by thin films of polystyrene," *T. Faraday Soc.*, vol. 44, pp. 495–506, 1948.

[126] R. Corneliussen, S. A. Rice, and H. Yamakawa, "On the Thermodynamic Properties of Solutions of Polar Polymers. A Comparison of Experiment and Theory," *The Journal of Chemical Physics*, vol. 38, no. 7, p. 1768, 1963.

[127] I. Noda, Y. Higo, N. Ueno, and T. Fujimoto, "Semidilute region for linear polymers in good solvents," *Macromolecules*, vol. 17, pp. 1055–1059, 1984.

[128] S. K. Lee, J. M. Cho, Y. Goo, W. S. Shin, and J.-c. Lee, "Synthesis and characterization of thiazolo [5 , 4-d] thiazole-based copolymer for high performance polymer solar cells," *Chemical Communications*, vol. 47, pp. 1791–1793, 2011.

[129] D. Leman, M. A. Kelly, S. Ness, S. Engmann, A. Herzing, C. Snyder, H. W. Ro, R. J. Kline, D. M. DeLongchamp, and L. J. Richter, "In situ characterization of polymer-fullerene bilayer stability," *Macromolecules*, vol. 48, no. 2, pp. 383–392, 2015.

[130] P. Dąbczyński, "Interdyfuzja pochodnych fulerenów w cienkich warstwach PQT-12 pod wpływem wygrzewania rozpuszczalnikowego," *Praca magisterska*, p. 56, 2015.

[131] B. Mayer, C. C. Collins, and M. Walton, "Transient analysis of carrier gas saturation in liquid source vapor generators," *Journal of Vacuum Science & Technology A: Vacuum, Surfaces, and Films*, vol. 19, no. 1, p. 329, 2001.

[132] A. R. Berens and H. B. Hopfenberg, "Diffusion and relaxation in glassy polymer powders: 2. Separation of diffusion and relaxation parameters," *Polymer*, vol. 19, no. 5, pp. 489–496, 1978.

[133] M. Minami, "Vapor Concentration Control System for Bubbling Method," *Readout: English Edition*, vol. 41, no. 41, pp. 34–37, 2013.

[134] A. Love, S. Middleman, and A. K. Hochberg, "The dynamics of bubblers as vapor delivery systems," *Journal of Crystal Growth*, vol. 129, no. 1-2, pp. 119–133, 1993.

[135] G. Wypych, ed., *Handbook of solvents*, vol. 1. Toronto , New York: ChemTec Publishing, 2001.

[136] C. H. Peters, I. T. Sachs-Quintana, J. P. Kastrop, S. Beaupré, M. Leclerc, and M. D. McGehee, "High efficiency polymer solar cells with long operating lifetimes," *Advanced Energy Materials*, vol. 1, no. 4, pp. 491–494, 2011.

[137] C. Reichardt, *Solvents and Solvent Effects in Organic Chemistry*. Weinheim, FRG: Wiley-VCH Verlag GmbH & Co. KGaA, dec 2002.

[138] G. Fang, J. Liu, Y. Fu, B. Meng, B. Zhang, Z. Xie, and L. Wang, "Improving the nanoscale morphology and processibility for PCDTBT-based polymer solar cells via solvent mixtures," *Organic Electronics*, vol. 13, pp. 2733–2740, nov 2012.

[139] A. F. M. Barton, "Solubility parameters," *Chemical Reviews*, vol. 75, pp. 731–753, 1975.

[140] C. M. Hansen, *Hansen Solubility Parameters A User's Handbook*. CRC Press, Taylor&Francis Group, 2007.

[141] M. Belmares, M. Blanco, W. A. Goddard, R. B. Ross, G. Caldwell, S. H. Chou, J. Pham, P. M. Olofson, and C. Thomas, "Hildebrand and hansen solubility parameters from molecular dynamics with applications to electronic nose polymer sensors," *Journal of Computational Chemistry*, vol. 25, no. 15, pp. 1814–1826, 2004.

[142] D. T. Duong, B. Walker, J. Lin, C. Kim, J. Love, B. Purushothaman, J. E. Anthony, and T.-Q. Nguyen, "Molecular solubility and hansen solubility parameters for the analysis of phase separation in bulk heterojunctions," *Journal of Polymer Science Part B: Polymer Physics*, vol. 50, pp. 1405–1413, oct 2012.

[143] F. Machui, S. Abbott, D. Waller, M. Koppe, and C. J. Brabec, "Determination of Solubility Parameters for Organic Semiconductor Formulations," *Macromolecular Chemistry and Physics*, vol. 212, pp. 2159–2165, oct 2011.

[144] I. Burgués-Ceballos, F. Machui, J. Min, T. Ameri, M. M. Voigt, Y. N. Luponosov, S. A. Ponomarenko, P. D. Lacharmoise, M. Campoy-Quiles, and C. J. Brabec, "Solubility Based Identification of Green Solvents for Small Molecule Organic Solar Cells," *Advanced Functional Materials*, vol. 24, pp. 1449–1457, mar 2014.

[145] P.-k. Shin, P. Kumar, A. Kumar, S. Kannappan, and S. Ochiai, "Effects of Organic Solvents for Composite Active Layer of PCDTBT / PC 71 BM on Characteristics of Organic Solar Cell Devices," *International journal of photoenergy*, vol. 2014, pp. 1–8, 2013.

[146] M. Sprenger, S. Walheim, A. Budkowski, and U. Steiner, "Hierarchic Structure Formation in Binary and Ternary Polymer Blends," *Interface Science*, vol. 11, pp. 225–235, 2003.

[147] S. Y. Heriot and R. A. L. Jones, "An interfacial instability in a transient wetting layer leads to lateral phase separation in thin spin-cast polymer-blend films.," *Nature materials*, vol. 4, no. 10, pp. 782–786, 2005.

[148] H. Hoppe and N. S. Sariciftci, "Organic solar cells: An overview," *Journal of Materials Research*, vol. 19, no. 7, pp. 1924–1945, 2004.

[149] R. Hansson, L. K. E. Ericsson, N. P. Holmes, J. Rysz, A. Opitz, M. Campoy-Quiles, E. Wang, M. G. Barr, A. L. D. Kilcoyne, X. Zhou, P. Dastoor, and E. Moons, "Vertical and lateral morphology effects on solar cell performance for a thiophene–quinoxaline copolymer:PC70BM blend," *Journal of Materials Chemistry A*, vol. 3, no. 13, pp. 6970–6979, 2015.

[150] H. W. Deckman, C. Wronski, H. Witze, and E. Yablonovitch, "Optically enhanced amorphous silicon solar cells," *Applied Physics Letters*, vol. 42, no. 11, p. 968, 1983.

[151] M. Berginski, J. Hupkes, M. Schulte, G. Schope, H. Stiebig, B. Rech, and M. Wuttig, "The effect of front ZnO:Al surface texture and optical transparency on efficient light trapping in silicon thin-film solar cells," *Journal of Applied Physics*, vol. 101, no. 7, p. 074903, 2007.

[152] C. Battaglia, C.-M. Hsu, K. Söderström, J. Escarré, F.-J. Haug, M. Charrière, M. Boccard, M. Despeisse, D. T. L. Alexander, M. Cantoni, Y. Cui, and C. Ballif, "Light trapping in solar cells: can periodic beat random?," *ACS nano*, vol. 6, pp. 2790–7, mar 2012.

[153] J. Li, L. Zuo, H. Pan, H. Jiang, T. Liang, Y. Shi, H. Chen, and M. Xu, "Texture design of electrodes for efficiency enhancement of organic solar cells," *Journal of Materials Chemistry A*, vol. 1, no. 7, p. 2379, 2013.

[154] C. Cho, H. Kim, S. Jeong, S.-W. W. Baek, J.-W. W. Seo, D. Han, K. Kim, Y. Park, S. Yoo, and J.-Y. Y. Lee, "Random and V-groove texturing for efficient light trapping in organic photovoltaic cells," *Solar Energy Materials and Solar Cells*, vol. 115, pp. 36–41, aug 2013.

[155] M.-S. Kim, J.-S. Kim, J. C. Cho, M. Shtein, L. J. Guo, and J. Kim, "Flexible conjugated polymer photovoltaic cells with controlled heterojunctions fabricated using nanoimprint lithography," *Appl. Phys. Lett.*, vol. 90, no. 12, p. 123113, 2007.

[156] R. Meier, *Novel Structuring Routines for Organic Photovoltaics.* PhD thesis, Technische Universitat Munschen, 2012.

[157] A. J. Smith, C. Wang, D. Guo, C. Sun, and J. Huang, "Repurposing Blu-ray movie discs as quasi-random nanoimprinting templates for photon management," *Nature Communications*, vol. 5, pp. 1–5, 2014.

[158] E. Menard, M. a. Meitl, Y. Sun, J.-U. Park, D. J.-L. Shir, Y.-S. Nam, S. Jeon, and J. a. Rogers, "Micro- and nanopatterning techniques for organic electronic and optoelectronic systems.," *Chemical reviews*, vol. 107, pp. 1117–60, apr 2007.

[159] D. J. Lipomi, R. V. Martinez, L. Cademartiri, and G. M. Whitesides, "Soft Lithographic Approaches to Nanofabrication," in *Polymer Science:A Comprehensive Reference*, vol. 7, pp. 211–231, Elsevier B.V., 2012.

[160] G. Tosello, H. N. Hansen, F. Marinello, and S. Gasparin, "Replication and dimensional quality control of industrial nanoscale surfaces using calibrated AFM measurements and SEM image processing," *CIRP Annals - Manufacturing Technology*, vol. 59, no. 1, pp. 563–568, 2010.

[161] S. K. Lin, I. C. Lin, and D. P. Tsai, "Characterization of nano recorded marks at different writing strategies on phase-change recording layer of optical disks.," *Optics express*, vol. 14, pp. 4452–8, may 2006.

[162] Y. Xia and G. M. Whitesides, "Extending Microcontact Printing as a Microlithographic Technique," *Langmuir*, vol. 13, no. 7, pp. 2059–2067, 1997.

[163] Y. Yang, K. Mielczarek, M. Aryal, A. Zakhidov, and W. Hu, "Nanoimprinted polymer solar cell.," *ACS nano*, vol. 6, pp. 2877–92, apr 2012.

[164] B. Kitchen, O. Awartani, R. J. Kline, T. McAfee, H. Ade, and B. T. O'Connor, "Tuning Open-Circuit Voltage in Organic Solar Cells with Molecular Orientation," *ACS Applied Materials & Interfaces*, vol. 7, no. 24, pp. 13208–13216, 2015.

[165] X. H. Li, W. E. I. Sha, W. C. H. Choy, D. D. S. Fung, and F. X. Xie, "Efficient inverted polymer solar cells with directly patterned active layer and silver back grating," *Journal of Physical Chemistry C*, vol. 116, no. 12, pp. 7200–7206, 2012.

[166] G. Teran-Escobar, D. M. Tanenbaum, E. Voroshazi, and M. Hermenau et al., "On the stability of a variety of organic photovoltaic devices by IPCE and in situ IPCE analyses – the ISOS-3 inter-laboratory collaboration," *Physical Chemistry Chemical Physics*, vol. 14, no. 33, p. 11824, 2012.

[167] N. Grossiord, J. M. Kroon, R. Andriessen, and P. W. Blom, "Degradation mechanisms in organic photovoltaic devices," *Organic Electronics*, vol. 13, no. 3, pp. 432–456, 2012.

[168] H. Cao, W. He, Y. Mao, X. Lin, K. Ishikawa, J. H. Dickerson, and W. P. Hess, "Recent progress in degradation and stabilization of organic solar cells," *Journal of Power Sources*, vol. 264, pp. 168–183, 2014.

[169] M. Srinivasarao, D. Collings, A. Philips, and S. Patel, "Three-dimensionally ordered array of air bubbles in a polymer film.," *Science (New York, N.Y.)*, vol. 292, pp. 79–83, apr 2001.

[170] A. Zhang, H. Bai, and L. Li, "Breath Figure: A Nature-Inspired Preparation Method for Ordered Porous Films," *Chemical Reviews*, vol. 115, pp. 9801–9868, sep 2015.

[171] J. Jaczewska, A. Budkowski, A. Bernasik, I. Raptis, J. Raczkowska, D. Goustouridis, J. Rysz, and M. Sanopoulou, "Humidity and Solvent Effects in Spin-Coated Polythiophene–Polystyrene Blends," *Journal of Applied Polymer Science*, vol. 105, pp. 23–28, 2006.

[172] P. Escalé, L. Rubatat, L. Billon, and M. Save, "Recent advances in honeycomb-structured porous polymer films prepared via breath figures," *European Polymer Journal*, vol. 48, pp. 1001–1025, jun 2012.

[173] A. Limaye, R. Narhe, A. Dhote, and S. Ogale, "Evidence for convective effects in breath figure formation on volatile fluid surfaces.," *Physical review letters*, vol. 76, pp. 3762–3765, may 1996.

[174] A. Steyer, P. Guenoun, D. Beysens, and C. M. Knobler, "Two-dimensional ordering during droplet growth on a liquid surface," *Physical Review B*, vol. 42, no. 1, pp. 1086–1089, 1990.

[175] J. Raczkowska, J. Rysz, a. Budkowski, J. Lekki, M. Lekka, a. Bernasik, K. Kowalski, and P. Czuba, "Surface Patterns in Solvent-Cast Polymer Blend Films Analyzed with an Integral-Geometry Approach," *Macromolecules*, vol. 36, pp. 2419–2427, apr 2003.

[176] S.-F. Leung, Q. Zhang, F. Xiu, D. Yu, J. C. Ho, D. Li, and Z. Fan, "Light Management with Nanostructures for Optoelectronic Devices," *The Journal of Physical Chemistry Letters*, vol. 5, pp. 1479–1495, apr 2014.

[177] A. Deinega, I. Valuev, B. Potapkin, and Y. Lozovik, "Minimizing light reflection from dielectric textured surfaces.," *Journal of the Optical Society of America. A, Optics, image science, and vision*, vol. 28, pp. 770–7, may 2011.

[178] M. H. Stenzel-Rosenbaum, T. P. Davis, A. G. Fane, and V. Chen, "Porous Polymer Films and Honeycomb Structures Made by the Self-Organization of Well-Defined Macromolecular Structures Created by Living Radical Polymerization Techniques," *Angewandte Chemie*, vol. 113, pp. 3536–3540, sep 2001.

[179] C.-L. Lin, P.-H. Tung, and F.-C. Chang, "Synthesis of rod-coil diblock copolymers by ATRP and their honeycomb morphologies formed by the 'breath figures' method," *Polymer*, vol. 46, pp. 9304–9313, oct 2005.

[180] M. Huh, M.-h. Jung, Y. S. Park, T.-b. Kang, C. Nah, R. A. Russell, P. J. Holden, and S. I. Yun, "Fabrication of honeycomb-structured porous films from poly(3-hydroxybutyrate) and poly(3-hydroxybutyrate-co-3-hydroxyvalerate) via the breath figures method," *Polymer Engineering & Science*, vol. 52, pp. 920–926, apr 2012.

[181] H. Ma, Y. Tian, and X. Wang, "In situ optical microscopy observation of the growth and rearrangement behavior of surface holes in the breath figure process," *Polymer*, vol. 52, pp. 489–496, jan 2011.

[182] A. S. de León, A. Muñoz-Bonilla, M. Fernández-García, and J. Rodríguez-Hernández, "Breath figures method to control the topography and the functionality of polymeric surfaces in porous films and microspheres," *Journal of Polymer Science Part A: Polymer Chemistry*, vol. 50, pp. 851–859, mar 2012.

[183] K.-i. Hiwatari, T. S. Irizawa, F. S. Eto, A. K. Ishida, K.-i. Hiwatari, T. Serizawa, F. Seto, A. Kishida, Y. Muraoka, and M. Akashi, "Graft Copolymers Having Hydrophobic Backbone and Hydrophilic Branches XXXIV. Fabrication and Control of Honeycomb Structure Prepared from Amphiphilic Graft Copolymers," *Polymer Journal*, vol. 33, no. 9, pp. 669–675, 2001.

[184] J. Mansouri, E. Yapit, and V. Chen, "Polysulfone filtration membranes with isoporous structures prepared by a combination of dip-coating and breath figure approach," *Journal of Membrane Science*, vol. 444, pp. 237–251, 2013.

[185] H. G. Jeon, C. Y. Cho, J. C. Shin, and B. Park, "Inverted polymer solar cells fabricated by a pre-metered coating process," *Journal of Materials Chemistry*, vol. 22, no. 43, p. 23022, 2012.

[186] J. Raczkowska, a. Bernasik, a. Budkowski, J. Rysz, K. Kowalski, M. Lekka, P. Czuba, and J. Lekki, "Pattern replication examined with integral geometry approach: application to ion milling of polymer blend films," *Thin Solid Films*, vol. 476, pp. 358–365, apr 2005.

[187] S. C. Kapfer, *Morphometry and Physics of Particulate and Porous Media*. PhD thesis, Friedrich-Alexander-Universitat Erlangen Nurnberg, 2011.

[188] S. Ji, K. Song, T. B. Nguyen, N. Kim, and H. Lim, "Optimal moth eye nanostructure array on transparent glass towards broadband antireflection," *ACS Applied Materials and Interfaces*, vol. 5, no. 21, pp. 10731–10737, 2013.

[189] L. A. Connal and G. G. Qiao, "Preparation of porous poly(dimethyIsiloxane)-based honeycomb materials with hierarchal surface features and their use as soft-lithography templates," *Advanced Materials*, vol. 18, no. 22, pp. 3024–3028, 2006.

[190] V. Vohra, S. Yunus, A. Attout, U. Giovanella, G. Scavia, R. Tubino, C. Botta, and A. Bolognesi, "Bifunctional microstructured films and surfaces obtained by soft lithography from breath figure arrays," *Soft Matter*, vol. 5, no. 8, p. 1656, 2009.

[191] L. Li, Y. Zhong, J. Li, J. Gong, Y. Ben, J. Xu, X. Chen, and Z. Ma, "Breath figure lithography: A facile and versatile method for micropatterning.," *Journal of colloid and interface science*, vol. 342, no. 1, pp. 192–197, 2010.

[192] F. Trespidi, G. Timò, F. Galeotti, and M. Pasini, "PDMS antireflection nano-coating for glass substrates," *Microelectronic Engineering*, vol. 126, pp. 13–18, 2014.

[193] F. Galeotti, W. Mróz, G. Scavia, and C. Botta, "Microlens arrays for light extraction enhancement in organic light-emitting diodes: A facile approach," *Organic Electronics*, vol. 14, pp. 212–218, jan 2013.